



Vapour-phase Hydrothermal Synthesis of Functional Nanomaterials for Energy Conversion Applications

Author

Tan, Zhijin

Published

2017-11-22

Thesis Type

Thesis (Masters)

School

Griffith School of Environment

DOI

[10.25904/1912/2787](https://doi.org/10.25904/1912/2787)

Downloaded from

<http://hdl.handle.net/10072/371911>

Griffith Research Online

<https://research-repository.griffith.edu.au>

Vapour-phase Hydrothermal Synthesis of Functional Nanomaterials for Energy Conversion Applications

Zhijin tan

A thesis submitted in fulfillment of the requirements of the degree of

Master of Philosophy

in

The Griffith School of Environment

Griffith University, Gold Coast campus, Queensland

22nd November 2017



Statement of Originality

The work of this thesis has not previously been submitted for a degree or diploma in any university. To the best of my knowledge and belief, the thesis contains no material previously published or written by another person except where due reference is made in the thesis itself.

.....

Zhijin Tan

November 2017

Abstract

There has been an increasing demand of energy for socioeconomic activities and global population growth. Such gigantic amount of energy has been dominantly supplied with the consumption of fossil fuels that cannot be reliably generated in near future. This energy crisis has recently raised as a global issue that has attracted widespread attention. Abundant, renewable and environmentally friendly solar energy is one of the alternative energy sources to reduce the current dependence on traditional fossil fuels and help alleviate the environmental pollution. As such, photovoltaic devices, or solar cells, that convert solar energy into electricity have been explored intensively by academia and industries. Dye sensitized solar cells (DSSCs) have been proven to be one of the more economic, versatile and robust photovoltaic devices. However, the use of expensive, scarce novel metal, normally platinum or its alloys, as the counter electrode material has to a large extent been limiting the practical application of DSSCs. Thus there are urgent needs to develop low cost, earth abundant, high performance, chemical stable materials as the electrocatalysts for DSSCs.

Metal oxides are one of the most abundant and stable substances on earth however they do not demonstrate high electrocatalytical activities as counter electrode materials. The aim of this thesis is to develop a generic approach to convert the widely available metal oxide into high performance electrocatalyst as counter electrode materials for DSSCs. The thesis has been structured as followings to achieve the goals: in chapter 1, an overview on the photovoltaic devices and DSSCs has been presented. In particular, the research background on the counter electrode materials of DSSCs has been provided with a mini review of the electrode materials developed to date. In chapter 2, Co_3O_4 nanowires films have been fabricated as the starting materials and subsequently converted into sulphur doped (S-doped) Co_3O_4 using a vapour-phase hydrothermal (VPH) approach. The structure of Co_3O_4 film and VPH parameters have been optimized to achieve the best electrocatalytic performance that demonstrates significant improvement compare with the pristine Co_3O_4 film. In chapter 3, thin Co_3O_4 nanosheets

film has been fabricated and converted in to S-Co₃O₄ film using VPH method. It has been demonstrated that an unprecedentedly high surface S content (>47%) has been achieved and the photovoltaic conversion efficiency of the DSSCs with such S-Co₃O₄ film was as superior as the one with benchmark Pt electrocatalysts. In chapter 4, the applicability of VPH method as a generic approach to convert metal oxides into electrocatalytic active materials has been investigated. Metal oxide films such as NiO and Fe₂O₃ have been successfully fabricated and modified with VPH treatment. The DSSCs equipped with such films as counter electrode have exhibited significantly improved solar to electricity conversion efficiency compared to those with equipped with pristine metal oxide film. Based on the findings in thesis, a conclusion has been provided in chapter 5 followed by a perspective on future research.

Acknowledgements

First and foremost, I would like to express my sincerest gratitude towards my principal supervisors, Professor Huijun Zhao for giving me the opportunity to pursue my studies under their supervisions at Centre for Clean Environment and Energy (CCEE). I would also like to thank another principle supervisor Dr Porun Liu for his supervision, discussions and technique support. Moreover, I am very grateful to my associate supervisors, Dr Yun Wang and Professor Haimin Zhang for their supervision and encouragement. The completion of this thesis would not have been possible without their persistent patience, guidance and support.

The work presented in this thesis would not have been possible without the kind support from many other colleagues in CCEE and Griffith School of Environment. I am grateful to Dr Yibing Li, Dr Xiaolu Liu, Dr Jiangxia Qiu, Dr Sheng Li, Dr Min Ling, Dr Tao Sun, Dr Lulu Wang, Dr Mohammad Al-Mamun, Dr Joshua Hayton, Mr Wentao Liang, Mr Kaicai Fan, Mr Lixue Jiang. Also, Thanks go to Mrs Christina Perry, Ms Belinda Hachem for their administrative support and consideration. I would like to show my gratitude to Griffith University and Australian Government for scholarship and financial support.

Finally, my deepest appreciation must go to my wife Dr Qi Jiang, who always loves me and supports the decisions I made, and I also would thank my son Nathan Tan and my daughter Chloe Tan, who give me motivations and make my life more meaningful. Moreover, my thanks go to my parents and parents-in-law, who have supported me and helped me to look after my family.

All Papers Included are Co-Authored

Acknowledgement of papers included in this thesis

Section 9.1 of the Griffith University Code for the Responsible Conduct of Research (“Criteria for Authorship”), in accordance with Section 5 of the Australian Code for the Responsible Conduct of Research, states:

To be named as an author, a researcher must have made a substantial scholarly contribution to the creative or scholarly work that constitutes the research output, and be able to take public responsibility for at least that part of the work they contributed. Attribution of authorship depends to some extent on the discipline and publisher policies, but in all cases, authorship must be based on substantial contributions in a combination of one or more of:

- conception and design of the research project
- analysis and interpretation of research data
- drafting or making significant parts of the creative or scholarly work or critically revising it so as to contribute significantly to the final output.

Section 9.3 of the Griffith University Code (“Responsibilities of Researchers”), in accordance with Section 5 of the Australian Code, states:

Researchers are expected to:

- Offer authorship to all people, including research trainees, who meet the criteria for authorship listed above, but only those people accept or decline offers of authorship promptly in writing.
- Include in the list of authors only those who have accepted authorship
- Appoint one author to be the executive author to record authorship and manage correspondence about the work with the publisher and other interested parties.

- Acknowledge all those who have contributed to the research, facilities or materials but who do not qualify as authors, such as research assistants, technical staff, and advisors on cultural or community knowledge.

Included in this thesis are papers or manuscripts in Chapters 2 and 3 which are co-authored with other researchers. My contribution to each co-authored paper is outlined at the front of the relevant chapter. The bibliographic details for these papers including all authors are:

Zhijin Tan, Porun Liu, Haimin Zhang, Yun Wang, Mohammad Al-Mamun, Huagui Yang, Dan Wang, Zhiyong Tang and Huijun Zhao. An in situ vapour phase hydrothermal surface doping approach for fabrication of high performance Co_3O_4 electrocatalysts with an exceptionally high S-doped active surface. *Chem. Commun.*, 2015, 51, 5695—5697.

Zhijin Tan, Wentao Liang, Mohammad Al-Mamun, Porun Liu, Yun Wang, Haimin Zhang, Huijun Zhao. Novel two-step synthesis of S doped Co_3O_4 nanowires arrays as efficient counter electrodes for dye-sensitized solar cells. In preparation.

(Signed) _____ (Date) _____

Zhijin Tan

(Countersigned) _____ (Date) _____

Supervisors: Prof. Huijun Zhao

Dr Porun Liu

Dr Yun Wang

Prof. Haimin Zhang

Table of Contents

Statement of Originality.....	ii
Abstract.....	iii
Acknowledgements.....	v
Table of Contents.....	viii
List of Figures.....	x
List of Tables.....	xii
Chapter 1. General Introduction.....	13
1.1 Backgrounds.....	13
1.2 Solar cells.....	14
1.2.1 Silicon Solar Cell.....	14
1.2.2 Thin film solar cells.....	14
1.2.3 Dye-Sensitised Solar Cells.....	15
1.3 Electrocatalysts.....	20
1.3.1 Metal Catalysts.....	20
1.3.2 Carbon Materials Catalysts.....	21
1.3.3 Transition Metal Compounds.....	23
1.4 Liquid-phase Hydrothermal Method.....	29
1.5 Vapour-phase Hydrothermal Method.....	33
References.....	36
Chapter 2. S-doped Co₃O₄ nanowires arrays as efficient counter electrode materials for dye-sensitized solar cells.....	48
2.1 Introduction.....	50
2.2 Experimental Section.....	53
2.3 Results and Discussion.....	55

2.4 Conclusion.....	67
2.5 Reference.....	68
Chapter 3. An In Situ Vapour Phase Hydrothermal Surface Doping Approach for Fabrication of High Performance Co₃O₄ Electrocatalyst with Exceptionally High S- doped Active Surface.....	73
3.1 Introduction	75
3.2 Results and Discussion	77
3.3 Conclusion.....	81
3.4 Reference.....	81
3.5 Supporting Information.....	84
Chapter 4. Synthesis, characterization of S-doped metal oxides and their photovoltaic activities.....	90
4.1 Introduction	90
4.2 Experimental Section	91
4.3 Results and Discussion	93
4.4 Conclusion.....	96
4.5 Reference.....	97
Chapter 5 General Conclusion and Future Work.....	100

List of Figures

Figure 1.1 General architecture and operating principle of dye-sensitised solar cells.....	17
Figure 1.2 Schematic of a typical stainless autoclave used in the laboratory to perform solution-based synthesis.....	31
Figure 1.3 Diagram of the VPH experimental set-up.....	34
Figure 2.1 Schematic illustration of the VPH doping process.....	56
Figure 2.2 Crystal structure of the Co_3O_4 samples and S-doped Co_3O_4 -6h (denoted as “SCO-6”) samples. (a) XRD data, and (b) room-temperature Raman spectra.....	57
Figure 2.3 a) SEM image, b) TEM image, c) electron diffraction and d) HRTEM image of Co_3O_4 samples.....	58
Figure 2.4 a) top-view SEM image, b) cross-section SEM image, c) TEM image, d) electron diffraction and e) HRTEM image of the SCO-6 sample.....	58
Figure 2.5 XPS spectra a) survey spectra, b) Co 2p, c) O 1s spectra of CO and SCO-6 samples, d) S 2p of SCO-6 sample.....	59
Figure 2.6 (a) J-V curve, (b) cyclic voltammograms, (c) Tafel polarization curves and (d) electrochemical impedance spectroscopy obtained the CO, SCO-6 and commercial Pt electrodes.....	62
Figure 2.7 SEM images of S- Co_3O_4 thin films prepared under VPH treatment with various temperatures (a) 70°C, (b) 90°C, (c) 120°C, and (d) 150°C for 6h	64
Figure 2.8 (a) J-V curve, (b) cyclic voltammograms, (c) Tafel polarization curves and (d) electrochemical impedance spectroscopy obtained with the S- Co_3O_4 samples prepared by VPH approach at various temperatures.....	65
Figure 2.9 SEM images of S- Co_3O_4 thin films prepared at 90 °C for (a) 3h, (b) 6h, (c) 9h and (d) 12h, respectively.....	66

Figure 2.10 (a) J-V curve, (b) cyclic voltammograms, (c) Tafel polarization curves and (d) electrochemical impedance spectroscopy obtained with the S-Co ₃ O ₄ samples prepared by VPH approach with different durations.....	67
Figure 3.1 (a) XRD patterns, (b) Raman spectra of CNS and S-CNS samples; (c) Cross-sectional SEM, (d) TEM and (f) HRTEM image of S-CNS sample.....	77
Figure 3.2 XPS data: (a) survey spectra, (b) Co 2p and (c) O 1s spectra of CNS and S-CNS samples; (d) S 2p spectrum of S-CNS sample.....	79
Figure 3.3 (a) CVs of CNS, S-CNS and Pt electrodes in I ⁻ /I ₃ ⁻ electrolyte. (b) J-V curves of DSSCs with CNS, S-CNS and Pt counter electrodes.....	80
Figure 3.4 Schematic illustration of the atomic arrangements of the clean and I adsorbed S-doped Co ₃ O ₄ (111) surface. Atoms in blue, red, yellow and purple colours represent Co, O, S and I, respectively.....	81
Figure 3.S1 Schematic illustration of the H ₂ S-VPH doping setup.....	88
Figure 3.S2(a) SEM image, (b) TEM image, and (c) HRTEM image of CNS sample.....	88
Figure 3.S3 Consecutive CV curves of a) S-CNS sample and b) Pt in I ⁻ /I ₃ ⁻ electrolyte.....	89
Figure 3.S4 a) Nyquist plots of CNS; b) Nyquist plots and c) Tafel curves S-CNS and Pt electrodes. Inset of b) shows the equivalent circuit.....	89
Figure 4.1 SEM images of a) S-NiO and b) S-Fe ₂ O ₃ film on FTO substrates.	94
Figure 4.2 Cyclic voltammograms comparison of a) NiO/FTO and S-NiO/FTO samples; b) Fe ₂ O ₃ /FTO and S-Fe ₂ O ₃ /FTO samples. The scan rate and scan voltage range are 50mV s ⁻¹ and -0.4–1.2 V vs Ag/AgCl, respectively.....	95
Figure 4.3 Tafel polarization curves for a) NiO/FTO and S-NiO/FTO and b) Fe ₂ O ₃ /FTO and S-Fe ₂ O ₃ /FTO counter electrodes.....	95
Figure 4.4 Photocurrent density–voltage characteristics of FTO, NiO/FTO, S-NiO/FTO, Fe ₂ O ₃ /FTO, S-Fe ₂ O ₃ /FTO and Pt/FTO CEs.....	96

List of Tables

Table 1.1 Photovoltaic Parameters for I_3^-/I^- DSSCs Using Various CEs.....	24
Table 2.1 Photovoltaic parameters of the DSSCs with the CO, SCO-6 and commercial Pt electrodes.....	66
Table 2.2 Photovoltaic parameters of the DSSCs with the S-Co₃O₄ electrodes prepared by VPH approach at various temperatures.....	65
Table 2.3 Photovoltaic parameters of the DSSCs with the S-Co₃O₄ samples prepared by VPH approach with different durations.....	67
Table 3.S1 Photovoltaic parameters and EIS parameters of the DSSCs with different electrodes as counter electrode.....	90
Table 4.1 Photovoltaic performance comparisons of DSSCs using S-NiO/FTO, S-Fe₂O₃/FTO, and Pt/FTO CEs.....	96

Chapter 1. General Introduction

1.1 Backgrounds

Energy is an essential human need for economic growth and socioeconomic activities, while the 80% of all energy consumed worldwide is supported by combustion of fossil fuels. However, energy demand has been exponentially increased in recent decades. For example, the relationship between energy consumption and gross national product (GNP) is studied in both developed and developing countries which shows the growth of GNP accompanying energy consumption increased in several times.¹⁻² Meanwhile, as the increasing growth of population year by year and development of the global industrialization, much more energy is demanded to meet the basic need of human and the development of the world. According to statistics,³ there is a nearly 20-fold increase in world energy use since 1850, and the growth of world population over this period was responsible for 52% of the energy growth, while growth in per capita energy use was responsible for 48% because of increased living standards. Fossil fuels are being consumed with a rate much faster than they are produced. In fact, in 2002, the resource reserves of fossil fuels throughout the whole world were predicted to last 40 years for oil, 60 years for natural gas and 200 years for coal.⁴ Thus energy shortage is becoming as an inevitable issue in coming future limiting the development of the human society.

On the other hand, the consumption of conventional energy (via combustion of coal, petroleum and natural gas) may result in serious environmental contamination like air pollution, water pollution, and greenhouse effects and billions of dollars are used for the environmental remediation annually.⁵⁻⁷ Today, to reduce the reliance on limited traditional fossil energy and the environment pollution during traditional energy production processes, renewable and sustainable sources such as wind energy, solar energy, chemical energy, and biological energy need to be utilized and explored.⁸⁻⁹ Among these renewable energy, solar energy is considered as ideal alternatives to the

conventional fossil source for the generation of electricity which is most used in the residential and industrial areas. In order to explore and use solar energy efficiently, high performance photovoltaic devices have to be used and their fabrication has attracted considerable and persistent attentions.⁹⁻¹⁰ So far, the development of these devices has achieved great progress in many technical aspects after decades of efforts, especially, the energy conversion efficiency has been improved, however, further investigation and development of newly designed devices still deserves to be performed.

1.2 Solar cells

Solar cells are important energy conversion devices the study of solar cell was date back to 1954 when Chapin et al.¹¹ at the Bell Telephone Laboratories demonstrated the first practical p–n junction type solar cell which can convert solar radiation into electric energy with 6% efficiency. There are three main types of solar cells:

1.2.1 Silicon Solar Cell

Photovoltaic cells made from semiconductor-grade silicon quickly became the power source of choice for use on satellites as the advent of the space program, and power conversion efficiencies of these common solar devices were between 15 and 20%.¹² Today, the best single crystal Si solar cells have reached an efficiency of 26%, which is comparable with the theoretical maximum value of 30%.¹³ However, the relatively high cost of manufacturing these silicon cells has prevented the widespread use. Another disadvantage is that the use of toxic chemicals in their manufacture might damage the surrounding environment. These aspects prompted the search for environmentally friendly and low-cost alternatives of single crystal Si solar cells.

1.2.2 Thin film solar cells

Thin film solar cells attracted much attention because they are cheaper and more easily available. The first thin film $\text{Cu}_2\text{S}/\text{CdS}$ cell was based on rather simple and cheap technology known as the ‘Clevite process’, by which several mm-thick CdS film was

deposited on to a metal or metallized plastic substrate, then an acid etch of the CdS film followed by immersion in hot cuprous chlorides solution for few seconds to convert the CdS surface to Cu₂S. The efficiencies of these applied solar cells reached as high as 10%.¹⁴ Then, GaAs, CdTe, Cu₂S, Cu₂O, InP, Zn₃P₂ and their derived alloys and compounds were all studied for photovoltaic applications, among them GaAs and InP are ideal for photovoltaic applications, but they are remarkably expensive for large-scale commercial applications.

1.2.3 Dye-Sensitised Solar Cells

In 1991, Grätzel and co-workers reported the first dye-sensitised solar cells (DSSCs), which attracted attention immediately because of high-efficiency (~12%)¹⁵ on small areas, potential low cost, environmentally friendliness and simple-fabrication procedure. DSSCs became one of the most promising photovoltaics as an alternative to the conventional silicon semiconductor solar cells. A DSSC is mainly composed of dye-sensitized semiconductor electrode (working electrode), redox active electrolyte, and counter electrode (CE).

A typical DSSC is assembled in a sandwich type device with dye anchored nanocrystalline TiO₂ films as photoanode, platinised conductive glass as CE, and I₃⁻/I⁻ in organic solvent as electrolyte solution. The operating mechanism of the DSSCs is shown in Figure.1.1 with different pathways of electron movement. Upon illumination of DSSCs, the dye molecule become photo-excited and ultrafast injection of electron into the conduction band of the semiconductor electrode, then the original state of the dye is subsequently restored by electron donation from the electrolyte. Usually the solution of an organic solvent or ionic liquid solvent containing the I₃⁻/I⁻ redox system.

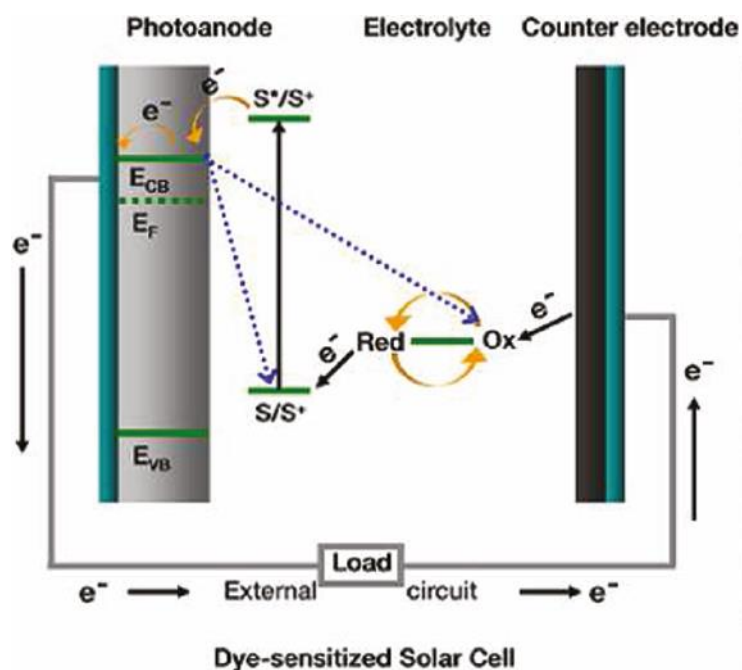


Figure 1.1 General architecture and operating principle of dye-sensitised solar cells.¹⁵

The regeneration of the sensitizer by iodide intercepts the recapture of the conduction band electron by the oxidised dye. The iodide is also regenerated by reduction of triiodide at the CE and hereby the circuit being completed through the external load. The open circuit voltage (V_{oc}) generated under illumination corresponds to the difference between the Fermi level of the electron in the semiconductor electrode and the redox potential of the electrolyte. Overall, electric power is generated without permanent chemical transformation. Along with these processes, electrons in the conduction band of semiconductor may be recombined with the oxidised dye sensitizers or electron acceptor species in the electrolyte solution.

1.2.3.1 Working Electrode

Working electrode plays the role of exciton generated at the dye which is separated into free carriers at the dye–photoelectrode interface. There are two driving forces for this charge separation: the charge separation is energetically favorable because the energy level of the conduction band of the metal oxide is lower than the LUMO of the dye; the charge separation is also entropically favorable as there is larger density of electronic energy states in the conduction band of a crystal than molecular orbital of a

dye. There are different kinds of metal oxides that have been explored so far, for example, TiO₂ Electrodes, ZnO electrodes, Nb₂O₅ electrodes, and ternary photoelectrode materials. Among them, TiO₂ electrodes are mostly commonly used photoanode for DSSCs.¹⁶⁻²⁰

TiO₂ is relatively cheap, abundant, nontoxic, biocompatible semiconducting material that is widely used in healthcare products as well as in paint and other industrial applications. Naturally, TiO₂ exists in three crystalline polymorphs, namely rutile (E_g 3.05 eV), anatase (E_g 3.23 eV), and brookite (E_g 3.26 eV).²¹ In addition, TiO₂ also exist in many other high pressure and metastable forms, e.g., the intermediate orthorhombic, orthorhombic columbite, cotunnite types, monoclinic baddeleyite type and cubic fluorite type.²²⁻²⁵ Out of all polymorphs rutile and anatase have tetragonal structure and rutile is the most common and stable polymorph. On the other hand, brookite is extremely difficult to synthesize in laboratory while both anatase and rutile can be readily prepared.

Anatase TiO₂ is known as an n-type semiconductor, which contains donor-type defects such as oxygen vacancies and titanium interstitials. The Fermi level of anatase is 0.1 eV higher than that of the rutile; therefore, anatase is more preferred for its applications in DSSCs.²⁶ However, recent studies showed that rutile phase can scatter light more effectively resulting pronounced light harvesting property and chemically stable.²⁷⁻²⁸ No significant change in V_{oc} has been reported for anatase and rutile despite the difference in their conduction band edges. But the short circuit current density (J_{sc}) of the DSSCs using rutile phase was about 30% less than those with anatase type photoanodes due to reduced dye loading of rutile particles with lower surface area.²⁷

1.2.3.2 Electrolytes

The electrolyte functions as charge carriers in DSSCs, which collects electrons at the cathode and transfers the electrons back to the photoexcited dye molecule. Regarding to the cell efficiency, the most popularly used electrolyte is the iodide/triiodide (I^-/I_3^-) redox couple in an organic matrix, generally acetonitrile along with some other

additives. In the meanwhile, there are some undesirable intrinsic properties which are inherent of a liquid electrolyte significantly affecting a device's long-term durability and operational stability. For example, not only the leakage of toxic organic solvent will cause environmental contamination, but also the evaporation of volatile iodine ions will lead to an increase in overall internal resistance (reduced concentration of the charge carrier). In order to overcome these disadvantages, research has been conducted to develop non-traditional electrolytes e.g. quasi-solid state and solid-state electrolytes.²⁹

Liquid Electrolyte

Iodide/triiodide (I^-/I_3^-) is the most commonly used liquid electrolyte with outstanding kinetics. The electron injection in to the TiO_2 conduction band occurs in the femto second time range which is much faster than the electron recombination with I_3^- , and the oxidised dye preferably reacts with I^- than combining with the injected electrons. In the electrolyte, the I_3^- diffuses to cathode to harvest electrons and in turn produces I^- which diffuses in the opposite direction towards the TiO_2 electrode to regenerate dye molecules. The diffusion coefficient of I_3^- ions in the porous TiO_2 structure is about $7.6 \times 10^{-6} \text{ cm}^2 \text{ s}^{-1}$.³⁰ According to the theory, the maximum voltage generated in DSSCs is determined by the difference between the quasi-Fermi level of the TiO_2 and the redox potential of the electrolyte, about 0.7 V under solar illumination conditions. To obtain a higher open circuit voltage and circumvent the corrosion of I^-/I_3^- redox couple, a variety of alternative redox couples have been introduced to DSSCs such as Br^-/Br_3^- , $SCN^-/(SCN)_2$, $SeCN^-/(SeCN)^{3-}$, $Fe(CN)_6^{3-/4-}$ and $Co(II)/Co(III)$ complex.³¹⁻³²

Solid-State Electrolyte

To overcome the difficulties of liquid electrolyte, a solid-state electrolyte could be an alternative to liquid electrolyte, because it could achieve better mechanical stability and simplified fabrication process. It is essentially promising to use inorganic p-type semiconductors or organic hole transporting materials (HTM) to eliminate the evaporation and leakage problem of liquid electrolyte. Being a compatible hole-

transport material, it must have a band gap structure reasonable to the highest occupied molecular orbital (HOMO) level of dye sensitizer and conduction band (CB) of TiO₂ to drive charge transfer process easier. So far, the most popular and effective hole-conducting is a p-type organic semiconductor namely, spiro-OMeTAD, which is used in DSSCs and also in perovskite sensitized solar cells as highly efficient hole-conducting materials.²⁹

Quasi-Solid Electrolyte

From the above discussion, it is clearer that the photo conversion efficiency (PCE) is still lower for solid-state electrolyte based solar cells which is mainly related to the poor contact at TiO₂/electrolyte interface along with the lower conductivity of the material.³³ To eliminate such issues, an alternative solution is proposed and attempted where both liquid and solid electrolyte can be combined to form a quasi-solid electrolyte or gel electrolyte.³⁴

1.2.3.3 Counter Electrode

An electrocatalyst participates in electrochemical reactions, which generally functions at electrode surfaces or as the electrode surface itself. Like all other types of catalyst materials, electrocatalysts can modify and increase the rate of chemical reactions without being consumed in the process. For the ideal electrocatalysts, they are supposed to possess electrocatalytic activities with high efficiency, environmental compatibility, and low cost.³⁵⁻³⁶ As the chemical compositions of the catalysts play a determining role in their energy conversion performance, moreover, surface area, structure and morphology of catalysts also affect the electrocatalytical abilities, so catalysts with high surface area and well-defined structure are practically needed in order to reach high efficiency of energy conversion for practical application.³⁷⁻⁴⁰ Due to its wide use in DSSCs, electrocatalysts for iodide/triiodide (I⁻/I₃⁻) redox couple will be focused in this thesis. Also, the electrocatalytic performance of the counter electrode is discussed and evaluated for iodide/triiodide (I⁻/I₃⁻) redox couple if not otherwise specified.

1.3 Electrocatalysts

Recently, the development of material science and nanotechnology has been persistently focused on the design and fabrication of function nanostructured semiconductors. Electrocatalysts used in DSSCs to catalyze the redox reaction of the Iodide/triiodide (I^-/I_3^-) redox couple can be generally divided into three main categories: metal catalysts, carbon material catalysts and transition metal compound catalysts.

1.3.1 Metal Catalysts

DSSCs generally employ platinum (Pt) nanoparticles as their counter electrode materials, which are readily produced by depositing small numbers of prepared Pt nanoparticles by citrate reduction on a substrate. The as deposited Pt materials are highly resistant to corrosive electrolyte environments containing I^- and I_3^- ions. Generally, DSSCs with Pt serving as catalysts on CE showed better performances compared with their Pt-free counterparts.^{35, 41-42}

Recently, Yella et al.⁴³ used Pt nanoparticles as CE for DSSCs and incorporated a Co(II/III) tris (bipyridyl)-based redox electrolyte, leading to a measured power conversion efficiency of 12.3% under simulated air mass 1.5 global sunlight, which created highest record for DSSCs. In addition, Pt alloys were also studied as CE of DSSCs. Pt/NiP electrodes were fabricated by optimising thermal decomposition temperature and Pt loading which showed a high electrocatalytic activity comparable to that of Pt/FTO electrode.⁴⁴

Although pure Pt is a good candidate for electrocatalytic reaction, the current loadings of noble metal do need to be highly reduced or replaced in the light of the economical and realistic factors that the rarity and availability of Pt limit it in large-scale applications. The great efforts have been made to substitute Pt-based catalysts.^{35,}

45-46

1.3.2 Carbon Materials Catalysts

Carbon materials have been extensively studied using in DSSCs. Recent advances in the carbon materials are studied as catalysts and catalyst supports because of low price, environmental friendliness, high conductivity, high electrical and thermal stability.⁴⁷⁻⁴⁸ There are many forms of carbon materials such as carbon black (CB)⁴⁹, graphite⁵⁰, graphene⁵¹, carbon nanotube (CNT). Their properties vary depending on how the carbon atoms are arranged.

1.3.2.1 Carbon Black

Takuro N. Murakami employed carbon black as the catalyst for triiodide reduction on fluorine-doped tin oxide glass substrates (FTO) used as counter electrodes in platinum-free dye-sensitized solar cells and the highest cell efficiency reached as high as 9.1% under 100 mW cm^{-2} light intensity⁵². Huang et al⁵³ investigated carbon black as counter electrodes of DSSC, the overall conversion efficiency of the cell reached 5.7%, which is comparable to 6.5% of platinum-sputtered fluorine-doped tin oxide used as counter electrodes under the same experimental conditions. Recently, porous carbon black layer fabricated by Jung-Min Kim is employed in the DSSCs with energy conversion efficiency of 7.2%, which is similar to the Pt counter electrode with the efficiency of 7.6%.⁴⁹ The performance clarifies the possibility of using carbon as a Pt-free catalyst for triiodide reduction in DSSCs.

1.3.2.2 Carbon Nanotubes (CNTs)

Suzuki et al. applied single-wall carbon nanotubes (SWCNTs) for the CE, which were deposited on both FTO-glass and a Teflon membrane filter achieving conversion efficiencies of 3.5% and 4.5%, respectively.⁵⁴ They found that SWCNTs are good triiodide reduction catalysts. Surprisingly, the surface resistivity of SWCNTs on the Teflon membrane was as low as 1.8 ohm sq^{-1} , which is four times lower than that of FTO-glass (ca. $8\text{-}15 \text{ ohm sq}^{-1}$). Also, a nitrogen-doped carbon nanotube-based bilayer thin film has been used in DSSCs. The counter electrode which is consisted of N-doped

CNTs and pristine CNTs results in efficiencies up to 2.18 %.⁵⁵

Recently, Zheng etc. prepared podlike nitrogen-doped carbon nanotubes encapsulating FeNi alloy nanoparticles (Pod(N)-FeNi) by the direct pyrolysis of organometallic precursors.⁵⁶ DSSCs with Pod(N)-FeNi as the CE presented a power conversion efficiency of 8.82 %. Also, nitrogen-doped carbon nanotubes prepared by direct pyrolysis showed an dramatically increased performances than the previous reported N-doped CNTs.⁵⁵, with a efficiency of 7.48% observed.⁵⁷

1.3.2.3 Graphene and graphite

Graphene, atomically thick planar sheet of sp^2 carbon, has recently attracted widespread interests due to its extraordinary conductivity, large surface area, excellent mechanically flexibility and tuneable physiochemical functionality. The electrocatalytic activity of graphene related materials is sensitive to the preparation techniques and normally it will enhanced after the introduction of defects, dopants or functional groups. Boron-doped graphene, which was synthesized by annealing a mixture of graphite oxide and B_2O_3 , has shown a very high conversion efficiency of 6.73% as a CE for DSSCs.⁵⁸ Also, the common CVD technique is employed by Lin et al. to prepare boron doped graphene.⁵⁹ It showed a much better efficiency than pristine graphene electrodes as CE in quantum dot (CdTe) sensitized solar cells because of the higher electrical conductivity and high work function.⁵⁹

Ganapathy Veerappan's group reported that DSSCs with sub-micrometer-sized graphite as a catalyst on FTO substrate showed an energy conversion efficiency greater than 6.0% under 1 sun illumination (100 mW cm^{-2}), which is comparable to the conversion efficiency of Pt (6.8%) under the same conditions.⁵⁰ Besides, N-Doped graphene/PEDOT composite films were fabricated and used as CE in DSSCs with a 7.1% power conversion efficiency observed which even higher than their Pt counterparts.⁶⁰ Moreover, layer-by-layer self-assembled graphene multilayers were used as Pt-Free counter electrodes in DSSCs, which exhibited 7% energy conversion efficiency.⁶¹ Most recently, nitrogen and sulfur co-doped graphene networks were also synthesized via a simple

hydrothermal route. DSSCs based on the nitrogen and sulfur co-doped graphene exhibited an efficiency of 9.40%, which is higher than the efficiency of the Pt-based device due to synergistic effect of sulfur and nitrogen atoms in graphene.⁶²

1.3.3 Transition Metal Compounds

Several classes of inorganic compounds were introduced into DSSCs as CE catalysts to replace the expensive Pt. Among these materials, early-transition-metal carbides (TMCs, Cr₃C₂, N-doped VC, WC, N-doped TiC, Mo₂C, and N-doped NbC), nitrides (TMNs, TiN, CrN, VN, TiN, MoN, and NbN), oxides (TMOs, Cr₂O₃, V₂O₃, TiO₂, WO₂, MoO₂, Nb₂O₅, and ZrO₂) and chalcogenides (TMChs, NiS, FeS, CoS, Cu₂S, NiSe, FeSe, CoSe and Cu₂ZnSnS₄) have been studied and demonstrated highly intrinsic electrocatalytic activity for the reduction of triiodide. These advanced catalysts not only demonstrate outstanding electrocatalytic activities but also other merits including the high melting temperatures of the ionic crystals, electrical and thermal conductivities and durability of the covalent solid.

Table 1.1 Summarized type, preparation techniques and performance of transitional metal compound electrocatalysts.

Classes	Types of materials	Synthetic techniques	Conversion efficiencies
TMCs	TiC ⁶³	Commercial	7.15%
	WC ⁶⁴	Hydrothermal method	7.01%
	WC ⁶⁵ /WC-MCarbon	Gel	5.35%/8.18%
	MoC ⁶⁵ /MoC-MCarbon	Gel	5.70%/8.34%
	Cr ₃ C ₂ ⁶⁶	Hydrothermal method	5.79%
	VC(N)/VC ⁶⁶	Hydrothermal method	6.38%/4.92%
	ZrC ⁶⁶	Hydrothermal method	3.85%

	NbC(N) ⁶⁶	Hydrothermal method	2.46%
TMNs	Mo ₂ N ⁶⁷	Hydrothermal/CVD	6.04%/6.38%
	W ₂ N ⁶⁷	CVD	5.81%
	TiN ^{66, 68}	Anodization/ Hydrothermal	7.45%/6.23%
	NbN ⁶⁶	Hydrothermal	3.68%
	FeN ⁶⁹	Hydrothermal	2.65%
	MoN ⁶⁹	Hydrothermal	5.57%
	WN ⁶⁹	Hydrothermal	3.67%
	VN ^{63,66}	CVD/Hydrothermal	6.97%/5.92%
	CrN ⁶⁶	Hydrothermal	5.79%
	ZrN ⁶⁶	Hydrothermal	1.20%
TMOs	NbO ₂ ⁶⁷	Sol-Gel	7.88%
	Nb ₂ O ₅ ⁶⁶ (H,O,M) ⁶⁷	Hydrothermal/Sol-Gel	4.84%/4.55-5.82%
	WO ₂ /WO ₃ ⁷⁰	Hydrothermal	7.25%/4.67%
	V ₂ O ₅ /Al ⁷¹	CVD	2%
	V ₂ O ₃ ⁶⁶	Hydrothermal	5.4%
	Cr ₂ O ₃ ⁶⁶	Hydrothermal	1.07%
	TaO ⁷²	Sol-Gel	6.48%
	ZrO ₂ ⁶⁶	Hydrothermal	2.60%
	RuO ₂ ⁷³	hydrothermal process	7.22%

TMChs	NiS ⁷⁴	Electrodeposition(PR)	6.82%
	CoS ⁷⁵	Electrochemical deposition	6.5%
	Cu ₂ ZnSnS ₄ ⁷⁶	Hydrothermal	7.04%

1.3.3.1 Transition-metal carbides (TMCs)

Given the scarcity and high cost of Pt, considerable amount of efforts have been devoted to the development of noble-metal-free electrocatalysts for CEs in DSSCs. In 1973, Levy et al.⁷⁷ first noted that tungsten carbide (WC) demonstrated Pt-like catalytic behavior because of its unique electronic structure. After that, WC has been shown to be an effective catalyst for a number of reactions that are readily catalyzed by platinum, and it has been approved that this is due to changes in the electron distribution when carbon is added to tungsten.⁷⁸⁻⁷⁹ Since then, this catalytic behavior has been found in many early transition metal carbides and metal nitride. Besides WC, other transition metal carbides, such as molybdenum, vanadium, chromium, titanium, niobium and tantalum carbide and nitride, have also been used as catalysts and applied in fuel cells and hydrogenation of aromatic hydrocarbon molecules.⁸⁰⁻⁸¹

The first systematic study of noble-metal-free CEs was carried out by Ma et al⁸² who started to work on improving catalytic performances and decreasing the cost of DSSCs by using substitutes on CE. Before that, a soft chemical urea pathway had been developed by Giordano et al⁸³ who have firstly fabricate a range of diverse metal nitrides and metal carbides (like TiN, VN, NbN, GaN, Mo₂N, W₂N, CrN, NbC(N), TiC(N), WC, Mo₂C, and Cr₃C₂) at a relatively low temperature using urea or close derivatives as both nitrogen or carbon source and the growth controlling system. Specifically, in every case, homogeneous gel-like starting products have been formed that were converted by calcination into the corresponding metal nitrides or metal carbides.⁸³

Ma's group employed hydrothermal technique produced a range of metal carbides

for DSSCs with Pt-like electrocatalytic performance. They prepared Mo₂C and WC nanoparticles and their corresponding composites embedded in ordered nanomesoporous carbon materials (Mo₂C-OMC, WC-OMC) using this simple method. The energy conversion efficiencies of the DSSCs equipped with pure Mo₂C and WC CE devices were 5.70% and 5.35 %, respectively, which were lower than those devices with a Pt CE (7.89%), while those DSSCs devices equipped with MoC-OMC and WC-OMC showed a slightly higher energy conversion efficiency with 8.34% and 8.18%, respectively.⁶⁵ Also, these authors produced Cr₃C₂, N-doped VC [VC (N)], N-doped TiC [TiC-(N)], and N-doped NbC [NbC (N)] using this soft urea pathway to replace the expensive Pt catalyst as CEs in DSSCs. Among these catalysts, except NbC(N) with only 2.46% energy conversion efficiency, they all showed excellent electrocatalytic activity for the reduction of I₃⁻ to I⁻ in the electrolyte, specifically, TiC-(N) had highest energy conversion efficiency at 6.52%, followed by VC (N) with 6.38%, while energy conversion efficiency with Cr₃C₂ CE reached 5.79%.⁶⁶

Other synthetic techniques were also adopted in the preparation of TMCs. For example, mesoporous tungsten carbides were fabricated by Jang et al.⁶⁴ who employed polymer-derived and microwave-assisted methods, for the first time, pure WC without any metallic promoter have been evaluated as Pt-free counter electrodes of DSSCs which showed an excellent activity with 7.01% energy conversion and photovoltaic performances up to 85% of that of the conventional Pt counter electrode. The application of commercial TiC in CE was also evaluated after the purchased TiC had milled for 4 hours using a ball mill and the energy conversion efficiency of the DSSCs was 6.29% using FTO substrate, which was higher than using other substrates like Ti foil substrate with energy conversion efficiency of 5.13%.⁶³

1.3.3.2 Transition-metal Nitrides (TMNs)

The Pt-like electrocatalytic activity was also found in TMNs which can be readily prepared with the aforementioned soft urea hydrothermal method. With this approach, TiN, NbN, ZrN and CrN have been successfully prepared by Wu et al⁶⁶ and tested as

CE catalysts in the solar cells. The obtained TiN nanoparticles showed PCEs of 6.23%, which were lower than the highly ordered TiN nanotubes.⁶⁸ This can be attributed to the highly ordered structures which accelerate electron transfer and thus improve the electrocatalytic activities. For the other three metal nitrides (NbN, ZrN and CrN), decent performances were achieved with 3.68%, 1.20%, and 5.79% respectively. VN was also fabricated using the same technique and deposited on three kinds of low-cost substrates, which showed PCEs of 5.09% coated on bare glass and a little lower than that of FTO substrate (6.29%).

The sputtering method was also employed by these authors to produce molybdenum nitride (Mo_2N) and tungsten nitride (W_2N) films⁶⁷ on flexible Ti sheets as CEs in DSSCs. The DSSCs based on Mo_2N and W_2N CEs achieved power conversion efficiencies of 6.38% and 5.81%, respectively. Other synthetic techniques, for instance, anodization was employed by Gao's group⁶⁸ who produced highly ordered TiO_2 nanotube arrays by the anodization of metallic Ti foil substrate, followed by simple nitridation in an ammonia atmosphere. The as-prepared materials on Ti foil were investigated as counter electrodes of DSSCs for the first time which showed excellent performances with the energy conversion of 7.73%, comparable with a typical fluorine-doped transparent conductive oxide (FTO)/Pt counter electrode. Later on, they also prepared TiN-CNTs composites by thermal hydrolysis of TiOSO_4 on CNTs and subsequent nitridation in an ammonia atmosphere.⁸⁴ DSSCs equipped with these as-synthesized TiN-CNTs as CEs displayed enhanced higher energy conversion (5.41%), compared with their counterparts with only TiN (2.12%) or CNTs (3.13%) under the same conditions.

Similarly, Li et al.⁶⁹ prepared MoN, WN, and Fe_2N nanoparticles by nitridation the metal oxide precursors in an ammonia atmosphere. These materials showed Pt-like electrocatalytic activity for DSSCs, among them, MoN had superior electrocatalytic activity and a higher photovoltaic performance with energy conversion of 5.57%, which was much higher than the other two candidates with 3.67% for WN and 2.65% for Fe_2N , respectively.

1.3.3.3 Transition-metal Oxides (TMOs)

For the class of TMOs, a simple chemical thermal method was employed by Wu et al.⁷⁰ who synthesized WO₂ nanorods and evaluated their electrocatalytic performance as CEs in DSSCs. The DSSCs showed excellent energy conversion of 7.25% which is close to that of a DSSC using Pt CE (7.57%), and much higher than that of the synthesized WO₃ (4.67%).

A sol-gel method was widely used in the preparation of TMOs. Lin et al.⁶⁷ synthesised niobium oxides (Nb₂O₅ and NbO₂) via this pathway. Three types of Nb₂O₅ was obtained by annealing the as-prepared gel at 500, 800 and 1000°C for 3h in nitrogen gas, respectively, while NbO₂ was obtained by annealing at higher temperature (1100 °C) under the same atmosphere. The DSSCs using a NbO₂ CE exhibited a high power conversion efficiency of 7.88%, matching the performance of the conventional Pt electrode (7.65%), whereas Nb₂O₅ showed a decent lower catalytic activity towards triiodide reduction reaction with an energy conversion of 5.65% (500°C), 4.55% (800°C) and 5.82% (1000°C), respectively. Niobium oxides as promising catalysts were also studied by Wu et al.⁶⁶ which showed a 4.84% conversion efficiency. Moreover, the authors also fabricated TMOs like Cr₂O₃, V₂O₃, ZrO₂ by the same technique and applied them in CEs, which showed energy conversions of 1.07%, 5.4% and 2.6%, respectively. Most recently, a tantalum oxide was prepared by Yun et al.⁷² using this sol-gel method and employed as non-Pt CE which demonstrated impressive Pt-like electrocatalytic activity for I₃⁻ reduction in a DSSCs with a high PCE value of 6.48%, up to 90.5% of the Pt-DSSCs (7.16%). Yu etc. reported that ruthenium dioxide (RuO₂) exhibited superior electrocatalytic activities toward triiodide reduction at a rate comparable to that of Pt.⁷³

In addition, CVD was also employed for the preparation of novel function material V₂O₅ with Al by Xia et al.⁷¹ and applied as counter electrode in solid dye-sensitized solar cell with over 2% conversion efficiency, which is comparable with noble Ag counter electrode.

1.3.3.4 Transition-metal chalcogenide (TMChs)

Early transition metal sulphides were also studied for DSSCs as Pt-free CEs. Electrochemical deposition was employed by Wang et al.⁷⁵, for the first time, who prepared CoS nanoparticles on flexible ITO/PEN films as Pt-free CEs. Their results demonstrated that CoS was very effective in catalyzing the reduction of triiodide to iodide in DSSCs yielding 6.5% efficiency, superseding the performance of Pt as an electrocatalyst and could be considered as an extremely promising candidate. Using a similar technique, Sun et al.⁷⁴ electrodeposited nickel sulfides on transparent conductive glass by a facile periodic potential reversal (PR) technique which was used as Pt-free CEs of DSSCs. The nickel sulphide deposited by PR technique showed higher catalytic activity for triiodide reduction in DSSCs (energy conversion efficiency of 6.82%) comparable to the device with conventional Pt coated CEs (7.00%), much higher than those with CEs prepared by common potentiostatic (PS) technique (3.22% efficiency). In addition, combined solution-base techniques were employed by Xin et al.⁷⁶ who synthesized low cost copper zinc tin sulphide nanocrystals by a simple spin-coating process followed by selenization. Power conversion efficiency of the DSSCs equipped with the as-prepared CZTSSe CE has achieved 7.37%, more than twice that of CZTS (3.62%) prepared by the single step.

Moreover, metal selenides ($\text{Co}_{0.85}\text{Se}$ and $\text{Ni}_{0.85}\text{Se}$) have been grown directly on conductive glass substrates by one-step hydrothermal approach, the DSSCs with $\text{Co}_{0.85}\text{Se}$ could achieve higher power conversion efficiency (9.40%) than that with Pt.⁸⁵

1.4 Liquid-phase Hydrothermal Method

From the aforementioned summary of developed electrocatalyst, it is evident that the fabrication of the CEs are decisive to the final electrocatalytic properties. In terms of bottom-up strategies, there are many kinds of approaches employed for the fabrication of electrocatalysts, they can be roughly classified into “hard” approaches and “soft” approaches. The former ones include chemical vapour deposition (CVD)

method, traditional thermal evaporation routes, and oxidation, which are used to fabricate diverse functional semiconductors with novel nanostructures, but the drastic conditions are normally involved in the reaction, such as high temperature, and high pressure, to construct electrocatalytic active sites via atomic rearrangement. For example, the high temperature annealing approach was widely employed for the fabrication of inorganic ceramic solids. Specifically, solid starting materials containing the desired chemical elements are intimately grounded in stoichiometric quantities, and then heated at extreme temperature (usually in excess of 1000 °C) for a period, normally, between hours and days. Extreme temperatures are necessary to enhance inter diffusion of the solid reagents, and thus allow chemical reaction to take place. Since high temperatures and long heating times are used to bring about reactivity, only the most thermodynamically-stable phases can be prepared by this method.⁸⁶

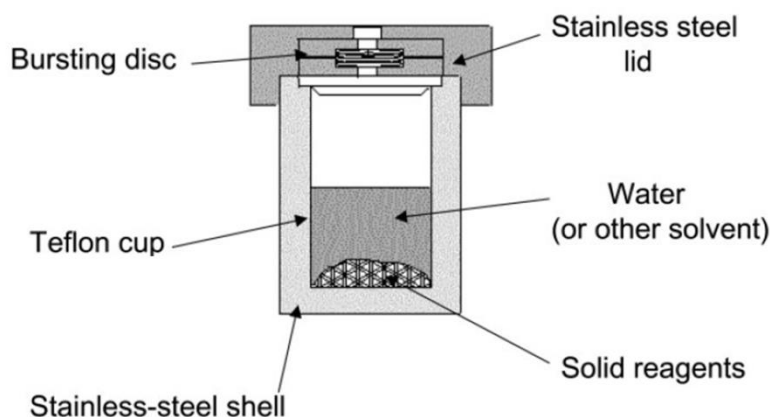


Figure 1.2 Schematic of a typical stainless autoclave used in the laboratory to perform solution-based synthesis

In comparison with “hard” approaches, “soft” ones associated to the material growth induced by thermodynamic dissolution/precipitation equilibrium in solution, can be triggered under mild conditions with much lower temperature, which provide a simple, convenient, environmentally friendly pathway for the fabrication of catalysts. Thus the “soft” approaches have been extensively studied and developed into a promising field in materials chemistry over the last two decades.⁸⁷ Generally, solution-based soft techniques refer to the preparation of products by chemical reactions of substances in a sealed vessel as shown in Figure 1 (i.e. an autoclave) with heated solution above

ambient temperature and pressure, normally, at a temperature higher than the boiling temperature of the solvent.⁸⁸ Solvent, through its physico-chemical properties, plays a key role in solution-based processes. It can act as the following roles in the reaction: (i) to control the orientation of the structural formation with a specific geometric preference for nanocrystallites, for example, crystalline ZnO nanowires and oriented nanorods were prepared under aqueous condition without any templates and surfactants where solvent oriented the growth of arrayed ZnO;⁸⁹ (ii) to manipulate the formation of specific metastable compounds through template action, for example, ethylenediamine has a strong coordination ability towards the divalent metal ions as Fe^{2+} , Co^{2+} and Ni^{2+} , which also acts as template for the growth of the resultant structure (iii) to alter the oxidation–reduction properties of the solvent. For instance, in an solution-based reaction, the solvents like water or ethanol usually provide oxidizing chemical environment that facilitates the growth of oxidized products.⁹⁰ Furthermore, as solvent is an important parameter, the solution-based techniques are divided into hydrothermal, solvothermal and mixed-solvothermal methods according to the different types of solvent used in the reaction.

Among the “soft” approaches, hydrothermal reaction system where only water is used as a solvent is most studied as its good solution’s ability, wide availability and environmental friendliness. Since the pioneering work from the 1960s, hydrothermal technique has achieved a huge success for the fabrication of various types of semiconductors such as metal carbides, metal nitrides, metal chalcogenides, metal oxides and carbon materials with well-defined shape and crystallinity.⁹¹ Basically, the mechanism of hydrothermal reactions follows a liquid-phase nucleation model which is different from that of solid-state reactions, where the action mechanism involves mainly diffusion of atoms or ions at the interface between reactants.⁹² Specifically, a liquid-phase nucleation normally involves two stages. The first one is the formation of supersaturated solutions since the spontaneous appearance of a new phase occurs only when a system is in a non-equilibrium condition. And then, in the next stage, molecules dissolved in solution begin to aggregate, which eventually leads to the formation of

nuclei that can act as centers of crystallization. The subsequent growth, which immediately follows the nucleation, is governed by the diffusion of particles, to the surface of the existing nuclei and their incorporation into the crystal lattice.⁹³ For example, Liu et al who observed the excellent crystallinity of the ZnO nanorods individually grown from the spontaneous nucleation, and then formed the final assemblies.⁹⁰

In the practical reaction system, a range of physical and chemical properties (pressure and temperature) of aqueous solutions can be adjusted in hydrothermal synthesis. Temperature and time duration which are the most important factors in the reaction system can be easily controlled, also it should be noted that the pressure of the reaction system which is another vital factor in reaction, highly depends on the filling ratio of solution and the reaction temperature. For instance, various shapes of ZnO were fabricated at different temperatures under the same other conditions, which clarifies the essential role of impact factors in a practical reaction.⁹⁴

In contrast to conventional synthetic techniques, hydrothermal synthesis offers a number of advantages. Firstly, using hydrothermal synthesis in a closed system can obtain the compounds with elements in oxidation states that are difficult to attain, especially important for the preparation of transition metal compounds⁹⁵. Moreover, it provides a pathway for the phase transformation at low temperature. Rod-like TiO₂ particles and crystallinity of particles were changed from anatase to rutile under hydrothermal treatment at a very low temperature (160 °C) with size and crystallinity remained unchanged.⁹⁶ In comparison, the “hard” approaches, chemical transport reactions of the aimed materials like in a CVD reaction system, reactants normally through the solid-state reaction under high temperature, while much lower temperature is required for the same materials in solution.⁹⁷

1.5 Vapour-phase Hydrothermal Method

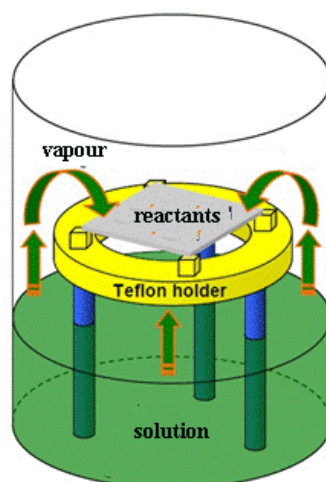


Figure 1.3 Diagram of the VPH experimental set-up

Although there are many advantages of solution-based routes in terms of preparing functional materials with well-defined morphology, structure, and composition, they still have limitations, such as a long reaction time, limited crystal structures under the same crystallisation pathway, solution-sensitive crystallization route (structure change when scale-up), and a residual chemical waste problem as a portion of the organic material is wasted which adheres on to surface of the products and exists in the liquid-phase solution.⁹⁸⁻⁹⁹ In this regards, vapour-phase hydrothermal (VPH) has potential in solving these problems of solution-based reaction, it has been studied and employed as an effective pathway in material fabrication, where the reactants are not directly dissolved in the solvents forming into solution, instead, they are normally deposited on the substrate above the solvents in an autoclave, and the reaction is triggered by the vaporized solvent steam under certain temperature and pressure (Figure 1.3).

VPH method was first reported by Xu et al, who reported the synthesis of zeolite sieve of molecular porosity-5 (ZSM-5) with decreased consumption of organic reagents and higher productivity compared with the traditional solution-based routes.⁹⁸ Moreover, the mixed solvents could be circulated and reused several times in VPH process, leading to an improved utilization of chemicals. Furthermore, VPH approaches

can be used to grow new crystalline materials which it is difficult to be achieved in the liquid-phase hydrothermal method.¹⁰⁰ Last but not least, the crystal phase transformation could also occur with prolonged crystallization, which cannot be realized in solution-based methods.¹⁰¹

The application of VPH method has recently been studied in the fabrication of metal oxides, and a variety of inorganic functional materials with well controlled morphologies and structures have been fabricated. Specifically, Zhang et al.¹⁰² synthesized enhanced photocatalytically active ZnO/TiO₂ layers by immobilizing TiO₂ nanoparticles in a size of 6 nm on the single-crystalline tetrapod-like ZnO under water steam treatment where uniform TiO₂ layers with tunable thickness were formed.¹⁰³ Moreover, an interesting 3D honeycomb structured PS/TTIP hybrid film was transformed into a photoactive TiO₂ film without dismantling the originally templated 3D structure employing VPH approach, which cannot be fabricated by hydrothermal method as the film cannot be formed in the solution.¹⁰³

Not only the formation of various nanostructures, but also the formation mechanisms have been studied under such unique reaction environment. For example, employing VPH approaches, Matsukata et al.¹⁰⁰ firstly reported a growth of zeolite beta that has not been observed in liquid-phase hydrothermal fabrication. Recently, Liu et al. using such a facile VPH method which created unique environment NH₃-saturated water vapour prepared titanate nanotubes direct growth on a titanium foil substrate with larger diameters, and for the first time proved a distinctive nanosheet roll-up mechanism for its formation.¹⁰⁴ They also demonstrated that VPH could realize the growth of novel crystalline phases (orthorhombic HTiOF₃) which has not been reported before.¹⁰⁵ The VPH reaction environment differs remarkably from that of liquid-phase hydrothermal processes, which can be readily used to effectively control the growth of the nanostructure. Interestingly, well-defined ZnO nanotube and nanorod array films were grown on the top and bottom surfaces of the same zinc foil substrate in an reaction, respectively, which means the gravity may also affect the structure and morphology of the resultant products.¹⁰⁶

Under VPH conditions, all reactions and mass transfer occurs within a highly localized thin liquid layer formed on the substrate surface in the reactors, and the dissolved products could rapidly supersaturate in the reaction zone to facilitate the formation of nanostructures, which could dramatically alter the kinetics of dissolution/crystallization, and thereby the crystal growth.¹⁰⁴ However, the full capability of the VPH has not been completely exploited, for example, the strong interaction within the solid/liquid/gas reaction zone could be utilized as a new avenue to control the crystal growth. Since the development of new synthetic procedures has the great potential to allow the discovery of novel functional materials,¹⁰⁷ it is promising to further explore novel approach and its capabilities for the growth of new and novel materials with controllable structural, crystal and electrocatalytic properties for specific application.

In this work, we extend the VPH methods to the fabrication of sulphur doped metal oxides. The introduction of sulphur elements into the materials has converted the metal oxides into high-performance non-precious-metal electrocatalysts. This thesis contains five chapters: a general introduction (Chapter 1), three experimental data chapters (Chapters 2-4) and general conclusion (Chapter 5). Following the introduction in Chapter 1, the VPH doping processes were studied in detail using Co_3O_4 nanowires as candidates in Chapter 2. The resultant S doped Co_3O_4 nanowires films were intensively investigated using as counter electrodes in DSSCs. In Chapter 3, sulphur and spinel-type cobalt oxide (Co_3O_4) are respectively used as the anion dopant and bulk metal oxide to demonstrate the effectiveness of the proposed VPH doping approach. The obtained electrocatalyst exhibits superior electrocatalytic activity for triiodide reduction. In Chapter 4, we further extend the VPH method to a wider spectrum of crystalline metal oxides, such as NiO and Fe_2O_3 and investigate their electrocatalytical activities as CEs in DSSCs. The research findings are summarized and concluded in Chapter 5 and a future research has also been proposed.

This thesis has been prepared in accordance with the Griffith University policy on preparing a MPhil thesis as a series of published and unpublished papers (see the policy

in the section of “All papers included are co-authored”). As a result, there are some differences on the formats and inevitable repetitions among the results chapters, including the descriptions of the studies and the reference lists.

References

1. Chang, J.; Leung, D. Y.; Wu, C.; Yuan, Z., A review on the energy production, consumption, and prospect of renewable energy in China. *Renewable and Sustainable Energy Reviews* **2003**, 7 (5), 453-468.
2. Yu, E. S.; Choi, J.-Y., The causal relationship between energy and GNP: an international comparison. *The Journal of Energy and Development* **1985**, 10 (2), 249-272.
3. Holdren, J. P., Population and the energy problem. *Population & Environment* **1991**, 12 (3), 231-255.
4. Li, B.; Wang, L.; Kang, B.; Wang, P.; Qiu, Y., Review of recent progress in solid-state dye-sensitized solar cells. *Solar Energy Materials and Solar Cells* **2006**, 90 (5), 549-573.
5. Zhang, H.; Chen, G.; Bahnemann, D. W., Photoelectrocatalytic materials for environmental applications. *Journal of Materials Chemistry* **2009**, 19 (29), 5089-5121.
6. Daghrir, R.; Drogui, P.; Robert, D., Photoelectrocatalytic technologies for environmental applications. *Journal of Photochemistry and Photobiology A: Chemistry* **2012**, 238, 41-52.
7. Dapeng, L.; Jiuhui, Q., The progress of catalytic technologies in water purification: A review. *Journal of Environmental Sciences* **2009**, 21 (6), 713-719.
8. Wang, K.; Guo, J.; Yang, M.; Junji, H.; Deng, R., Decomposition of two haloacetic acids in water using UV radiation, ozone and advanced oxidation processes. *Journal of hazardous materials* **2009**, 162 (2), 1243-1248.
9. Chen, H.-Y.; Kuang, D.-B.; Su, C.-Y., Hierarchically micro/nanostructured photoanode materials for dye-sensitized solar cells. *Journal of Materials Chemistry* **2012**, 22 (31), 15475-15489.

10. Li, Y.; Gemmen, R.; Liu, X., Oxygen reduction and transportation mechanisms in solid oxide fuel cell cathodes. *Journal of Power Sources* **2010**, *195* (11), 3345-3358.
11. Chapin, D. M.; Fuller, C.; Pearson, G., A new silicon p-n junction photocell for converting solar radiation into electrical power. *Journal of Applied Physics* **1954**, *25* (5), 676-677.
12. Grant, C. D.; Schwartzberg, A. M.; Smestad, G. P.; Kowalik, J.; Tolbert, L. M.; Zhang, J. Z., Characterization of nanocrystalline and thin film TiO₂ solar cells with poly (3-undecyl-2, 2'-bithiophene) as a sensitizer and hole conductor. *Journal of electroanalytical Chemistry* **2002**, *522* (1), 40-48.
13. Chopra, K.; Paulson, P.; Dutta, V., Thin-film solar cells: an overview. *Progress in Photovoltaics: Research and Applications* **2004**, *12* (2-3), 69-92.
14. Chopra, K. L.; Das, S. R., Why thin film solar cells? In *Thin film solar cells*, Springer: 1983; pp 1-18.
15. Yella, A.; Lee, H.-W.; Tsao, H. N.; Yi, C.; Chandiran, A. K.; Nazeeruddin, M. K.; Diao, E. W.-G.; Yeh, C.-Y.; Zakeeruddin, S. M.; Grätzel, M., Porphyrin-sensitized solar cells with cobalt (II/III)-based redox electrolyte exceed 12 percent efficiency. *science* **2011**, *334* (6056), 629-634.
16. Zhu, K.; Neale, N. R.; Miedaner, A.; Frank, A. J., Enhanced charge-collection efficiencies and light scattering in dye-sensitized solar cells using oriented TiO₂ nanotubes arrays. *Nano letters* **2007**, *7* (1), 69-74.
17. Özgür, Ü.; Alivov, Y. I.; Liu, C.; Teke, A.; Reshchikov, M.; Doğan, S.; Avrutin, V.; Cho, S.-J.; Morkoc, H., A comprehensive review of ZnO materials and devices. *Journal of applied physics* **2005**, *98* (4), 11.
18. Zhang, H.; Wang, Y.; Yang, D.; Li, Y.; Liu, H.; Liu, P.; Wood, B. J.; Zhao, H., Directly Hydrothermal Growth of Single Crystal Nb₃O₇ (OH) Nanorod Film for High Performance Dye-Sensitized Solar Cells. *Advanced Materials* **2012**, *24* (12), 1598-1603.
19. Sancho-Parramon, J.; Janicki, V.; Zorc, H., Compositional dependence of a bsorption coefficient and band-gap for Nb₂O₅-SiO₂ mixture thin films. *Thin Solid Films*

2008, 516 (16), 5478-5482.

20. Burnside, S.; Moser, J.-E.; Brooks, K.; Grätzel, M.; Cahen, D., Nanocrystalline mesoporous strontium titanate as photoelectrode material for photosensitized solar devices: increasing photovoltage through flatband potential engineering. *The Journal of Physical Chemistry B* **1999**, 103 (43), 9328-9332.
21. Bokhimi, X.; Morales, A.; Aguilar, M.; Toledo-Antonio, J.; Pedraza, F., Local order in titania polymorphs. *International journal of hydrogen energy* **2001**, 26 (12), 1279-1287.
22. Dubrovinskaia, N. A.; Dubrovinsky, L. S.; Ahuja, R.; Prokopenko, V. B.; Dmitriev, V.; Weber, H.-P.; Osorio-Guillen, J.; Johansson, B., Experimental and theoretical identification of a new high-pressure TiO₂ polymorph. *Physical Review Letters* **2001**, 87 (27), 275501.
23. Lagarec, K.; Desgreniers, S., Raman study of single crystal anatase TiO₂ up to 70 GPa. *Solid state communications* **1995**, 94 (7), 519-524.
24. Sato, H.; Endo, S., Baddeleyite-Type High-Pressure Phase of TiO₂. *Science* **1991**, 251 (4995), 786.
25. Mattesini, M.; De Almeida, J.; Dubrovinsky, L.; Dubrovinskaia, N.; Johansson, B.; Ahuja, R., High-pressure and high-temperature synthesis of the cubic TiO₂ polymorph. *Physical Review B* **2004**, 70 (21), 212101.
26. Kavan, L.; O'Regan, B.; Kay, A.; Grätzel, M., Preparation of TiO₂ (anatase) films on electrodes by anodic oxidative hydrolysis of TiCl₃. *Journal of Electroanalytical Chemistry* **1993**, 346 (1-2), 291-307.
27. Park, N.-G.; Van de Lagemaat, J.; Frank, A., Comparison of dye-sensitized rutile- and anatase-based TiO₂ solar cells. *The Journal of Physical Chemistry B* **2000**, 104 (38), 8989-8994.
28. Nowotny, M. K.; Sheppard, L. R.; Bak, T.; Nowotny, J., Defect chemistry of titanium dioxide. Application of defect engineering in processing of TiO₂-based photocatalysts. *The Journal of Physical Chemistry C* **2008**, 112 (14), 5275-5300.
29. Bach, U.; Lupo, D.; Comte, P.; Moser, J., Solid-state dye-sensitized mesoporous

TiO₂ solar cells with high proton-to-electron conversion efficiencies. *Nature* **1998**, 395 (6702), 583.

30. Huang, S.; Schlichthörl, G.; Nozik, A.; Grätzel, M.; Frank, A., Charge recombination in dye-sensitized nanocrystalline TiO₂ solar cells. *The Journal of Physical Chemistry B* **1997**, 101 (14), 2576-2582.

31. Daeneke, T.; Uemura, Y.; Duffy, N. W.; Mozer, A. J.; Koumura, N.; Bach, U.; Spiccia, L., Aqueous Dye-Sensitized Solar Cell Electrolytes Based on the Ferricyanide–Ferrocyanide Redox Couple. *Advanced Materials* **2012**, 24 (9), 1222-1225.

32. Wang, M.; Chamberland, N.; Breau, L.; Moser, J.-E.; Humphry-Baker, R.; Marsan, B.; Zakeeruddin, S. M.; Grätzel, M., An organic redox electrolyte to rival triiodide/iodide in dye-sensitized solar cells. *Nature Chemistry* **2010**, 2 (5), 385-389.

33. Kron, G.; Egerter, T.; Werner, J.; Rau, U., Electronic Transport in dye-sensitized nanoporous TiO₂ solar cells comparison of electrolyte and solid-state devices. *The Journal of Physical Chemistry B* **2003**, 107 (15), 3556-3564.

34. Wang, P.; Zakeeruddin, S. M.; Moser, J. E.; Nazeeruddin, M. K.; Sekiguchi, T.; Grätzel, M., A stable quasi-solid-state dye-sensitized solar cell with an amphiphilic ruthenium sensitizer and polymer gel electrolyte. *Nature materials* **2003**, 2 (6), 402-407.

35. Chen, J.; Li, K.; Luo, Y.; Guo, X.; Li, D.; Deng, M.; Huang, S.; Meng, Q., A flexible carbon counter electrode for dye-sensitized solar cells. *Carbon* **2009**, 47 (11), 2704-2708.

36. Alonso-Vante, N., Platinum and Non-Platinum Nanomaterials for the Molecular Oxygen Reduction Reaction. *Chemphyschem* **2010**, 11 (13), 2732-2744.

37. Chen, H. M.; Chen, C. K.; Liu, R. S.; Zhang, L.; Zhang, J.; Wilkinson, D. P., Nano-architecture and material designs for water splitting photoelectrodes. *Chem Soc Rev* **2012**.

38. Grätzel, M., Dye-sensitized solar cells. *Journal of Photochemistry and Photobiology C: Photochemistry Reviews* **2003**, 4 (2), 145-153.

39. Papageorgiou, N., Counter-electrode function in nanocrystalline

photoelectrochemical cell configurations. *Coordination chemistry reviews* **2004**, 248 (13), 1421-1446.

40. Sahoo, N. G.; Pan, Y.; Li, L.; Chan, S. H., Graphene-Based Materials for Energy Conversion. *Advanced Materials* **2012**.

41. Wang, Y.; Zhao, C. Y.; Qin, D.; Wu, M.; Liu, W.; Ma, T. L., Transparent Flexible Pt Counter Electrodes for High Performance Dye-Sensitized Solar Cells. *Journal of Materials Chemistry* **2012**.

42. Peng, W. Q.; Yanagida, M.; Han, L. Y.; Ahmed, S., Controlled fabrication of TiO₂ rutile nanorod/anatase nanoparticle composite photoanodes for dye-sensitized solar cell application. *Nanotechnology* **2011**, 22 (27).

43. Yella, A.; Lee, H. W.; Tsao, H. N.; Yi, C.; Chandiran, A. K.; Nazeeruddin, M. K.; Diau, E. W. G.; Yeh, C. Y.; Zakeeruddin, S. M.; Grätzel, M., Porphyrin-sensitized solar cells with cobalt (II/III)-based redox electrolyte exceed 12 percent efficiency. *Science* **2011**, 334 (6056), 629-634.

44. Wang, G.; Lin, R.; Lin, Y.; Li, X.; Zhou, X.; Xiao, X., A novel high-performance counter electrode for dye-sensitized solar cells. *Electrochimica Acta* **2005**, 50 (28), 5546-5552.

45. Lee, W. J.; Ramasamy, E.; Lee, D. Y.; Song, J. S., Performance variation of carbon counter electrode based dye-sensitized solar cell. *Solar Energy Materials and Solar Cells* **2008**, 92 (7), 814-818.

46. Gao, M. R.; Jiang, J.; Yu, S. H., Solution-Based Synthesis and Design of Late Transition Metal Chalcogenide Materials for Oxygen Reduction Reaction (ORR). *Small* **2012**.

47. Hsieh, C. T.; Yang, B. H.; Lin, J. Y., One-and two-dimensional carbon nanomaterials as counter electrodes for dye-sensitized solar cells. *Carbon* **2011**, 49 (9), 3092-3097.

48. Dai, L.; Chang, D. W.; Baek, J. B.; Lu, W., Carbon nanomaterials for advanced energy conversion and storage. *Small* **2012**.

49. Kim, J. M.; Rhee, S. W., Electrochemical properties of porous carbon black layer

as an electron injector into iodide redox couple. *Electrochimica Acta* **2012**.

50. Veerappan, G.; Bojan, K.; Rhee, S. W., Sub-micrometer-sized Graphite As a Conducting and Catalytic Counter Electrode for Dye-sensitized Solar Cells. *ACS Appl Mater Interfaces* **2011**, 3 (3), 857-862.

51. Chavez, A.; Shaffer, M. S. P.; Boccaccini, A. R., Applications of Graphene Electrophoretic Deposition. A Review. *The Journal of Physical Chemistry B* **2012**.

52. Murakami, T. N.; Ito, S.; Wang, Q.; Nazeeruddin, M. K.; Bessho, T.; Cesar, I.; Liska, P.; Humphry-Baker, R.; Comte, P.; Péchy, P., Highly efficient dye-sensitized solar cells based on carbon black counter electrodes. *Journal of the Electrochemical Society* **2006**, 153 (12), A2255-A2261.

53. Huang, Z.; Liu, X.; Li, K.; Li, D.; Luo, Y.; Li, H.; Song, W.; Chen, L. Q.; Meng, Q., Application of carbon materials as counter electrodes of dye-sensitized solar cells. *Electrochemistry Communications* **2007**, 9 (4), 596-598.

54. Suzuki, K.; Yamaguchi, M.; Kumagai, M.; Yanagida, S., Application of carbon nanotubes to counter electrodes of dye-sensitized solar cells. *Chemistry Letters* **2002**, 32 (1), 28-29.

55. Ju, M. J.; Kim, J. C.; Choi, H.-J.; Choi, I. T.; Kim, S. G.; Lim, K.; Ko, J.; Lee, J.-J.; Jeon, I.-Y.; Baek, J.-B., N-doped graphene nanoplatelets as superior metal-free counter electrodes for organic dye-sensitized solar cells. *ACS nano* **2013**, 7 (6), 5243-5250.

56. Zheng, X.; Deng, J.; Wang, N.; Deng, D.; Zhang, W. H.; Bao, X.; Li, C., Podlike N-Doped Carbon Nanotubes Encapsulating FeNi Alloy Nanoparticles: High-Performance Counter Electrode Materials for Dye-Sensitized Solar Cells. *Angewandte Chemie International Edition* **2014**, 53 (27), 7023-7027.

57. Wu, M.-S.; Ceng, Z.-Z., Bamboo-like nitrogen-doped carbon nanotubes formed by direct pyrolysis of Prussian blue analogue as a counter electrode material for dye-sensitized solar cells. *Electrochimica Acta* **2016**, 191, 895-901.

58. Fang, H.; Yu, C.; Ma, T.; Qiu, J., Boron-doped graphene as a high-efficiency counter electrode for dye-sensitized solar cells. *Chemical Communications* **2014**, 50

(25), 3328-3330.

59. Lin, T.; Huang, F.; Liang, J.; Wang, Y., A facile preparation route for boron-doped graphene, and its CdTe solar cell application. *Energy & Environmental Science* **2011**, *4* (3), 862-865.

60. Paterakis, G.; Raptis, D.; Ploumistos, A.; Belekoukia, M.; Sygellou, L.; Ramasamy, M. S.; Lianos, P.; Tasis, D., N-Doped graphene/PEDOT composite films as counter electrodes in DSSCs: Unveiling the mechanism of electrocatalytic activity enhancement. *Applied Surface Science* **2017**, *423*, 443-450.

61. Rani, A.; Chung, K.; Kwon, J.; Kim, S. J.; Jang, Y. H.; Jang, Y. J.; Quan, L. N.; Yoon, M.; Park, J. H.; Kim, D. H., Layer-by-layer self-assembled graphene multilayers as Pt-free alternative counter electrodes in dye-sensitized solar cells. *ACS applied materials & interfaces* **2016**, *8* (18), 11488-11498.

62. Yu, Z.; Bai, Y.; Wang, Y.; Liu, Y.; Zhao, Y.; Liu, Y.; Sun, K., One-step synthesis of three-dimensional nitrogen and sulfur co-doped graphene networks as low cost metal-free counter electrodes for dye-sensitized solar cells. *Chemical Engineering Journal* **2017**, *311*, 302-309.

63. Wang, Y.; Wu, M.; Lin, X.; Shi, Z.; Hagfeldt, A.; Ma, T., Several highly efficient catalysts for Pt-free and FTO-free counter electrodes of dye-sensitized solar cells. *Journal of Materials Chemistry* **2012**, *22* (9), 4009-4014.

64. Ham, D. J.; Ramasamy, E.; Lee, J.; Lee, J. S., Platinum-free tungsten carbides as an efficient counter electrode for dye sensitized solar cells. *Chem Commun (Camb)* **2010**, *46* (45), 8600-8602.

65. Wu, M.; Lin, X.; Hagfeldt, A.; Ma, T., Low-Cost Molybdenum Carbide and Tungsten Carbide Counter Electrodes for Dye-Sensitized Solar Cells. *Angewandte Chemie International Edition* **2011**, *50* (15), 3520-3524.

66. Wu, M.; Lin, X.; Wang, Y.; Wang, L.; Guo, W.; Qi, D.; Peng, X.; Hagfeldt, A.; Grätzel, M.; Ma, T., Economical Pt-free catalysts for counter electrodes of dye-sensitized solar cells. *J Am Chem Soc* **2012**, *134* (7), 3419-3428.

67. Wu, M.; Zhang, Q.; Xiao, J.; Ma, C.; Lin, X.; Miao, C.; He, Y.; Gao, Y.; Hagfeldt,

- A.; Ma, T., Two flexible counter electrodes based on molybdenum and tungsten nitrides for dye-sensitized solar cells. *Journal of Materials Chemistry* **2011**, *21* (29), 10761-10766.
68. Jiang, Q.; Li, G.; Gao, X., Highly ordered TiN nanotube arrays as counter electrodes for dye-sensitized solar cells. *Chem Commun (Camb)* **2009**, (44), 6720-6722.
69. Li, G.; Song, J.; Pan, G.; Gao, X., Highly Pt-like electrocatalytic activity of transition metal nitrides for dye-sensitized solar cells. *Energy & Environmental Science* **2011**, *4* (5), 1680-1683.
70. Lin, X.; Wu, M.; Wang, Y.; Hagfeldt, A.; Ma, T., Novel counter electrode catalysts of niobium oxides supersede Pt for dye-sensitized solar cells. *Chem Commun (Camb)* **2011**, *47* (41), 11489-11491.
71. Wu, M.; Lin, X.; Hagfeldt, A.; Ma, T., A novel catalyst of WO₂ nanorod for the counter electrode of dye-sensitized solar cells. *Chem Commun (Camb)* **2011**, *47* (15), 4535-4537.
72. Xia, J.; Yuan, C.; Yanagida, S., Novel Counter Electrode V₂O₅/Al for Solid Dye-Sensitized Solar Cells. *ACS Appl Mater Interfaces* **2010**, *2* (7), 2136-2139.
73. Yun, S.; Wang, L.; Guo, W.; Ma, T., The application of non-Pt counter electrode catalysts using tantalum oxide for low-cost dye-sensitized solar cells. *Electrochemistry Communications* **2012**.
74. Hou, Y.; Chen, Z. P.; Wang, D.; Zhang, B.; Yang, S.; Wang, H. F.; Hu, P.; Zhao, H. J.; Yang, H. G., Highly Electrocatalytic Activity of RuO₂ Nanocrystals for Triiodide Reduction in Dye-Sensitized Solar Cells. *Small* **2014**, *10* (3), 484-492.
75. Sun, H.; Qin, D.; Huang, S.; Guo, X.; Li, D.; Luo, Y.; Meng, Q., Dye-sensitized solar cells with NiS counter electrodes electrodeposited by a potential reversal technique. *Energy & Environmental Science* **2011**, *4* (8), 2630-2637.
76. Wang, M.; Anghel, A. M.; Marsan, B.; Cevy Ha, N. L.; Pootrakulchote, N.; Zakeeruddin, S. M.; Grätzel, M., CoS supersedes Pt as efficient electrocatalyst for triiodide reduction in dye-sensitized solar cells. *J Am Chem Soc* **2009**, *131* (44), 15976-

15977.

77. Xin, X.; He, M.; Han, W.; Jung, J.; Lin, Z., Low-Cost Copper Zinc Tin Sulfide Counter Electrodes for High-Efficiency Dye-Sensitized Solar Cells. *Angewandte Chemie International Edition* **2011**, *50* (49), 11739-11742.

78. Levy, R.; Boudart, M., Platinum-like behavior of tungsten carbide in surface catalysis. *Science (New York, NY)* **1973**, *181* (4099), 547.

79. Bennett, L.; Cuthill, J.; McAlister, A.; Erickson, N.; Watson, R., Electronic structure and catalytic behavior of tungsten carbide. *Science* **1974**, *184* (4136), 563-565.

80. Houston, J.; Laramore, G.; Park, R. L., Surface electronic properties of tungsten, tungsten carbide, and Platinum. *Science* **1974**, *185*, 258-260.

81. Ganesan, R.; Lee, J. S., Tungsten Carbide Microspheres as a Noble-Metal-Economic Electrocatalyst for Methanol Oxidation. *Angewandte Chemie International Edition* **2005**, *44* (40), 6557-6560.

82. Neumark, E.; Cohn, M.; Lukanidin, E.; Witz, I.; Ben-Baruch, A., Possible co-regulation of genes associated with enhanced progression of mammary adenocarcinomas. *Immunology Letters* **2002**, *82* (1), 111-121.

83. Ma, T.; Fang, X.; Akiyama, M.; Inoue, K.; Noma, H.; Abe, E., Properties of several types of novel counter electrodes for dye-sensitized solar cells. *Journal of Electroanalytical Chemistry* **2004**, *574* (1), 77-83.

84. Giordano, C.; Erpen, C.; Yao, W.; Milke, B.; Antonietti, M., Metal Nitride and Metal Carbide Nanoparticles by a Soft Urea Pathway. *Chemistry of Materials* **2009**, *21* (21), 5136-5144.

85. Li, G.; Wang, F.; Jiang, Q.; Gao, X.; Shen, P., Carbon Nanotubes with Titanium Nitride as a Low-Cost Counter - Electrode Material for Dye-Sensitized Solar Cells. *Angewandte Chemie International Edition* **2010**, *49* (21), 3653-3656.

86. Gong, F.; Wang, H.; Xu, X.; Zhou, G.; Wang, Z.-S., In situ growth of Co_{0.85}Se and Ni_{0.85}Se on conductive substrates as high-performance counter electrodes for dye-sensitized solar cells. *Journal of the American Chemical Society* **2012**, *134* (26), 10953-10958.

87. Walton, R. I., Subcritical solvothermal synthesis of condensed inorganic materials. *Chem. Soc. Rev.* **2002**, *31* (4), 230-238.
88. Jansen, M., A Concept for Synthesis Planning in Solid-State Chemistry. *Angewandte Chemie International Edition* **2002**, *41* (20), 3746-3766.
89. Michailovski, A.; Patzke, G. R., Hydrothermal synthesis of molybdenum oxide based materials: Strategy and structural chemistry. *Chemistry-A European Journal* **2006**, *12* (36), 9122-9134.
90. Vayssieres, L., Growth of arrayed nanorods and nanowires of ZnO from aqueous solutions. *Advanced Materials* **2003**, *15* (5), 464-466.
91. Liu, B.; Zeng, H. C., Hydrothermal synthesis of ZnO nanorods in the diameter regime of 50 nm. *J Am Chem Soc* **2003**, *125* (15), 4430-4431.
92. Rabenau, A., The role of hydrothermal synthesis in preparative chemistry. *Angewandte Chemie International Edition in English* **2003**, *24* (12), 1026-1040.
93. Feng, S.; Xu, R., New materials in hydrothermal synthesis. *Accounts of chemical research* **2001**, *34* (3), 239-247.
94. Erdemir, D.; Lee, A. Y.; Myerson, A. S., Nucleation of crystals from solution: classical and two-step models. *Accounts of chemical research* **2009**, *42* (5), 621-629.
95. Zhang, H.; Wu, R.; Chen, Z.; Liu, G.; Zhang, Z.; Jiao, Z., Self-assembly fabrication of 3D flower-like ZnO hierarchical nanostructures and their gas sensing properties. *CrystEngComm* **2012**, *14* (5), 1775-1782.
96. Wu, C.; Yin, P.; Zhu, X.; OuYang, C.; Xie, Y., Synthesis of hematite (α -Fe₂O₃) nanorods: Diameter-size and shape effects on their applications in magnetism, lithium ion battery, and gas sensors. *The Journal of Physical Chemistry B* **2006**, *110* (36), 17806-17812.
97. So, W. W.; Park, S. B.; Kim, K. J.; Moon, S. J., Phase transformation behavior at low temperature in hydrothermal treatment of stable and unstable titania sol. *Journal of Colloid and Interface Science* **1997**, *191* (2), 398-406.
98. Yoshida, H.; Takeda, S.; Uchiyama, T.; Kohno, H.; Homma, Y., Atomic-scale in-situ observation of carbon nanotube growth from solid state iron carbide nanoparticles.

Nano Lett **2008**, 8 (7), 2082-2086.

99. Xu, W.; Jinxiang, D.; Li, J.; Wu, F., A novel method for the preparation of zeolite ZSM-5. *Journal of the Chemical Society. Chemical communications* **1990**, (10), 755-756.

100. Matsukata, M.; Ogura, M.; Osaki, T.; Hari Prasad Rao, P. R.; Nomura, M.; Kikuchi, E., Conversion of dry gel to microporous crystals in gas phase. *Topics in Catalysis* **1999**, 9 (1), 77-92.

101. Matsukata, M.; Osaki, T.; Ogura, M.; Kikuchi, E., Crystallization behavior of zeolite beta during steam-assisted crystallization of dry gel. *Microporous and mesoporous materials* **2002**, 56 (1), 1-10.

102. Matsukata, M.; Nishiyama, N.; Ueyama, K., Crystallization of FER and MFI zeolites by a vapor-phase transport method. *Microporous materials* **1996**, 7 (2), 109-117.

103. Zhang, Q.; Fan, W.; Gao, L., Anatase TiO₂ nanoparticles immobilized on ZnO tetrapods as a highly efficient and easily recyclable photocatalyst. *Applied Catalysis B: Environmental* **2007**, 76 (1), 168-173.

104. Zhao, H.; Shen, Y.; Zhang, S.; Zhang, H., A vapor phase hydrothermal modification method converting a honeycomb structured hybrid film into photoactive TiO₂ film. *Langmuir* **2009**, 25 (18), 11032-11037.

105. Liu, P.; Zhang, H.; Liu, H.; Wang, Y.; Yao, X.; Zhu, G.; Zhang, S.; Zhao, H., A Facile Vapor-Phase Hydrothermal Method for Direct Growth of Titanate Nanotubes on a Titanium Substrate via a Distinctive Nanosheet Roll-Up Mechanism. *J Am Chem Soc* **2011**, 133 (47), 19032-19035.

106. Liu, P.; Wang, Y.; Zhang, H.; An, T.; Yang, H.; Tang, Z.; Cai, W.; Zhao, H., Vapor-Phase Hydrothermal Transformation of HTiOF₃ Intermediates into {001} Faceted Anatase Single-Crystalline Nanosheets. *Small* **2012**.

107. Zhang, H.; Li, Y.; Liu, P.; Li, Y.; Yang, D.; Yang, H.; Zhao, H., A New Vapor-Phase Hydrothermal Method to Concurrently Grow ZnO Nanotube and Nanorod Array Films on Different Sides of a Zinc Foil Substrate. *Chemistry-A European Journal* **2012**,

18 (17), 5165-5169.

108. Xia, Y.; Rogers, J. A.; Paul, K. E.; Whitesides, G. M., Unconventional methods for fabricating and patterning nanostructures. *Chemical Reviews-Columbus* **1999**, 99 (7), 1823-1848.

Chapter 2. S-doped Co_3O_4 nanowires arrays as efficient counter electrode materials for dye-sensitized solar cells

(In Preparation)

STATEMENT OF CONTRIBUTION TO CO-AUTHORED PREPARED PAPER

This chapter includes a co-authored paper. The bibliographic details of the co-authored paper, including all authors, are:

Zhijin Tan, Wentao Liang, Mohammad Al-Mamun, Porun Liu, Yun Wang, Haimin Zhang, Huijun Zhao*

S-doped Co₃O₄ nanowires arrays as efficient counter electrode materials for dye-sensitized solar cells

In preparation

My contribution to the paper involved:

Initial concept, experimental design and implementation;

All data collection and analysis;

Preparation of the manuscript.

(Signed)_____ (Date)_____

Name of Student: Zhijin Tan

(Countersigned)_____ (Date)_____

Corresponding author of paper: Huijun Zhao, Porun Liu

(Countersigned)_____ (Date)_____

Supervisor: Prof. Huijun Zhao, Dr Porun Liu, Dr Yun Wang, Prof. Haimin Zhang

2.1 Introduction

Over last decades, there have been increasing interests in the exploitation and utilization of renewable energy among the society due to the concerns about the unprecedented carbon dioxide emissions and fossil fuel deficiency. Dye-sensitized solar cells (DSSCs), since their advent, have emerged as one of the most promising alternatives to the traditional p-n junction solar cells, and attracted widely spread interests due to their simple construction, environmental friendly and cost-effective features. Notable progresses including developed redox couples, organic dye sensitizers, nanostructured TiO₂ photoanode, new electrocatalysts for counter electrode have been achieved to signify the state-of-the-art over 13% power conversion efficiency (PCE). However, the best-performing DSSCs to date are still equipped with high-cost platinum (Pt) electrocatalysts, which impedes economically viable large-scale DSSCs production. Thus, researches have focused on the development of low-cost, highly efficient electrocatalysts to replace dominant Pt as the benchmark materials for high-performance DSSCs.

In classical DSSCs where iodide/tri-iodide (I⁻/I₃⁻) redox couple solution is used as the electrolyte, the role of electrocatalysts is to reduce I₃⁻ to I⁻ while collecting the electrons from external circuit. A competent electrocatalyst is expected to possess i) high catalytic activity towards the reduction of I₃⁻ to suppress the potential I₃⁻ reduction by accepting electrons from excited dye molecules; ii) electrical conductivity to allow efficient electron collection from the counter electrode substrate; iii) long-term stability for elongated function of DSSCs.

The current research strategies to elevate the overall electrochemical performance of Pt-low and Pt-free electrocatalyst include: i) development of wide-ranged electrocatalytic materials, such as carbon materials, polymers, metal compounds (oxides, sulphides,¹⁻² nitrides, carbides and phosphide). Very recently,

the transition metal sulphides (CoMoS₄ and NiMoS₄) have been reported to possess very high electrocatalytic activity towards I₃⁻ reduction;³ ii) creation of active sites *via* nanoscaled engineering, for instance, the synthesis of α-Fe₂O₃ crystals with exposed active (012) and (104) surfaces⁴ or active edge sites established on MoS₂ electrode by patterning;⁵ iii) optimal substrate support, such as mesoporous fluorine-doped tin oxide (FTO)⁶ and tin-doped indium oxide (ITO) nanoarray supports;⁷ iv) utilization of the composite materials for synergetic performance enhancement and improved stabilities.⁸⁻¹² Notably, this strategy has been generally and widely adopted to boost the electrocatalytic performance although deepen understandings on the origin of the synergetic effects is still lacking. v) chemical doping.¹³⁻¹⁹ The incorporation of dopants to materials plays different roles to contribute to the overall electrocatalytic performance. For carbon based materials, such as carbon black, nanotubes, and graphene, the doping of heteroatoms *via* post-doping will produce local strains and structural deformations. The incurred electron charges in the delocalized carbon framework will improve the electro-transfer ability and also electrocatalytic activity without altering the bulk properties.²⁰ For conducting polymer, on the other hand, the introduction of dopant atoms into the polymer structure will induce remarkable enhanced conductivity that facilitate electron transport in the polymer main chain.^{14, 21} Compared to carbon and polymer materials, however, cation²²⁻²³ or anion¹⁷ doped inorganic metal compounds as the counter electrode electrocatalysts for DSSCs have not been much explored. Notably, Li and co-workers reported that PCE of DSSCs using sulphur-doped nickel oxide as counter electrode electrocatalyst was 5.04%, showing much improvement compared to the pristine nickel oxide film (0.31%).¹⁷ However, the relationship between the dopant levels and the electrocatalytic activity remains unclear. We believe that the answer to the question will be a good guidance to further enhancement of the electrocatalytic performance.

In terms of doping approaches, a wide range of techniques have been adopted: solid state reaction, sol-gel method, RF magnetron sputtering, ball milling, electrochemical synthesis, solution-based method and so forth.²⁴ However, despite of the generality of doping process, majority of the preparation procedures involve the use of either high energy (temperature, voltage) or prolonged process time, which usually impair the crystal, structural quality of the matrix materials. Also, incorporation of dopants into the matrix materials is not very effective, normally with the atomic ratio of less than 5% (even on the surface). Additionally, the homogeneity of chemical states of the dopant in some of the products is not satisfactory (yielding dopant with mixed chemical states). To develop a low-energy-consuming, effective, generic doping technique for function material preparation is still a challenge.

Spinel-type cobalt oxide (Co_3O_4) has been an important p-type semiconducting material for heterogeneous catalysis, lithium ion battery, electrochemical pseudocapacitors and gas sensing applications.²⁵⁻²⁶ In this study, it was selected as the potential electrocatalytic materials due to its good catalytic activity, charge capacity and chemical stability. It has been reported that the incorporation of anion dopants (such as nitrogen²⁷⁻²⁸ and fluorine²⁹) in to Co_3O_4 crystals will dramatically enhance the catalytic (Hg oxidation), electrocatalytic (oxygen reduction reaction) and photocatalytic (hydrogen generation) performance of the material. However, there have been few previous researches on the S-doped Co_3O_4 counter electrode electrocatalyst for tri-iodide reduction in DSSCs. In this work, we report the two-step preparation of S- Co_3O_4 crystals on conductive FTO substrate as the counter electrode for DSSCs *via* a facile, low-temperature vapour-phase hydrothermal (VPH) doping technique. The finding in our research is important to the fabrication of alternative, efficient, Pt-free counter electrode electrocatalysts for DSSCs.

2.2 Experimental Section

Chemicals

Cobalt (II) nitrate hexahydrate (98%), Al_2S_3 , and LiClO_4 (98%) and NaNO_3 were obtained from Sigma-Aldrich. Anhydrous LiI , I_2 , and acetonitrile (ACN) were purchased from Merck. 4-tert-Butylpyridine (TBP, 96%) and tert-butanol (TBA, 99.5%) were received from Acros. Ethanol (ACS reagent, 99.5%) was purchased from Aldrich Chemical Co. The commercial TiO_2 electrodes, Pt electrodes and electrolyte were purchased from DyeSol. All chemicals mentioned above were used without further purification. Deionized water (DIW) was used throughout the work.

Fabrication of various S- Co_3O_4 counter electrodes

Thin films of Co_3O_4 nanowire arrays were grown on FTO glass substrates, separately, using chemical bath deposition (CBD) followed by a pyrolysis treatment. In a typical CBD process, a FTO substrate was suspended with the conductive side facing downwards in a container with an aqueous solution containing 6.25wt% of urea and 0.15M (4.4 g) of cobalt nitrate with the volume of 50ml, at different temperatures and durations, respectively.³⁰ The obtained pink films on the FTO were the precursor cobalt hydroxide carbonate, which were converted to the film of Co_3O_4 by pyrolyzing them at 400°C for 2 h in air. Thereafter, the resultant Co_3O_4 films on FTO substrates were placed onto a PTFE holder and doped by vapour-phase hydrothermal (VPH) method with hydrogen sulphur gas that is generated by the reaction of Al_2S_3 (0.26g) and water (60 μl) without direct contact (Figure 2.1). Reactions with various reacting temperatures 70°C, 90°C, 120°C, and 150°C, and durations (3h, 6h, 9h and 12h under 90°C) were also performed, respectively. After reaction, the electrodes are rinsed in CS_2 to remove the elemental sulfurs prior to DSSCs assembly or characterizations.

Fabrication of the DSSCs

TiO_2 electrodes (on FTO substrates) were purchased commercially, and then sintered at 450°C for 30 mins in air. The sintered TiO_2 electrode was coupled with one

of the various CEs (CEs with Co_3O_4 nanowires, S-doped Co_3O_4 nanowires, and Pt) to fabricate the DSSC; these two electrodes were separated by a 60 μm thick Surlyn and sealed by heating. The electrolyte was injected into the space between the two electrodes by a vacuum pump, and the hole was sealed with hot-melt glue after the electrolyte injection.

Characterization

XRD patterns were analysed with a Bruker X-ray diffractometer operated at 40 kV and 30 mA. Raman spectra were collected with a Renishaw Raman spectrometer using 632.8 nm He-Ne laser. The scattered light was detected with a Peltier-cooled CCD detector with a spectral resolution of 2 cm^{-1} . The grating was calibrated using the 520 cm^{-1} silicon band. The X-ray photoelectron spectroscopy (XPS) data was obtained using a Kratos Analytical Axis Ultra X-ray photoelectron spectrometer equipped with a monochromatic Al X-ray source (Al $\text{K}\alpha$, 1.487 keV). The C 1s was used as the charge reference with a binding energy of 284.8 eV. The morphological properties of samples were investigated by a JSM-7001 scanning electron microscope (SEM). The microstructures were examined by field emission TEM Tecnai 20 (F20) with an accelerating voltage of 200kV. Samples were scrapped from FTO substrates, and then they were dispersed in ethanol under ultrasonic. The samples in this suspended liquid were transferred onto TEM copper grids by a drop of the solution.

Cyclic voltammetric (CV) measurements were performed with a CHI 7600 electrochemical workstation (CH Instruments, Inc., USA), using the conventional three-electrode system. One of the various CEs, a platinum sheet, and a Ag/AgCl electrode were used as the working electrode, counter electrode, and reference electrode, respectively. The solution of 10.0 mM LiI, 1.0 mM I_2 , and 0.1 M LiClO_4 in ACN was used as the electrolyte for all CV measurements. CV curves were recorded at a scan rate of 100 mV/s. Tafel polarization curves and electrochemical impedance spectra (EIS) were obtained by symmetrical cells, at a scan rate of 50 mV/s, using a CHI 7600 instrument with a two-electrode system. The symmetrical cell contained two

identical electrodes; the film area was confined to be 0.25 cm^2 by removing the side portions by scrapping. The photocurrent density-voltage characteristic was measured using a computer-controlled scanning potentiostat (Model 362, Princeton Applied Research, US). A 500 W Xe lamp (Trusttech Co., Beijing) with an AM 1.5G filter (Sciencetech, Canada) was used as the light source. The light intensity was measured by a radiant power meter (Newport, 70260) coupled with a broadband probe (Newport, 70268).

2.3 Results and Discussion

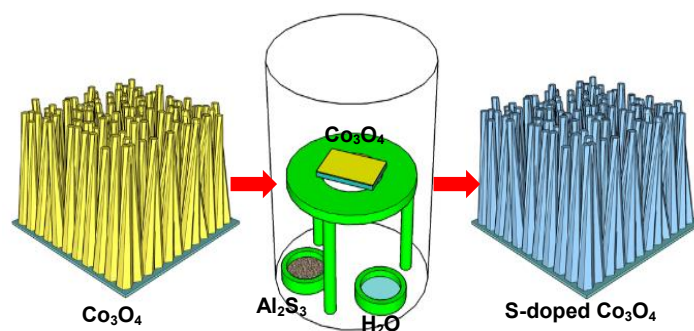


Figure 2.1 Schematic illustration of the VPH doping process.

Sulphur doped cobalt oxide (denoted as “SCO”) thin films were fabricated by VPH treatment of the obtained Co_3O_4 (denoted as “CO”) nanowire arrays grown on the FTO glasses by a two-step process, as shown in Figure 2.1. In the first step, the pink films with the precursor cobalt hydroxide carbonate were formed on the surface of FTO glasses by chemical bath. The thickness of films was controlled by the bath time, the film obtained at $90 \text{ }^\circ\text{C}$ for different numbers of hours were selected for further study (see below). This followed by annealing the precursor at $400 \text{ }^\circ\text{C}$ for 2 h in air to convert precursor cobalt hydroxide carbonate into Co_3O_4 . In the second step, S- Co_3O_4 thin films were achieved by a novel VPH sulphur doping treatment of the as-prepared Co_3O_4 film. The doping process is implemented at various temperatures for short period of time in a closed VPH reactor where H_2S gas was produced by slowly hydrolysis of Al_2S_3 at the presence of trace amount of water vapour generated after initial heating.

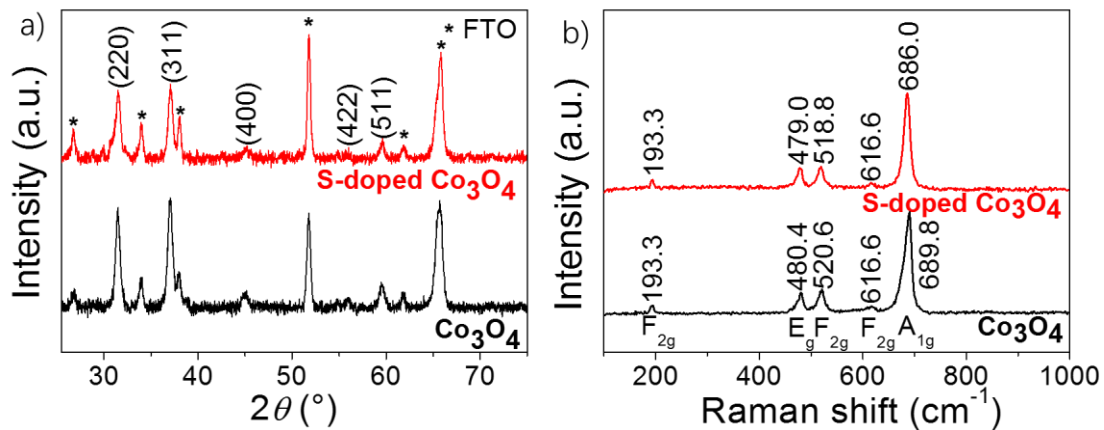


Figure 2.2 Crystal structure of the Co_3O_4 samples and S-doped Co_3O_4 -6h (denoted as “SCO-6”) samples. (a) XRD data, and (b) room-temperature Raman spectra.

The crystal and structural characteristics of CO and S-doped Co_3O_4 obtained under VPH treatment for 6h (SCO-6, best performing sample) were analyzed by X-ray diffraction (XRD) analysis and Raman spectra. The XRD data of film samples before and after VPH doping treatment (Figure 2.2) show similar diffraction patterns. The peaks at $2\theta = 31.5^\circ$, 37.0° , 45.0° , 55.9° and 59.5° are in good consistent with the (220), (311), (400), (422) and (511) planes of spinel Co_3O_4 crystal structure (cubic, $a = 8.056 \text{ \AA}$, space group $Fd\bar{3}m$, JCPDS: PDF-74-1656, ICSD: 27497) while the other peaks are related to the FTO substrate. Minor shifts of the peaks can also be detected (see Figure 2.3), suggesting an increase of lattice strain due to S doping into the oxide lattice.³¹ Room-temperature Raman spectra of these two samples demonstrate 5 peaks which can be ascribed to three F_{2g} modes (at about 193 cm^{-1} , 519 cm^{-1} and 616 cm^{-1}), one E_g mode (at about 480 cm^{-1}) and one A_{1g} mode (at about 688 cm^{-1}) of spinel Co_3O_4 crystals (Figure 2.2b).³² Compared to the peak position in the reference, the data collected in this study show a slightly red shift due to the agglomerated state of nanosized Co_3O_4 particles (see morphology below).³³ Notably, the most dominant peak (A_{1g}) of the S-doped Co_3O_4 sample (686.0 cm^{-1}) has shift to lower frequencies compared to the pristine Co_3O_4 sample (689.8 cm^{-1}). The A_{1g} mode is referred to the symmetric stretching of the Co-O bonds. This observation of shifting may allude to the decrease in the bond strength upon the sulphur doping process.

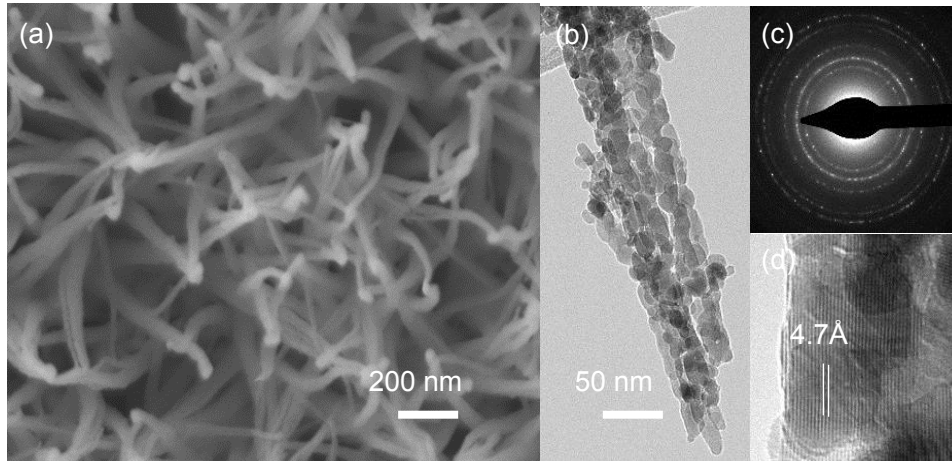


Figure 2.3 a) SEM image, b) TEM image, c) electron diffraction and d) HRTEM image of Co_3O_4 samples.

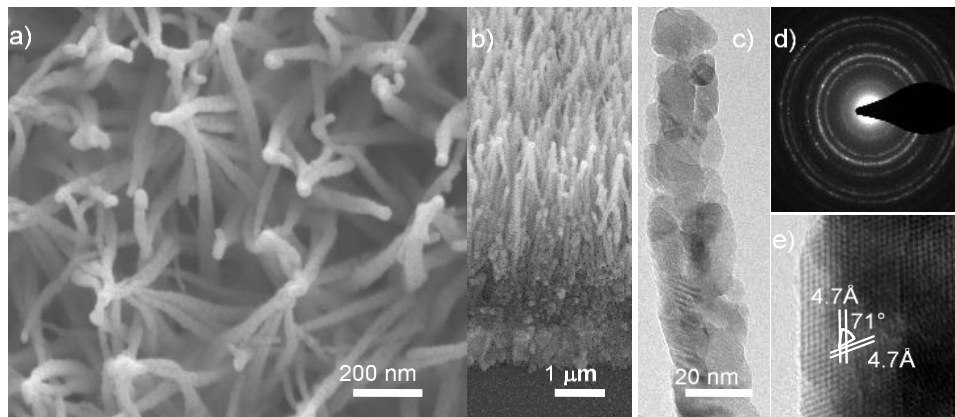


Figure 2.4 a) top-view SEM image, b) cross-section SEM image, c) TEM image, d) electron diffraction and e) HRTEM image of the SCO-6 sample.

The as-synthesized CO and SCO-6 samples were characterized by both scanning electron microscopy (SEM) and transmission electron microscopy (TEM). The SEM images of samples before (Figure 2.3) and after (Figure 2.4) have confirmed that the Co_3O_4 films ($\sim 3\mu\text{m}$ thick, Figure 2.4b) are composed of uniform wire-like array structure, which has been kept intact after VPH doping process. The nanowires, with width of 20 – 50 nm, grow from the substrate and join with neighbor at the top forming bundle like tips. The TEM image reveals that the nanowires are consisted of multiple closely-packed Co_3O_4 nanocrystals with the size of about 5–15 nm. The polycrystalline characteristics of the nanowires have been further confirmed in the electron diffraction

(SAED) pattern (Figures 2.3c and 2.4d). High resolution TEM (HRTEM) image shows lattice spacing of 4.7 Å, in good consistence with the (111) plane of spinel Co_3O_4 crystal structure. The formation of such particle-packed, tip-joined nanowire structure might be a result of the directed growth at the presence of NH_4^+ in the chemical bath preparation reaction (from the hydrolysis of urea). It will provide a good electrical pathway for charge carriers within the nanowire network which is important for practical electrocatalytic application. We also investigated the nanowire structure growth process in chemical bath reaction (results not shown here) and found that insufficient growth tends to yield immature nanowire structure while prolonged reaction will result to thicker film that tend to crack.

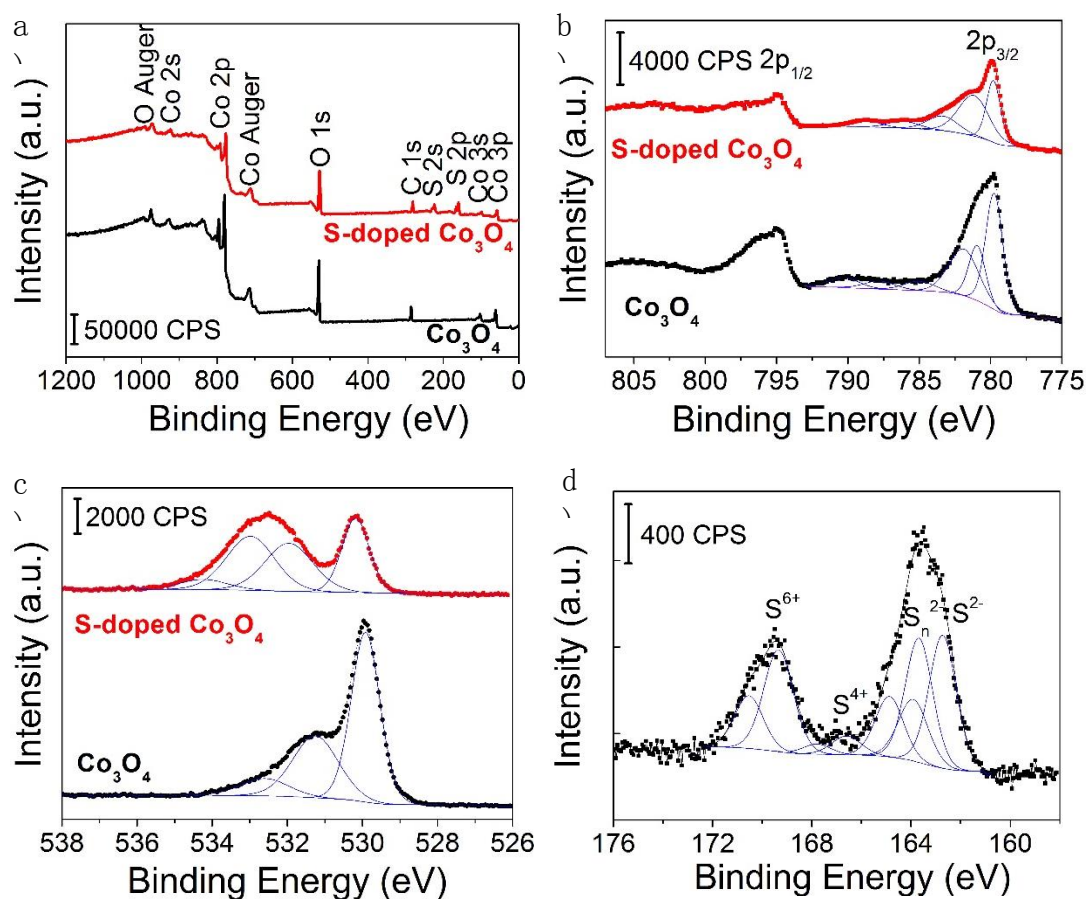


Figure 2.5 XPS spectra a) survey spectra, b) Co 2p, c) O 1s spectra of CO and SCO-6 samples, d) S 2p of SCO-6 sample.

X-ray photoelectron spectroscopy (XPS) was performed to analyse the surface compositions of the samples (Figure 2.5). The elemental distributions on

the surface are Co 19.50%, O 49.59%, C 30.91% for CO sample and Co 16.39%, O 43.34%, C 22.51% and S 17.75% for SCO-6 sample respectively. Notably the relatively high surface sulphur element after VPH doping treatment has been achieved compared to the general low content concentration (<10%). In high-resolution spectra, the Co $2p_{3/2}$ peaks of both CO and SCO-6 samples can be fitted to be three peaks and shake-up satellite peaks that is associated with Co (II) in high spin state. Contrastingly, the two major peaks (centred at 779.7 and 780.9 eV, representing the predominant Co (III)-O and Co (II)-O bonds in the octahedral and tetrahedral oxygen environments, respectively) are shifted to higher binding energy direction (779.8 and 781.2eV), indicating the change of chemical environment due to the incorporation of S atoms. In the O 1s spectrum of CO sample (Figure 2.5c), the peak centered at 531.9 and the other peaks can be assigned to be the lattice oxygen (O_{lat}) and absorbed non-stoichiometric oxygen respectively. It is note that a dramatic decrease in the O_{lat} peak is observed after doping treatment indicating the surface oxygen is substituted by sulphur atoms. Also, new peaks centered at about 534.2 eV appear, which can be attributed to the -O-S-O-, similar to SO_x^{n-} . Furthermore, the S $2p_{3/2}$ peaks of SCO sample centered at 162.7 eV (22.97%), 163.7 eV (21.41%), 166.6 eV (3.44%) and 169.3 (18.87%) are ascribed to be sulfide (S^{2-}), polysulfide (S_n^{2-}), sulfite (SO_3^{2-}) and sulfate species (SO_4^{2-}) on the surface. (Figure 2.5d).

It was reported that the N-doped Co_3O_4 nanoparticles demonstrated good electrocatalytic activity towards oxygen reduction reaction.³⁴ In this study, the resultant S-doped Co_3O_4 film has been used as the counter electrode (CE) catalytic towards tri-iodide reduction in DSSCs. The photocurrent density–voltage ($J-V$) characteristics of DSSCs composed of Co_3O_4 nanowires, S-doped Co_3O_4 nanowires and Pt counter electrodes are presented in Figure 2.6 the detailed photovoltaic parameters of the DSSCs are all listed in Table 2.1. The CE deposited with a Co_3O_4 nanowires film displays a poor photovoltaic performance with a low fill factor (FF) and poor cell efficiency (0.21%). However, after the VPH treatment, the photovoltaic performance

of DSSCs with a S-doped Co_3O_4 nanowires CE was improved significantly in all parameters, with a short-circuit current density (J_{sc}) of 15.03 mA/cm^2 , an open-circuit voltage (V_{oc}) of 0.68V , an FF of 0.66 and a power conversion efficiency (PCE, η) of 6.78% observed. Apparently, the dramatically enhanced cell performance of Co_3O_4 nanowires can be attributed to the presence of S dopants in the latter sample, which improve electrocatalytic activities towards I^-/I_3^- redox reaction and charge transfer activity occurring at the interface of the electrode and the electrolyte.³⁵⁻³⁶ When a commercial Pt film was used as a CE, the photovoltaic parameters were obtained, the corresponding V_{oc} , J_{sc} , FF and PCE are 0.71 V , 18.02 mA/cm^2 , 0.61 , and 7.28% , respectively. A DSSC based on a commercial Pt film exhibited a slightly higher V_{oc} and PCE than that based on S-doped Co_3O_4 nanowires. It is also noted that the DSSCs using S-doped Co_3O_4 nanowires shows higher FF values than that of the DSSC with Pt-CE. This can be attributed to its lower electrochemical impedance compared to that of Pt. The higher cell efficiency of the DSSC with a Pt-CE can be mainly due to its higher J_{sc} .

Cyclic voltammetry measurements were carried out to investigate the electrocatalytic activity of CEs with the films of Co_3O_4 nanowires and S-doped Co_3O_4 nanowires towards the reduction of triiodide, using a Pt/FTO CE as a reference. It can be seen in Figure 2.6b that CV curves of both S-doped Co_3O_4 nanowires and Pt show two pairs of oxidation and reduction peaks in the potential range from -0.4 to 1.2 V , while that of the Co_3O_4 nanowires shows a quite different behavior. The redox pair at more negative potentials is represented by Red-1 and Ox-1, which is attributed to the reaction of $\text{I}_3^- + 2\text{e}^- \rightarrow 3\text{I}^-$ and directly affects the DSSC performance, whereas Red-2 and Ox-2 correspond to the other redox pair at more positive potentials contributed by the reaction $2\text{I}_3^- \rightarrow 3\text{I}_2 + 2\text{e}^-$.^{31, 37} Peak-to-peak separation (E_{pp}) is another important parameter for comparing the electrocatalytic abilities of different electrodes, which is negatively correlated with the standard electrochemical rate. The redox peaks at the negative potentials imply that CV curves of the CEs with S- Co_3O_4 nanowires and Pt have electrocatalytic activity for the reduction of triiodide, while there is no redox peaks observed from CV curve of Co_3O_4 nanowires at the negative potentials, indicating its

poor electrocatalytic activity toward I^-/I_3^- reduction. Notably, the introduction S dopants in Co_3O_4 significantly enhances the electrocatalytic activity for the reduction of I_3^- , especially on the increase of the reduction and oxidation current densities, which make the electrode with a Co_3O_4 film has higher peak current densities than Pt. Although a S- Co_3O_4 nanowires electrode shows higher anodic and cathodic peak current densities than Pt-CE, which also implies a faster I^-/I_3^- reaction rate in the S-doped Co_3O_4 nanowires electrode, the latter one has less E_{pp} value, which may contribute to the better photovoltaic performance of Pt- electrode.³⁸

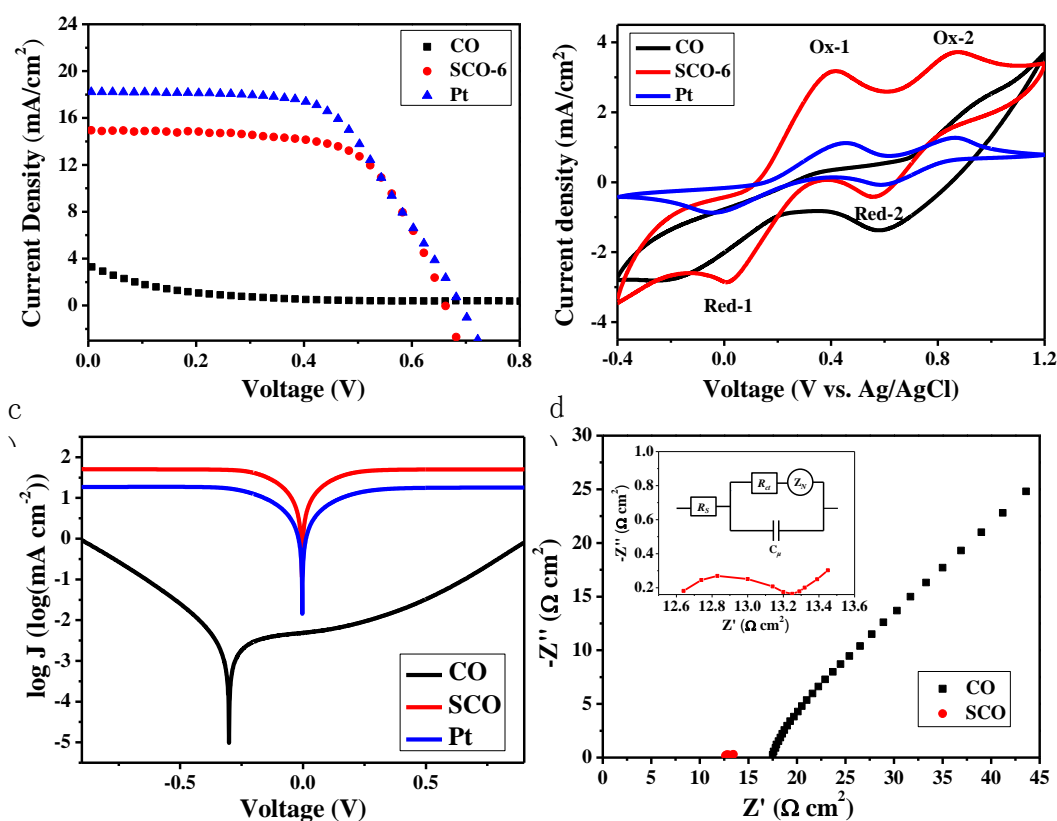


Figure 2.6 (a) J - V curve, (b) cyclic voltammograms, (c) Tafel polarization curves and (d) electrochemical impedance spectroscopy obtained the CO, SCO-6 and commercial Pt electrodes.

Tafel polarization curves are used to further verify the electrocatalytic abilities of CEs for DSSCs as shown in is shown in Figure 2.6d. The horizontal section of the curve can be attributed to the diffusion zone and the curve with a sharp slope can be attributed to the Tafel zone in Tafel polarization curves. The limiting diffusion current density

(J_{lim}) is defined as the intersection of the cathodic branch with the Y-axis. In addition, the intersection of the cathodic branch with the equilibrium potential line, which is the middle dash line, can be considered as the exchange current density (J_o). The film with S-Co₃O₄ nanowires shows higher J_o and J_{lim} than that of Pt, while the CE of Co₃O₄ nanowires possesses poor catalytic property. Also, the tendency of the J_o agrees with that of the peak current density observed in Figure 2.6b. The better performance of S-Co₃O₄ nanowires may be attributed to the much higher surface areas of the film with nanowires arrays.

Table 2.1 Photovoltaic parameters of the DSSCs with the CO, SCO-6 and commercial Pt electrodes.

Sample	J_{sc} (mA/cm ²)	V_{oc} (V)	FF	η (%)	R_s (Ω /cm ²)	R_{ct} (Ω /cm ²)
CO	3.43	0.57	0.11	0.21	-	-
SCO-6	15.03	0.68	0.66	6.78	12.61	0.564
Pt	18.02	0.71	0.61	7.28	12.31	1.18

To gain insight into the electrocatalytic the electrochemical catalyst of different electrodes with the films of Co₃O₄ nanowires, S-Co₃O₄ nanowires, and Pt in the reduction of I₃⁻, electrochemical impedance analyses (EIS) spectra of these CEs were measured using a sealed symmetric cell, consisting of two identical CEs properties of the deposited films on FTO glass substrates. Nyquist plots were illustrated in Figs 6d, in which the semicircle corresponds to the charge-transfer process occurring at the interface of the electrode and the electrolyte, which directly relates to the electrocatalytic activity of the CE for the reduction of triiodide ions, and the diameter of the semicircle represents the resistance of the electrochemical reaction. Specifically, the high frequency intercept on the real axis corresponds to the Ohmic series resistance (R_s), which includes the sheet resistance of two identical electrodes and the resistance of electrolyte, and span of a single semi-circle along the real axis from high to low frequency (R_{ct}) represents the charge-transfer resistance at the electrode–electrolyte interface for the I₃⁻ reduction.³⁹⁻⁴⁰ Also, the observed arch in the low frequency region indicates the diffusion resistance of the redox couple in the electrolyte. The data of R_s and R_{ct} are summarized in above Table 2.1. In an electrochemical reaction, a smaller

diameter of the semicircle indicates a lower resistance of electrochemical reaction with a faster electron transfer rate. As it is shown that Co_3O_4 is a semiconductor with high impedance, which means it has a lower charge carrier mobility and relatively poor conductivity compared with Pt, therefore, the electron transport from the thin film to a FTO substrate is limited and thus DSSCs based on a Co_3O_4 film show a poor photovoltaic performance. However, the resistance of S- Co_3O_4 is decreased dramatically with S dopants, and it is even lower than Pt, which highly improves the electron transport and thus electrocatalytic activity. These impedance measurements are consistent with the obtained CV results and Tafel curves.

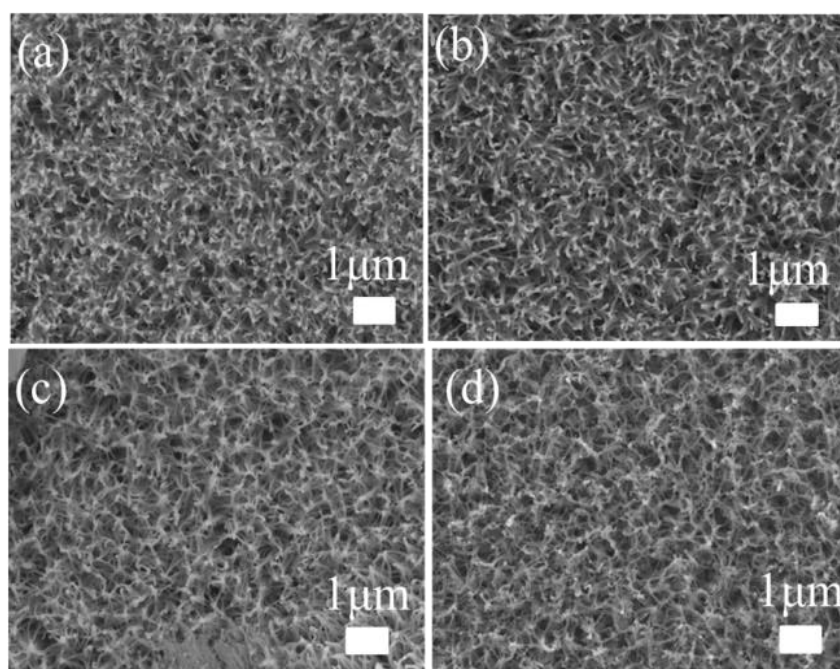


Figure 2.7 SEM images of S- Co_3O_4 thin films prepared under VPH treatment with various temperatures (a) 70°C, (b) 90°C, (c) 120°C, and (d) 150°C for 6h.

The influence of VPH temperature on the electrocatalytic properties of resultant S- Co_3O_4 thin films has been investigated. Figure 2.7 shows SEM images of S- Co_3O_4 thin films obtained under VPH treatment for 6h, with a reaction temperature varying from 70°C to 150 °C. At 150 °C, the corruption of the nanowire arrays was observed probably

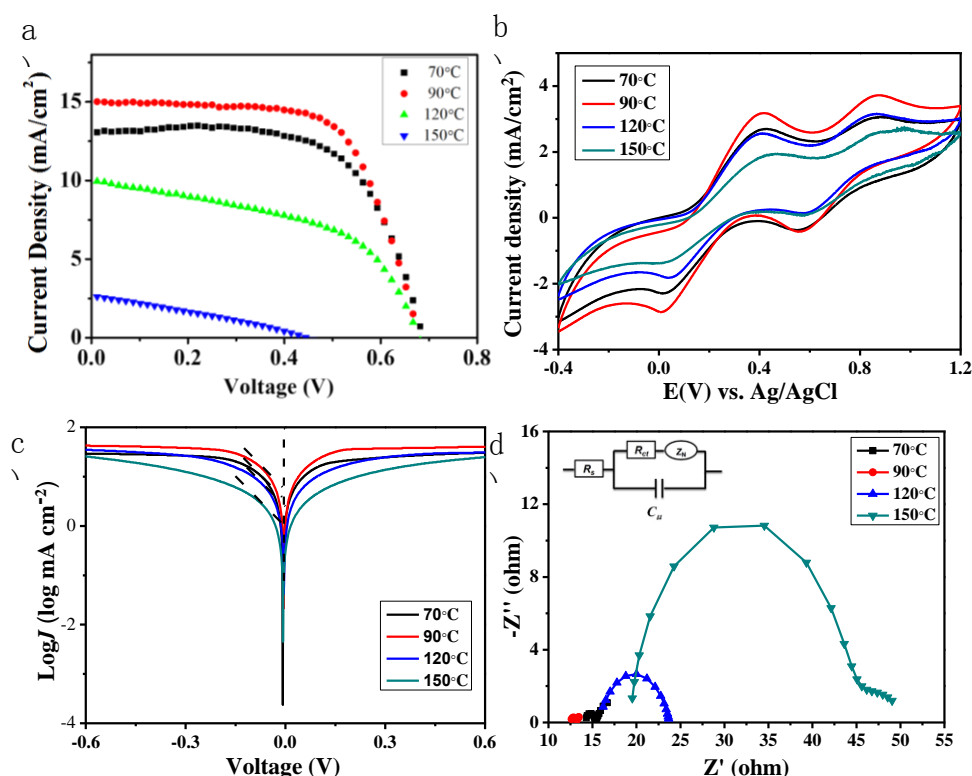


Figure 2.8 (a) J - V curve, (b) cyclic voltammograms, (c) Tafel polarization curves and (d) electrochemical impedance spectroscopy obtained with the S-Co₃O₄ samples prepared by VPH approach at various temperatures.

Table 2.2 Photovoltaic parameters of the DSSCs with the S-Co₃O₄ electrodes prepared by VPH approach at various temperatures.

Sample	J_{sc} (mA/cm ²)	V_{oc} (V)	FF	η (%)	R_s (Ω /cm ²)	R_{ct} (Ω /cm ²)
70°C	13.08	0.67	0.68	6.03	14.20	1.064
90°C	15.03	0.68	0.66	6.78	12.61	0.564
120°C	10.01	0.68	0.50	3.44	15.72	8.037
150°C	2.67	0.45	0.29	0.35	19.29	23.92

due to the quick reaction between H₂S and Co₃O₄ thin films. When higher temperature was used, i.e., 180°C, the S-Co₃O₄ thin films began to peel off from the FTO substrate. Although, there was no significant morphology change observed between 70°C to 120°C, the reaction temperature have significant effects on the photovoltaic performance of S-Co₃O₄ thin film counter electrodes for DSSCs (Figure 2.8). Figure 2.8a and Table 2.2 show the S-Co₃O₄ nanowire film prepared at 90°C exhibits the best photovoltaic performance, with a highest FF and best cell efficiency. Also, CV of S-Co₃O₄ nanowires samples show two pairs of oxidation and reduction peaks in the

potential range from -0.4 to 1.2 V in I^-/I_3^- solution, while the current intensity of the sample obtained at 90 °C surpasses those obtained at other temperature (Figure 2.8b). Consistently, Tafel polarization curves (Figure 2.8c) and the EIS data (Figure 2.8d) of S-Co₃O₄ sample prepared at 90 °C demonstrate a much higher J_o and smaller charge transfer resistance compared to other S-Co₃O₄ samples. The possible explanation for this observation could be the VPH doping process require thermal energy to facilitate and the dopant could not effectively be introduced into the Co₃O₄ lattice at low temperature. On the contrary, the vapor pressure may be increased at higher temperature which would potentially deteriorate the structural stability of the S-Co₃O₄ nanowire leading to a poor connectivity between adjacent particles. This argument is partly supported by the relatively low FF in $J-V$ data and higher charge transfer resistance in EIS data (Figure 2.8).

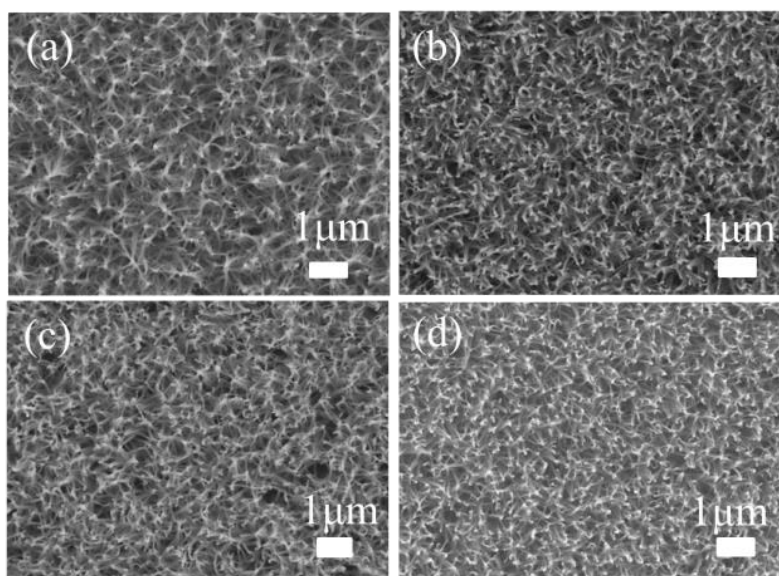


Figure 2.9 SEM images of S-Co₃O₄ thin films prepared at 90 °C for (a) 3h, (b) 6h, (c) 9h and (d) 12h, respectively.

Our results also illustrate a strong dependence of the photovoltaic performance on the duration of the VPH treatment. Figure 2.9 shows the SEM images of the SCO samples after VPH treatment at 90 °C with different durations, e.g., 3h, 6h, 9h and 12h. Again, it is evident that the no structural change is noticeable even with 12 h VPH

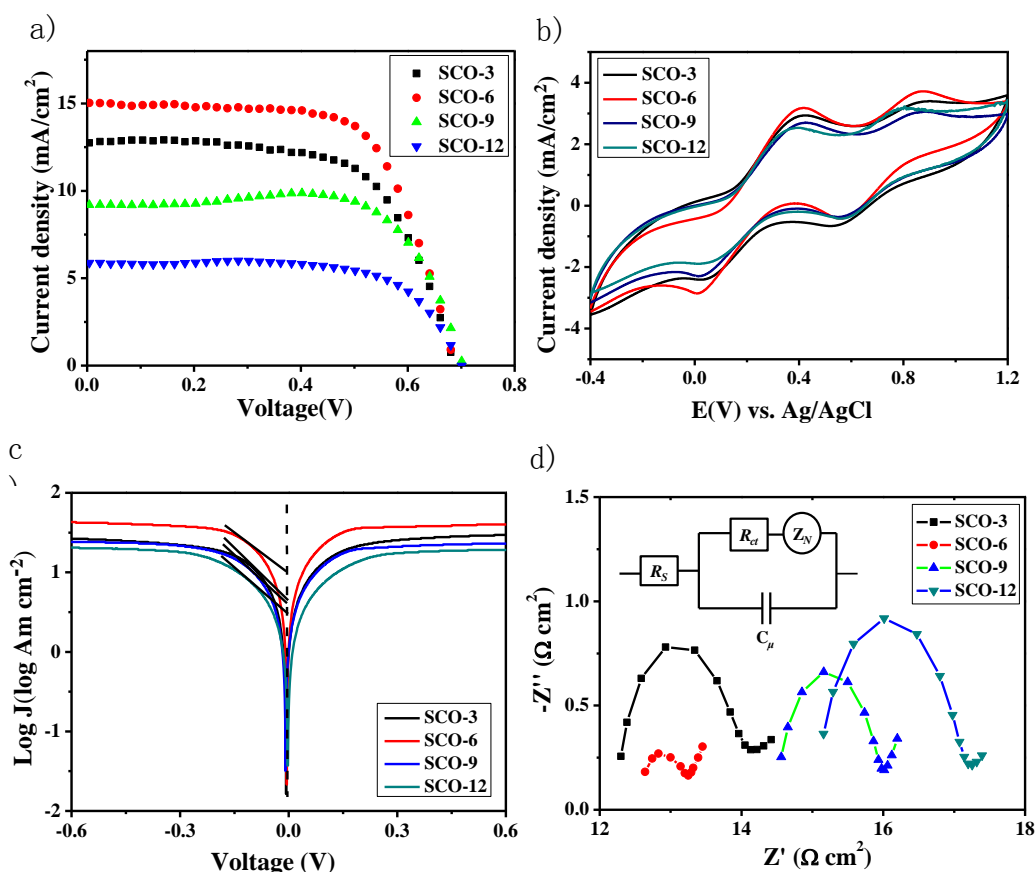


Figure 2.10 (a) J - V curve, (b) cyclic voltammograms, (c) Tafel polarization curves and (d) electrochemical impedance spectroscopy obtained with the S- Co_3O_4 samples prepared by VPH approach with different durations.

Table 2.3 Photovoltaic parameters of the DSSCs with the S- Co_3O_4 samples prepared by VPH approach with different durations.

Sample	J_{sc} (mA/cm^2)	V_{oc} (V)	FF	η (%)	R_s (Ω/cm^2)	R_{ct} (Ω/cm^2)
SCO-3	12.74	0.69	0.65	5.67	12.25	1.393
SCO-6	15.03	0.68	0.66	6.78	12.61	0.564
SCO-9	9.21	0.70	0.73	4.74	14.49	1.438
SCO-12	5.91	0.70	0.69	2.84	15.05	1.948

treatment at 90°C . Nevertheless, the DSSCs with these SCO electrodes perform distinctively differently as the J - V curves shown in Figure 2.10a, Table 2.3. SCO-6 outperforms the other counterparts with much higher J_{sc} while other photovoltaic parameters, i.e., V_{oc} , FF are relatively comparable. This is consistent with the CV, Tafel plots and EIS data showing similar current densities, exchange current density and

charge transfer resistance. Although the extra reason for this observed trend is still unclear, it implies that an intermediate or equilibrium may exist during the interfacial VPH reaction between Co_3O_4 and H_2S gas. Excessive reaction may change the structural properties of Co-S species that deactivate the surface. Another possibility could be associated with the fact that elemental sulphur could be generated and deposited within the porous space within the nanowire during VPH treatment. Elongated VPH reaction could lead to sulphur blockage within the nanopores in the nanowire films that could not be easily removed in the post-treatment CS_2 washing procedure.

2.4 Conclusion

In summary, we have successfully synthesized sulphur doped Co_3O_4 nanowires thin films by VPH method. The reacting temperature and duration play important roles in determining the sulphur doping process. The fabricated Co_3O_4 nanowires thin films and S- Co_3O_4 nanowires thin films were tested as counter electrodes in a DSSC device. The DSSCs based on Co_3O_4 nanowires thin films showed poor photovoltaic performance, while their S- Co_3O_4 counterparts demonstrate significantly improved electrocatalytic activities towards triiodide reduction reaction in DSSCs, and lead to an energy conversion efficiency of 6.78%, which is comparable to those of DSSCs made of commercial Pt CEs (7.36%). This significant increase in the photovoltaic performance can be attributed to sulphur species introduced during VPH treatment. More importantly, the demonstrated highly effective VPH doping approach could be used to convert low cost, earth abundant metal oxides into high performance electrocatalyst that could potentially replace Pt for large-scale applications of DSSCs in the future.

2.5 Reference

1. Li, Y.; Wang, H.; Zhang, H.; Liu, P.; Wang, Y.; Fang, W.; Yang, H.; Li, Y.; Zhao, H., A {0001} faceted single crystal NiS nanosheet electrocatalyst for dye-sensitised solar cells: sulfur-vacancy induced electrocatalytic activity. *Chemical Communications* **2014**, 50 (42), 5569-5571.
2. Al-Mamun, M.; Zhang, H.; Liu, P.; Wang, Y.; Cao, J.; Zhao, H., Directly hydrothermal growth of ultrathin MoS₂ nanostructured films as high performance counter electrodes for dye-sensitised solar cells. *RSC Advances* **2014**.
3. Zheng, X.; Guo, J.; Shi, Y.; Xiong, F.; Zhang, W. H.; Ma, T.; Li, C., Low-cost and high-performance CoMoS₄ and NiMoS₄ counter electrodes for dye-sensitized solar cells. *Chem Commun* **2013**, 49 (83), 9645-7.
4. Hou, Y.; Wang, D.; Yang, X. H.; Fang, W. Q.; Zhang, B.; Wang, H. F.; Lu, G. Z.; Hu, P.; Zhao, H. J.; Yang, H. G., Rational screening low-cost counter electrodes for dye-sensitized solar cells. *Nature communications* **2013**, 4, 1583.
5. Zhang, J.; Najmaei, S.; Lin, H.; Lou, J., MoS₂ atomic layers with artificial active edge sites as transparent counter electrodes for improved performance of dye-sensitized solar cells. *Nanoscale* **2014**, 6 (10), 5279-5283.
6. Bao, C.; Huang, H.; Yang, J.; Gao, H.; Yu, T.; Liu, J.; Zhou, Y.; Li, Z.; Zou, Z., The maximum limiting performance improved counter electrode based on a porous fluorine doped tin oxide conductive framework for dye-sensitized solar cells. *Nanoscale* **2013**, 5 (11), 4951-7.
7. Jiang, Y.; Zhang, X.; Ge, Q. Q.; Yu, B. B.; Zou, Y. G.; Jiang, W. J.; Song, W. G.; Wan, L. J.; Hu, J. S., ITO@Cu₂S tunnel junction nanowire arrays as efficient counter electrode for quantum-dot-sensitized solar cells. *Nano Lett* **2014**, 14 (1), 365-72.
8. Zheng, X.; Deng, J.; Wang, N.; Deng, D.; Zhang, W. H.; Bao, X.; Li, C., Podlike N-Doped Carbon Nanotubes Encapsulating FeNi Alloy Nanoparticles: High-Performance Counter Electrode Materials for Dye-Sensitized Solar Cells. *Angewandte Chemie* **2014**.
9. Xu, H.; Zhang, C.; Wang, Z.; Pang, S.; Zhou, X.; Zhang, Z.; Cui, G., Nitrogen-

doped carbon and iron carbide nanocomposites as cost-effective counter electrodes of dye-sensitized solar cells. *Journal of Materials Chemistry A* **2014**, 2 (13), 4676.

10. Wang, L.; Shi, Y.; Wang, Y.; Zhang, H.; Zhou, H.; Wei, Y.; Tao, S.; Ma, T., Composite catalyst of rosin carbon/Fe₃O₄: highly efficient counter electrode for dye-sensitized solar cells. *Chem Commun (Camb)* **2014**, 50 (14), 1701-3.

11. Yun, S.; Zhang, H.; Pu, H.; Chen, J.; Hagfeldt, A.; Ma, T., Metal Oxide/Carbide/Carbon Nanocomposites: In Situ Synthesis, Characterization, Calculation, and their Application as an Efficient Counter Electrode Catalyst for Dye-Sensitized Solar Cells. *Advanced Energy Materials* **2013**, 3 (11), 1407-1412.

12. Peng, S.; Zhu, P.; Wu, Y.; Mhaisalkar, S. G.; Ramakrishna, S., Electrospun conductive polyaniline–polylactic acid composite nanofibers as counter electrodes for rigid and flexible dye-sensitized solar cells. *RSC Advances* **2012**, 2 (2), 652.

13. Yang, D.-S.; Kim, C.; Song, M. Y.; Park, H.-Y.; Kim, J. C.; Lee, J.-J.; Ju, M. J.; Yu, J.-S., N-Doped Hierarchical Hollow Mesoporous Carbon as Metal-Free Cathode for Dye-Sensitized Solar Cells. *The Journal of Physical Chemistry C* **2014**, 140225093917000.

14. Hwang, D. K.; Song, D.; Jeon, S. S.; Han, T. H.; Kang, Y. S.; Im, S. S., Ultrathin polypyrrole nanosheets doped with HCl as counter electrodes in dye-sensitized solar cells. *Journal of Materials Chemistry A* **2014**, 2 (3), 859.

15. Fang, H.; Yu, C.; Ma, T.; Qiu, J., Boron-doped graphene as a high-efficiency counter electrode for dye-sensitized solar cells. *Chem Commun (Camb)* **2014**, 50 (25), 3328-30.

16. Ahn, H. J.; Kim, I. H.; Yoon, J. C.; Kim, S. I.; Jang, J. H., p-Doped three-dimensional graphene nano-networks superior to platinum as a counter electrode for dye-sensitized solar cells. *Chem Commun (Camb)* **2014**, 50 (19), 2412-5.

17. Guai, G. H.; Leiw, M. Y.; Ng, C. M.; Li, C. M., Sulfur-Doped Nickel Oxide Thin Film as an Alternative to Pt for Dye-Sensitized Solar Cell Counter Electrodes. *Advanced Energy Materials* **2012**, 2 (3), 334-338.

18. Lee, K. S.; Lee, W. J.; Park, N. G.; Kim, S. O.; Park, J. H., Transferred vertically

aligned N-doped carbon nanotube arrays: use in dye-sensitized solar cells as counter electrodes. *Chem Commun (Camb)* **2011**, 47 (14), 4264-6.

19. Ju, M. J.; Kim, J. C.; Choi, H.-J.; Choi, I. T.; Kim, S. G.; Lim, K.; Ko, J.; Lee, J.-J.; Jeon, I.-Y.; Baek, J.-B.; Kim, H. K., N-Doped Graphene Nanoplatelets as Superior Metal-Free Counter Electrodes for Organic Dye-Sensitized Solar Cells. *ACS Nano* **2013**, 7 (6), 5243-5250.

20. Yu, D.; Nagelli, E.; Du, F.; Dai, L., Metal-Free Carbon Nanomaterials Become More Active than Metal Catalysts and Last Longer. *The Journal of Physical Chemistry Letters* **2010**, 1 (14), 2165-2173.

21. Lee, Y. W.; Do, K.; Lee, T. H.; Jeon, S. S.; Yoon, W. J.; Kim, C.; Ko, J.; Im, S. S., Iodine vapor doped polyaniline nanoparticles counter electrodes for dye-sensitized solar cells. *Synthetic Metals* **2013**, 174, 6-13.

22. Joseph, D. P.; Ganesan, S.; Kovendhan, M.; Suthanthiraraj, S. A.; Maruthamuthu, P.; Venkateswaran, C., Fabrication of dye sensitized solar cell using Cr doped Cu-Zn-Se type chalcopyrite thin film. *physica status solidi (a)* **2011**, 208 (9), 2215-2219.

23. Kim, B.-M.; Son, M.-K.; Kim, S.-K.; Hong, N.-Y.; Park, S.; Jeong, M.-S.; Seo, H.; Prabakar, K.; Kim, H.-J., Improved performance of CdS/CdSe quantum dot-sensitized solar cells using Mn-doped PbS quantum dots as a catalyst in the counter electrode. *Electrochimica Acta* **2014**, 117, 92-98.

24. McFarland, E. W.; Metiu, H., Catalysis by Doped Oxides. *Chemical Reviews* **2013**, 113 (6), 4391-4427.

25. Wang, X.; Tian, W.; Zhai, T.; Zhi, C.; Bando, Y.; Golberg, D., Cobalt(ii,iii) oxide hollow structures: fabrication, properties and applications. *Journal of Materials Chemistry* **2012**, 22 (44), 23310-23326.

26. Sun, H.; Ang, H. M.; Tade, M. O.; Wang, S., Co₃O₄ nanocrystals with predominantly exposed facets: synthesis, environmental and energy applications. *Journal of Materials Chemistry A* **2013**, 1 (46), 14427-14442.

27. Yu, H.; Li, Y.; Li, X.; Fan, L.; Yang, S., Electrochemical preparation of N-doped cobalt oxide nanoparticles with high electrocatalytic activity for the oxygen-reduction

- reaction. *Chemistry* **2014**, *20* (12), 3457-62.
28. Mei, Z.; Shen, Z.; Wang, W.; Zhang, Y., Novel Sorbents of Non-Metal-Doped Spinel Co₃O₄ for the Removal of Gas-Phase Elemental Mercury. *Environmental Science & Technology* **2007**, *42* (2), 590-595.
29. Gasparotto, A.; Barreca, D.; Bekermann, D.; Devi, A.; Fischer, R. A.; Fornasiero, P.; Gombac, V.; Lebedev, O. I.; Maccato, C.; Montini, T.; Van Tendeloo, G.; Tondello, E., F-Doped Co₃O₄ photocatalysts for sustainable H₂ generation from water/ethanol. *J Am Chem Soc* **2011**, *133* (48), 19362-5.
30. Kung, C.-W.; Lin, C.-Y.; Li, T.-J.; Vittal, R.; Ho, K.-C., Synthesis of Co₃O₄ thin films by chemical bath deposition in the presence of different anions and application to H₂O₂ sensing. *Procedia Engineering* **2011**, *25*, 847-850.
31. Wu, M.; Lin, X.; Wang, Y.; Wang, L.; Guo, W.; Qi, D.; Peng, X.; Hagfeldt, A.; Grätzel, M.; Ma, T., Economical Pt-free catalysts for counter electrodes of dye-sensitized solar cells. *Journal of the American Chemical Society* **2012**, *134* (7), 3419-3428.
32. Hadjiev, V. G.; Iliev, M. N.; Vergilov, I. V., The Raman spectra of Co₃O₄. *Journal of Physics C: Solid State Physics* **1988**, *21* (7), L199.
33. Lorite, I.; Romero, J. J.; Fernández, J. F., Effects of the agglomeration state on the Raman properties of Co₃O₄ nanoparticles. *Journal of Raman Spectroscopy* **2012**, *43* (10), 1443-1448.
34. Yu, H.; Li, Y.; Li, X.; Fan, L.; Yang, S., Electrochemical preparation of N-doped cobalt oxide nanoparticles with high electrocatalytic activity for the oxygen-reduction reaction. *Chemistry - A European Journal* **2014**, *20* (12), 3457-62.
35. Wang, M.; Anghel, A. M.; Marsan, B. t.; Cevey Ha, N.-L.; Pootrakulchote, N.; Zakeeruddin, S. M.; Grätzel, M., CoS supersedes Pt as efficient electrocatalyst for triiodide reduction in dye-sensitized solar cells. *Journal of the American Chemical Society* **2009**, *131* (44), 15976-15977.
36. Lin, J.-Y.; Liao, J.-H.; Hung, T.-Y., A composite counter electrode of CoS/MWCNT with high electrocatalytic activity for dye-sensitized solar cells. *Electrochemistry*

Communications **2011**, *13* (9), 977-980.

37. Zhao, W.; Zhu, X.; Bi, H.; Cui, H.; Sun, S.; Huang, F., Novel two-step synthesis of NiS nanoplatelet arrays as efficient counter electrodes for dye-sensitized solar cells.

Journal of Power Sources **2013**, *242*, 28-32.

38. Guai, G. H.; Leiw, M. Y.; Ng, C. M.; Li, C. M., Sulfur-Doped Nickel Oxide Thin Film as an Alternative to Pt for Dye-Sensitized Solar Cell Counter Electrodes.

Advanced Energy Materials **2012**, *2* (3), 334-338.

39. Kung, C.-W.; Chen, H.-W.; Lin, C.-Y.; Huang, K.-C.; Vittal, R.; Ho, K.-C., CoS acicular nanorod arrays for the counter electrode of an efficient dye-sensitized solar cell.

ACS nano **2012**, *6* (8), 7016-7025.

40. Bi, H.; Zhao, W.; Sun, S.; Cui, H.; Lin, T.; Huang, F.; Xie, X.; Jiang, M., Graphene films decorated with metal sulfide nanoparticles for use as counter electrodes of dye-

sensitized solar cells. *Carbon* **2013**, *61*, 116-123.

Chapter 3. An *In Situ* Vapour Phase Hydrothermal Surface Doping Approach for Fabrication of High Performance Co_3O_4 Electrocatalyst with Exceptionally High S-doped Active Surface

(published)

STATEMENT OF CONTRIBUTION TO CO-AUTHORED PREPARED PAPER

This chapter includes a co-authored paper. The bibliographic details of the co-authored paper, including all authors, are:

Zhijin Tan, Porun Liu,* Haimin Zhang, Yun Wang, Mohammad Al-Mamun, Hua Gui Yang, Dan Wang, Zhiyong Tang and Huijun Zhao*

An *In Situ* Vapour Phase Hydrothermal Surface Doping Approach for Fabrication of High Performance Co₃O₄ Electrocatalyst with Exceptionally High S-doped Active Surface

Chem. Commun., 2015, 51, 5695—5697

My contribution to the paper involved:

Initial concept, experimental design and implementation;

All data collection and analysis;

Preparation of the manuscript.

(Signed)_____ (Date)_____

Name of Student: Zhijin Tan

(Countersigned)_____ (Date)_____

Corresponding author of paper: Huijun Zhao, Porun Liu

(Countersigned)_____ (Date)_____

Supervisor: Prof. Huijun Zhao, Dr Porun Liu, Dr Yun Wang, Prof. Haimin Zhang

3.1 Introduction

A facile *in-situ* vapour-phase hydrothermal (VPH) surface doping approach has been developed for fabrication of high-performance S-doped Co_3O_4 electrocatalyst with an unprecedentedly high surface S content (>47%). The demonstrated VPH doping approach could be useful for enrichment of surface active sites for other metal oxide electrocatalysts.

Electrocatalyst plays a critical role in energy conversion technologies such as solar and fuel cells. To date, high-performance electrocatalysts used for these applications are mainly fabricated by noble metals that are precious and scarce, hindering their widespread use. Extensive efforts have therefore been made to develop non-precious-metal-based electrocatalysts using carbon-based hybrid electrocatalysts, transition metal alloys, oxides, chalcogenides, nitrides, phosphides, carbides and metal/organic composites.¹

For developing non-precious-metal-based high-performance electrocatalysts, a central task is the pursuit of effective and efficient means to introduce rich catalytic active sites into the materials. Various active site creation/enrichment strategies have been reported such as morphological control, surface engineering and anchoring onto porous supports.² Among them, introducing exterior elements into existing material structures (doping) has been proven to be an effective approach.³ Furthermore, available evidences suggest that the richness of active sites in the resultant electrocatalyst closely depends on the dopant content.⁴ However, introducing a high dopant content via the majority of the reported bulk doping approaches is highly challenging because high dopant contents are destructive to the original crystal structures.⁵ This is particularly true for anions doped electrocatalysts where the maximum dopant contents are generally less than 10%.^{3a, 6}

It is well known that the activity of an electrocatalyst is determined by its surface active sites rather than those bulk ones.⁷ Therefore, developing new doping approaches to realise selective surface high-content doping and non-destructive to the bulk material structures is highly desirable.

In this work, we venture to extend the VPH methods⁸ for selective doping high content of exterior anion elements on the surface of metal oxides. Sulphur and spinel-type cobalt oxide (Co_3O_4) are respectively used as the anion dopant and bulk metal oxide to demonstrate the effectiveness of the proposed doping approach. An unprecedented 47% doped S content on the surface of Co_3O_4 nanosheets can be achieved, leading to a dramatically enhanced electrocatalytic performance. Although versatile applications of Co_3O_4 in catalysis have been reported,⁹ the anion-doped Co_3O_4 catalysts have rarely been investigated.^{6b, 10}

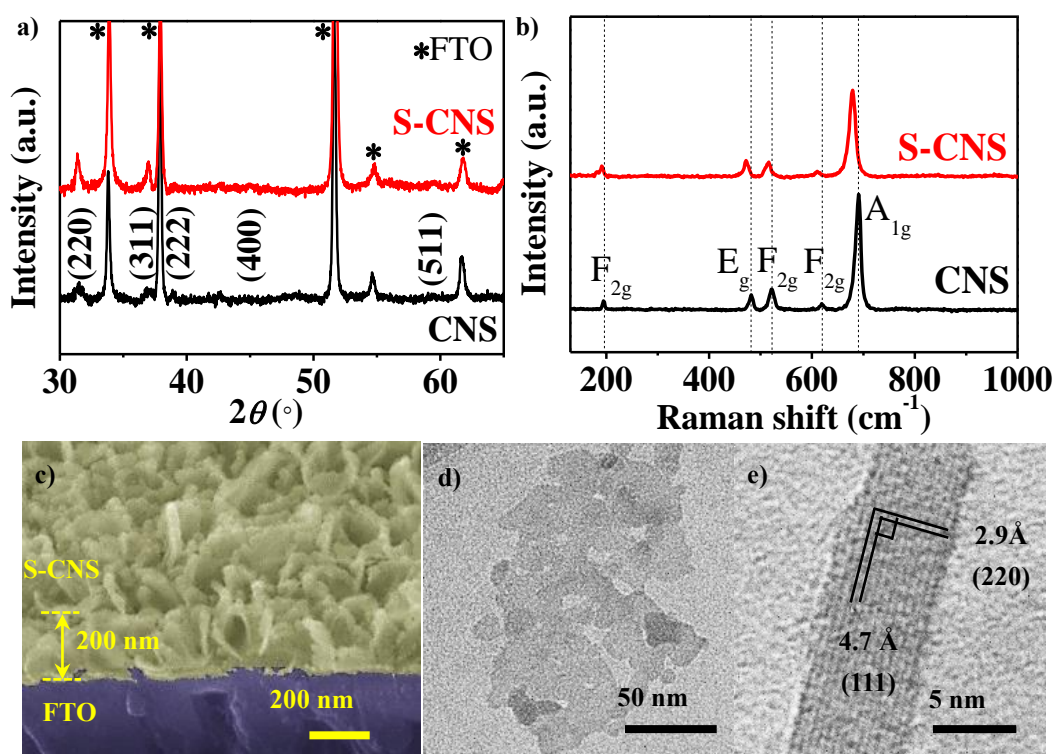


Figure 3.1 (a) XRD patterns, (b) Raman spectra of CNS and S-CNS samples; (c) Cross-sectional SEM, (d) TEM and (f) HRTEM image of S-CNS sample.

3.2 Results and Discussion

The Co₃O₄ nanosheets coated FTO (denoted as “CNS”) was firstly prepared via electrodeposition followed by sintering. Figure 3.S1 schematically illustrates the *in-situ* VPH doping approach. Briefly, the synthesised CNS as the doping substrate is suspended in a VPH reactor containing Al₂S₃ and a small quantity of water as the doping reactants. The VPH doping is carried out at a low temperature of 90°C for 6 h to obtain the S-doped Co₃O₄ nanosheets (denoted as “S-CNS”). An initial heating will generate water vapour, triggering a slow hydrolysis reaction of Al₂S₃ to produce H₂S gas that acts as the S doping source.

X-ray diffraction (XRD) data of the samples before and after VPH doping treatment show similar diffraction patterns (Figure 3.1a) that can be assigned to spinel Co₃O₄ crystal structure (cubic, $a = 8.056 \text{ \AA}$, space group $Fd-3m$, JCPDS: PDF-74-1656, ICSD: 27497). However, the S-CNS sample shows diffraction peaks being slightly shifted ($\Delta 2\theta = 0.15^\circ$) towards lower angle due to the increased lattice constants resulting from S doping.¹¹ These results confirm that there is no significant change in the bulk crystal structures of S-CNS sample. The room-temperature Raman spectra of both samples reveal 5 distinctive peaks ascribable to spinel Co₃O₄ crystals (Figure 3.1b).¹² Notably, compared to CNS, all peaks observed from S-CNS appear at lower frequencies, indicating an increases surface structural disorder and decreased bond strength of S-doped Co₃O₄.

Scanning electron microscopic (SEM) observations of the samples before (Figure 3.S2) and after (Figure 3.1c) S doping confirm that CNS and S-CNS samples are composed of a 200nm layer of uniformly coated nanosheets (~6 nm in thickness) and the VPH doping process has no noticeable effect on the nanosheet structure. The transmission electron microscope (TEM) image reveals that the nanosheets are formed by multiple closely-packed single crystals (Figure 3.1d). The high resolution TEM (HRTEM) image shows that these nanosheets

are mainly bounded with Co_3O_4 {111} facets (Figure 3.1e), further confirming the well-maintained bulk Co_3O_4 crystals after VPH doping.

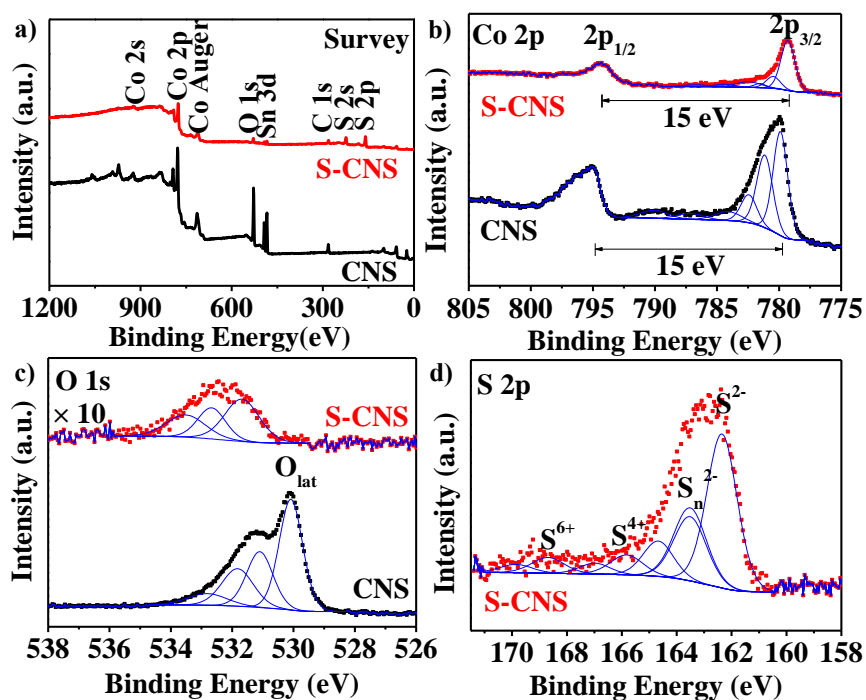


Figure 3.2 XPS data: (a) survey spectra, (b) Co 2p and (c) O 1s spectra of CNS and S-CNS samples; (d) S 2p spectrum of S-CNS sample.

Figure 3.2a shows the X-ray photoelectron spectroscopy (XPS) data of CNS and S-CNS samples. The measured surface contents of S-CNS by XPS are Co 15.25%, O 11.55%, S 47.22%, C 24.81% and Sn 1.17% (from FTO). The confirmed 47% surface doped S content without affecting the bulk Co_3O_4 crystal structure is unprecedented as the S contents of S-doped metal oxides published to date are less than 10% due to the destruction of high contents of doped S to the original metal oxide crystal structures.¹³ The effectiveness and superiority of the VPH doping approach can be attributed to the unique H_2S -rich vapour reaction environment that enables a selective surface doping at mild conditions (90°C).

The high-resolution Co 2p_{3/2} spectra (Figure 3.2b) can be fitted to three main peaks and several weak shake-up satellite peaks (referred to Co (II) in high spin

state). The split spin-orbit of 2p (ΔE) are 15 eV for both samples, consistent with the reported values for Co_3O_4 crystals. The Co $2p_{3/2}$ peak (centred at 779.9 eV) is shifted to 779.3 eV, close to that of Co_3S_4 (779.0 eV).¹⁴ For the O 1s spectra (Figure 3.2c), the peak centred at 529.6 observed from CNS can be assigned to the lattice oxygen (O_{lat} , Co-O) and the rest of the peaks are attributed to absorbed non-stoichiometric oxygen. Notably, the O_{lat} peak of S-CNS vanishes while others shift towards higher binding energies. Importantly, the surface O replacement by S can be confirmed from the observed main S $2p_{3/2}$ peak centred at 162.4eV (assigned to Co-S) and the minor peak centred at 163.5eV (related to S_n^{2-} species) from S-CNS (Figure 2.2d).

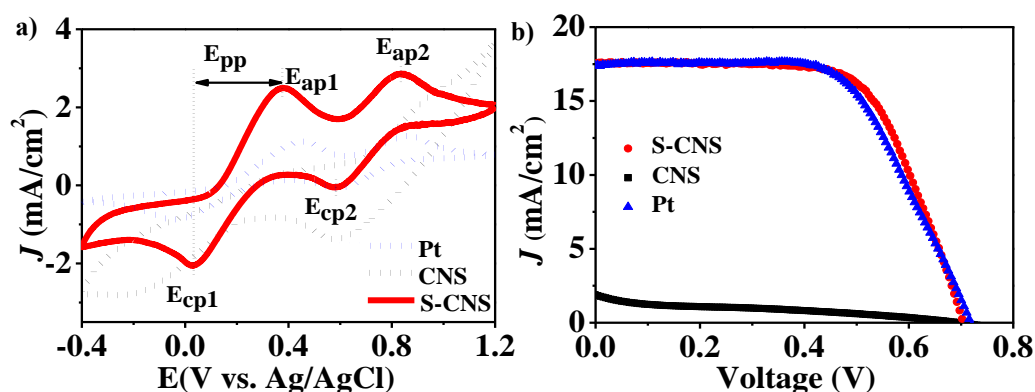


Figure 3.3 (a) CVs of CNS, S-CNS and Pt electrodes in I^-/I_3^- electrolyte. (b) J-V curves of DSSCs with CNS, S-CNS and Pt counter electrodes

The electrocatalytic activity of S-CNS electrode was evaluated for the most commonly employed I^-/I_3^- electrolyte system in dye-sensitised solar cells (DSSCs). The cyclic voltammogram (CV) of CNS electrode in I^-/I_3^- solution shows ill-defined I^-/I_3^- redox responses, indicating a poor reversibility and electrocatalytic activity (Figure 3.3a). In strong contrast, the CV of S-CNS electrode obtained under the same conditions reveals two pairs of well-defined redox peaks, representing the distinctive characteristic of I^-/I_3^- redox processes, confirming the superior electrocatalytic activity of S-CNS (Figure 3.3a). Comparing to Pt (Figure 3.3a) and metal sulphide electrodes (e.g., NiS, MoS, Co_3S_4 and Ni_3S_4),^{15, 16} S-CNS electrode exhibits a noticeable anodically shifted cathodic peak potential and significantly reduced redox peak separation ($E_{\text{pp}}=E_{\text{ap1}}-E_{\text{cp1}}$)

corresponding to I^-/I_3^- redox processes, further confirming the superiority of S-CNS. The excellent electrochemical stability of S-CNS electrode is demonstrated by the almost identical CV responses obtained from 100 consecutive cycles (Figure 3.S3).

The electrocatalytic activity of S-CNS as a counter electrode in DSSCs was also evaluated (Figure 3.3b). The key performance parameters are summarised in Table 3.S1. The DSSC assembled with the S-CNS counter electrode shows a conversion efficiency of 7.79%, almost identical to that of the DSSC assembled with a benchmark Pt counter electrode (7.81%), and much higher than those assembled using S-doped nickel oxide (5.04%)¹⁷ and Co_3S_4 (6.59%)¹⁵ counter electrodes.

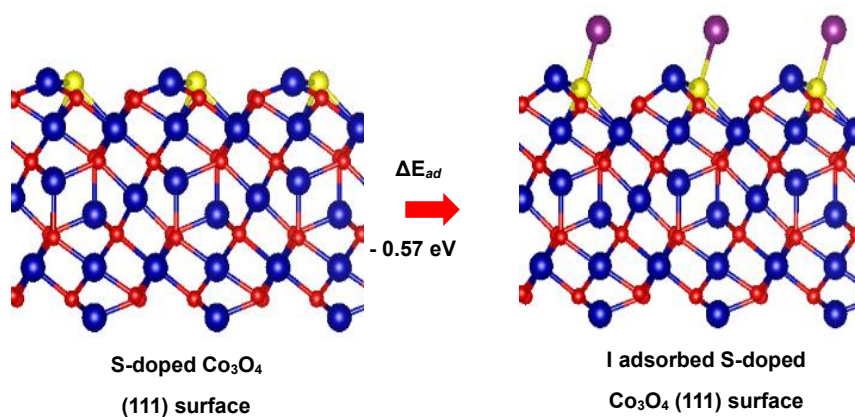


Figure 3.4 Schematic illustration of the atomic arrangements of the clean and I adsorbed S-doped Co_3O_4 (111) surface. Atoms in blue, red, yellow and purple colours represent Co, O, S and I, respectively.

The results shown in Figure 3.3 suggest that only S-doped (rather than the pristine) {111} faceted Co_3O_4 is electrocatalytically active. The possible origin of electrocatalytic activity for S-doped {111} faceted Co_3O_4 towards I_3^- reduction is therefore investigated using Density functional theory (DFT). Previous studies have shown that a high-performance electrocatalyst for I_3^- reduction reaction should possess optimal I adsorption energies (ΔE_{ad}) between -0.33 and -1.20 eV.^{2a} The XPS results (Figure 3.2) suggest that the surface S doping is achieved by

forming Co-S bonds via surface O substitution. The optimised structure of the S-doped Co₃O₄ (111) surface is shown in Figure 3.4. The calculated ΔE_{ad} of I on such optimised surface is -0.57 eV, close to ΔE_{ad} values obtained from Pt (-0.52 eV) and CoS (-0.59 eV) surfaces.^{2a} This indicates that the surface Co-S bonds resulted from VPH doping should be the main form of surface active sites.

3.3 Conclusion

In summary, the effectiveness of VPH approach has been validated for *in-situ* selective doping of exceptionally high S contents onto the surface of Co₃O₄ crystal without destruction to the bulk structures. The obtained electrocatalyst exhibits superior electrocatalytic activity for I₃⁻ reduction, almost identical to that of the benchmark commercial Pt catalyst. The VPH surface doping approach demonstrated here is simple, effective and directly applicable to a wide spectrum of crystalline metal oxides.

3.4 Reference

- 1 (a) B. Winther-Jensen and D. R. MacFarlane, *Energy Environ. Sci.*, 2011, **4**, 2790; (b) M. S. Faber and S. Jin, *Energy Environ. Sci.*, 2014, **7**, 3519; (c) B. Xia, Y. Yan, X. Wang and X. Lou, *Mater. Horiz.*, 2014, **1**, 379.
- 2 (a) Y. Hou, D. Wang, X. H. Yang, W. Q. Fang, B. Zhang, H. F. Wang, G. Z. Lu, P. Hu, H. J. Zhao and H. G. Yang, *Nat. Commun.*, 2013, **4**, 1583; (b) B. Zhang, D. Wang, Y. Hou, S. Yang, X. H. Yang, J. H. Zhong, J. Liu, H. F. Wang, P. Hu, H. J. Zhao and H. G. Yang, *Sci. Rep.*, 2013, **3**, 1836; (c) A. P. O'Mullane, *Nanoscale*, 2014, **6**, 4012.
- 3 (a) K. Gong, F. Du, Z. Xia, M. Durstock and L. Dai, *Science*, 2009, **323**, 760; (b) B. Zhang, N. N. Zhang, J. F. Chen, Y. Hou, S. Yang, J. W. Guo, X. H. Yang, J. H. Zhong, H. F. Wang, P. Hu, H. J. Zhao and H. G. Yang, *Sci. Rep.*, 2013, **3**.
- 4 (a) M. K. Datta, K. Kadakia, O. I. Velikokhatnyi, P. H. Jampani, S. J. Chung, J. A. Poston, A. Manivannan and P. N. Kumta, *J. Mater. Chem. A*, 2013, **1**, 4026;

- (b) S. Y. Yang, Y. S. Choo, S. Kim, S. K. Lim, J. Lee and H. Park, *Appl. Catal., B*, 2012, **111–112**, 317.
- 5 F. Wang, Y. Han, C. S. Lim, Y. Lu, J. Wang, J. Xu, H. Chen, C. Zhang, M. Hong and X. Liu, *Nature*, 2010, **463**, 1061.
- 6 (a) A. Gasparotto, D. Barreca, D. Bekermann, A. Devi, R. A. Fischer, P. Fornasiero, V. Gombac, O. I. Lebedev, C. Maccato, T. Montini, G. Van Tendeloo and E. Tondello, *J. Am. Chem. Soc.*, 2011, **133**, 19362; (b) Z. Mei, Z. Shen, W. Wang and Y. Zhang, *Environ. Sci. Technol.*, 2007, **42**, 590.
- 7 C.-H. Cui and S.-H. Yu, *Acc. Chem. Res.*, 2013, **46**, 1427.
- 8 (a) H. Zhao, Y. Shen, S. Zhang and H. Zhang, *Langmuir*, 2009, **25**, 11032; (b) P. Liu, H. Zhang, H. Liu, Y. Wang, X. Yao, G. Zhu, S. Zhang and H. Zhao, *J. Am. Chem. Soc.*, 2011, **133**, 19032; (c) H. Zhang, Y. Li, P. Liu, Y. Li, D. Yang, H. Yang and H. Zhao, *Chem. -Eur. J.*, 2012, **18**, 5165.
- 9 (a) X. Wang, W. Tian, T. Zhai, C. Zhi, Y. Bando and D. Golberg, *J. Mater. Chem.*, 2012, **22**, 23310; (b) H. Sun, H. M. Ang, M. O. Tade and S. Wang, *J. Mater. Chem. A*, 2013, **1**, 14427.
- 10 H. Yu, Y. Li, X. Li, L. Fan and S. Yang, *Chem. -Eur. J.*, 2014, **20**, 3457.
- 11 S. Y. Bae, H. W. Seo and J. Park, *J. Phys. Chem. B*, 2004, **108**, 5206.
- 12 V. G. Hadjiev, M. N. Iliev and I. V. Vergilov, *J. Phys. C.: Solid State Phys.*, 1988, **21**, L199.
- 13 (a) G. K. Pradhan, N. Sahu and K. M. Parida, *RSC Adv.*, 2013, **3**, 7912; (b) M. H. Z. Maha, M. M. Bagheri-Mohagheghi, H. Azimi-Juybari and M. Shokooh-Saremi, *Phys. Scr.*, 2012, **86**, 055701.
- 14 Q. Wang, L. Jiao, H. Du, Y. Si, Y. Wang and H. Yuan, *J. Mater. Chem.*, 2012, **22**, 21387.
- 15 J. Yang, C. Bao, K. Zhu, T. Yu, F. Li, J. Liu, Z. Li and Z. Zou, *Chem. Commun.*, 2014, **50**, 4824.

- 16 (a) Y. Li, H. Wang, H. Zhang, P. Liu, Y. Wang, W. Fang, H. Yang, Y. Li and H. Zhao, *Chem. Commun.*, 2014, **50**, 5569; (b) M. Al-Mamun, H. Zhang, P. Liu, Y. Wang, J. Cao and H. Zhao, *RSC Adv.*, 2014, **4**, 21277.
- 17 G. H. Guai, M. Y. Leiw, C. M. Ng and C. M. Li, *Adv. Energy Mater.*, 2012, **2**, 334.

3.5 Supporting Information

Experimental section

Chemicals and materials

Cobalt (II) nitrate hexahydrate (98%, Sigma-Aldrich), Aluminium sulphide (99%, Sigma-Aldrich), Lithium perchlorate (98%, Sigma-Aldrich), Anhydrous Lithium iodide (99%, Merck), Iodine (99.99%, Sigma-Aldrich), 4-tert-Butylpyridine (TBP, 96%, Acros) and tert-butanol (TBA, 99.5%, Acros), acetonitrile (99%, Sigma-Aldrich) and ethanol (99.5%, Sigma-Aldrich) were purchased and used without further purification. The mesoporous TiO₂ electrodes, Pt electrodes and EL-HPE (I₃⁻/I⁻) electrolyte were purchased from Dyesol. Deionized water was used throughout the work.

Fabrication of CNS and S-CNS electrodes

The electrodeposition of Co(OH)₂ precursor film was performed at room temperature in a three-electrode electrochemical cell, using an FTO substrate as working electrode, a Ag/AgCl electrode as reference electrode and a Pt mesh as counter electrode in an electrolyte containing 0.01 M Co(NO₃)₂ and 0.02 M NaNO₃ at a constant current of 1.0 mA cm⁻² for 30s with a CHI 760D Electrochemical Workstation (CH Instruments, Inc.). The obtained Co(OH)₂ films were converted to Co₃O₄ counterparts via sintering at 400°C for 30 min in air. The Co₃O₄ nanosheets were readily transformed into S-doped Co₃O₄ nanosheets via an additional H₂S vapour-phase hydrothermal (H₂S-VPH) treatment in a closed Teflon-lined autoclave at 90°C for 6 hours (Figure 2.S1). Al₂S₃ (0.26 g) and 60 μL water were located at the bottom of the autoclave separately to supply the H₂S dopant source. Lab-made Teflon holder was employed to vertically suspend the Co₃O₄ nanosheet film about 10 cm above the Al₂S₃ and water. After H₂S-VPH treatment, the S-doped Co₃O₄ samples were rinsed in carbon sulphide and ethanol respectively and stored in dark.

DSSCs device fabrication

TiO₂ photoanodes were used after calcination at 500°C for 30 min in air before dye loading (N719, Dyesol, Australia) for 24 h. The dye-loaded TiO₂ electrode was coupled with CEs (CNS, S-CNS, or commercial Pt electrodes) to fabricate the DSSCs; these two electrodes were separated by a 60 μm thick Surlyn and sealed by heating. The electrolyte was injected into the solar cell under vacuum, and the hole was sealed with hot-melt glue.

Characterizations

XRD patterns were collected with a Bruker A8 X-ray diffractometer operated at 40 kV and 30 mA. Room-temperature Raman spectra were measured with a Renishaw 100 system Raman spectrometer (632.8 nm He-Ne laser) with a spectral resolution of 2 cm⁻¹ (calibrated using the 520 cm⁻¹ silicon band). The X-ray photoelectron spectroscopy (XPS) data was collected with a Kratos Analytical Axis Ultra X-ray photoelectron spectrometer with a Al X-ray source (1.487 keV). C 1s (284.8 eV) was used as the charge reference. The morphological properties of samples were studied by a JSM-7001 field-emission scanning electron microscope (FE-SEM). The microstructures were analyzed by Tecnai 20 (F20) field-emission transmission electron microscope (FE-TEM) with an accelerating voltage of 200kV. For TEM sample preparation, CNS and S-CNS samples were scrapped from FTO substrates, and dispersed in ethanol under ultrasonic. They were transferred onto TEM copper grids by a drop of the solution and drying in air.

Electrochemical measurements

Cyclic voltammetry (CV) measurements were performed with a CHI 760D (CH Instruments, Inc.) electrochemical workstation. FTO supported CNS, S-CNS or Pt electrode, a platinum mesh net, and a Ag/AgCl electrode were used as the working electrode, counter electrode, and reference electrode, respectively. A solution of 10.0 mM LiI, 1.0 mM I₂, and 0.1 M LiClO₄ in acetonitrile was used as the electrolyte. CV

curves were recorded at a scan rate of 50 mV/s. Tafel polarization curves and electrochemical impedance spectra (EIS) were obtained with symmetrical cells consisting of two identical electrodes; the electrode area was confined to be 0.49 cm². The photocurrent-voltage curves were measured using a potentiostat (Model 362, Princeton Applied Research, US). A 500 W Xe lamp (Trusttech Co., Beijing) with an AM 1.5G filter (Sciencetech, Canada) was used as the light source. The light intensity was measured by a radiant power meter (Newport, 70260) coupled with a broadband probe.

Computational Methods

All calculations were performed using the Vienna *ab initio* simulation program (VASP) based on the first-principles density functional theory (DFT) with the projector augmented wave (PAW) method in this study.¹⁻³ Electron-ion interactions were described using standard PAW potentials,^{4, 5} with valence configurations of $3s^23p^64s^23d^7$ for Co, $5s^25p^5$ for I, $2s^22p^4$ for O, and $3s^22p^4$ for S. And a kinetic energy cut-off of 520 eV was set. Herein, we used Perdew-Burke-Ernzerhof (PBE)⁶ functional for the GGA-level DFT calculations. Due to the insufficient consideration of the on-site Columbic repulsion, between the Co *d* electrons, DFT may fail to describe the electronic structure of Co₃O₄. To overcome this shortcoming, the GGA+U approach was used.⁷ U-J = 6.0 eV for the Co atoms was chosen. A broadening approach proposed by Methfessel and Paxton was employed with an electronic temperature width of 0.2 eV. To simulate the Co₃O₄ (111) surface, a 10-layer slab was enclosed in a supercell with a sufficiently large vacuum region of 15 Å to ensure the periodic images to be well separated. During the geometry optimizations, the atoms in the bottom three layers were fixed at the bulk-like positions; and the rest atoms were allowed to relax until the Hellmann-Feynman forces were smaller than 0.01 eV/Å. Our calculations with the consideration of spin-polarizations demonstrated that the most stable magnetic structures of Co₃O₄ are anti-ferromagnetic. And two neighbouring 4-coordinated Co cations are with opposite spins. To this end, in the middle of our Co₃O₄ (111) surface slab, the two 4-coordinated Co cations are also with the opposite spins in our systems.

For Brillouin-zone integrations, gamma-centered k -point grids of special points with a $(4 \times 4 \times 1)$ mesh were used for the (1×1) surface cell. The calculation of I adsorption on S-doped Co_3O_4 (111) surface is based on the details described elsewhere.⁸

Figures and captions

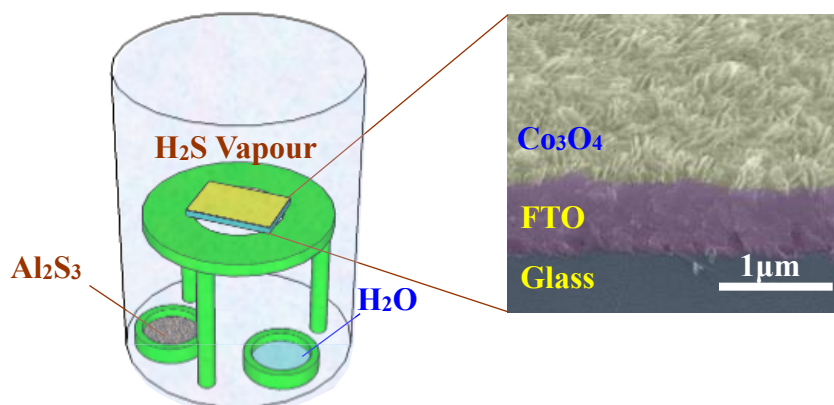


Figure 3.S1 Schematic illustration of the H_2S -VPD doping setup

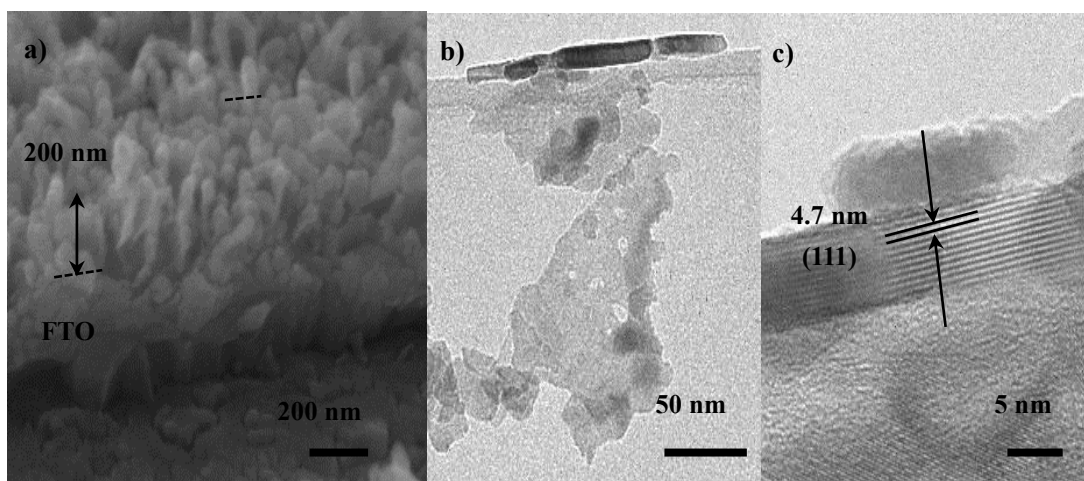


Figure 3.S2(a) SEM image, (b) TEM image, and (c) HRTEM image of CNS sample.

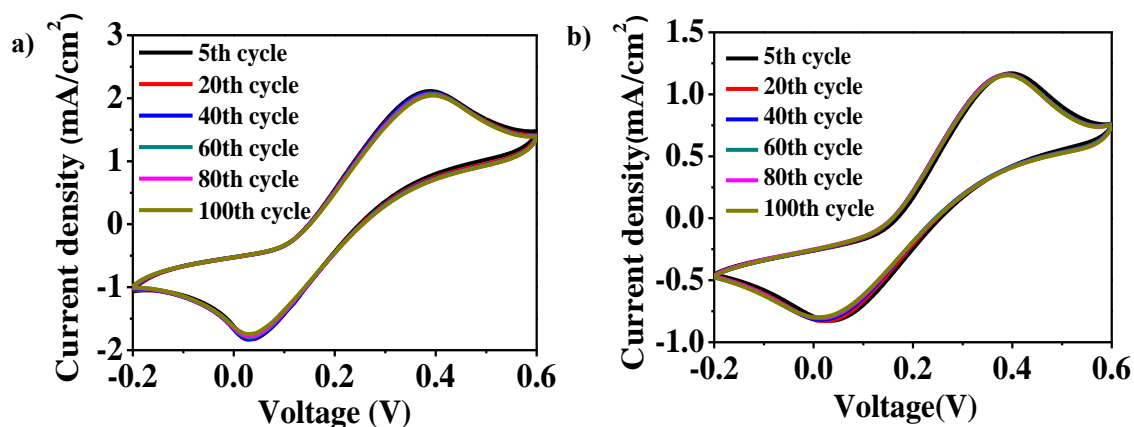


Figure 3.S3 Consecutive CV curves of a) S-CNS sample and b) Pt in I^-/I_3^- electrolyte.

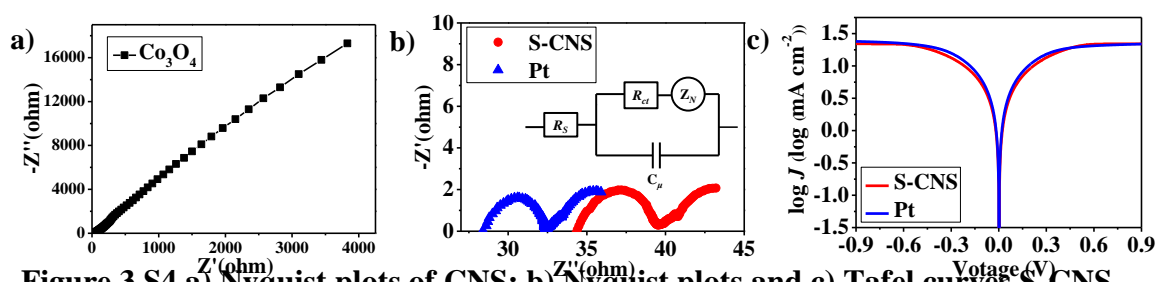


Figure 3.S4 a) Nyquist plots of CNS; b) Nyquist plots and c) Tafel curves S-CNS and Pt electrodes. Inset of b) shows the equivalent circuit.

Electrochemical impedance spectroscopy (EIS) of the symmetrical cells composed of CNS, S-CNS and Pt electrodes was performed to investigate the charge-transfer behaviours and diffusion resistances. The value of EIS parameters (Table S1) were gained by fitting the EIS data with an equivalent circuit (inset of Fig. S2a). R_s is the series resistance of the electrolyte and electrodes. R_{ct} is the charge-transfer resistance at the electrode-electrolyte interface, which is an indicator for the electrocatalytic activity of the electrode towards the reduction of I_3^- . The similar R_{ct} values of S-CNS and Pt electrodes imply they both possess good electrocatalytic activity.

Table 3.S1 Photovoltaic parameters and EIS parameters of the DSSCs with different electrodes as counter electrode.

Electrode	J_{sc} (mA cm ⁻²)	V_{oc} (V)	FF	η (%)	R_s (Ω)	R_{ct} (Ω)
CO	1.89	0.69	0.25	0.33	-	-
SCO	16.83	0.70	0.66	7.79	34.83	4.15
Pt	17.52	0.71	0.66	7.81	28.92	3.13

To further examine the electrocatalytic activities, Tafel polarization curve of logarithmic current density as function of potential was collected (Fig. S2b). The exchange current density (J_0), obtained from the extrapolated intercepts of anodic and cathodic branches, is indicative of the electrocatalytic activity. As shown in Fig. S2b, Tafel plot of S-CNS sample exhibits similar slope compared with Pt electrode indicating its good electrocatalytic activity.

Reference

1. G. Kresse and J. Hafner, *Phys. Rev. B*, 1993, **47**, 558-561.
2. G. Kresse and J. Furthmuller, *Comput. Mater. Sci.*, 1996, **6**, 15-50.
3. G. Kresse and D. Joubert, *Phys. Rev. B*, 1999, **59**, 1758-1775.
4. D. Vanderbilt, *Phys. Rev. B*, 1990, **41**, 7892-7895.
5. G. Kresse and J. Hafner, *J. Phys.-Condens. Mat.*, 1994, **6**, 8245-8257.
6. J. P. Perdew, W. Burke and M. Ernzerhof, *Phys. Rev. Lett.*, 1996, **77**, 3865.
7. S. L. Dudarev, G. A. Botton, S. Y. Savrasov, C. J. Humphreys and A. P. Sutton, *Phys. Rev. B*, 1998, **57**, 1505-1509.
8. Y. Hou, D. Wang, X. H. Yang, W. Q. Fang, B. Zhang, H. F. Wang, G. Z. Lu, P. Hu, H. J. Zhao and H. G. Yang, *Nat. Commun.*, 2013, **4**, 1583

Chapter 4. Synthesis, characterization of S-doped metal oxides and their photovoltaic activities

4.1 Introduction

In recent years, there has been a widespread interests in the studies on high performance energy-conversion devices aiming to alleviate the unprecedented energy demand as well as the pollution problems related to current energy consumption. Among these useful energy-conversion devices, dye-sensitized solar cells (DSSCs) have become the focus of attention as an important photovoltaic device due to its cost-effectiveness, facile fabrication procedure and high energy conversion efficiency.¹⁻³ The counter electrode (CE) as one of the most important components in the DSSCs performs two critical functions, which collects the electron from the external circuit, and catalyzes the reduction of triiodide ions, thereby realizing the regeneration of the sensitizer.⁴⁻⁵ Although platinum (Pt) exhibits a very good performance as a superior CE material, the rarity and high cost of Pt severely impedes the large-scale application of DSSCs.⁶⁻⁷ Therefore, significant amount of efforts have been devoted to exploiting low cost, highly active and stable electrocatalyst substitutes to the Pt materials.

Recently, several groups of compounds such as early-transition-metal carbides (TMCs)⁸⁻¹⁰, nitrides (TMNs)¹¹⁻¹³ oxides (TMOs)¹⁴⁻¹⁶ and chalcogenides (TMChs)^{2, 17-18} were reported showing Pt-like catalytic activities, some of these materials even exhibited higher energy conversion efficiency than their Pt counterparts. However, the fabrication of these materials either requires extremely high temperatures or showing much lower electrocatalytic activities compared with Pt.

We have reported a vapor-phase hydrothermal (VPH) method with a low temperature as an efficient approach to achieve S doping of cobalt oxides (Co_3O_4) which dramatically increased electrocatalytic activities by creating an active-site-rich surface on the resultant electrocatalysts.¹⁹ Herein, we explore VPH approach as a generic method for an effective creation of electrocatalytically active sites (sulphur

dopants) on other metal oxides materials, e.g., NiO and Fe₂O₃, as the CE materials for DSSCs. The results displayed that enormous improvements have been successfully accomplished in their electrocatalytic activities after VPH treatment compared with their corresponding raw counterparts, and also energy conversion efficiencies of DSSCs with these resultant electrocatalysts as CE material have been dramatically improved.

4.2 Experimental Section

Chemicals

Nickle nitrate hexahydrate (99.9%), Iron (III) sulfate hydrate, NaNO₃, NaOH, Al₂S₃, and LiClO₄ (98%) were obtained from Sigma-Aldrich. Anhydrous LiI, I₂, and acetonitrile (ACN) were purchased from Merck. 4-tert-Butylpyridine (TBP, 96%) and tert-butanol (TBA, 99.5%) were received from Acros. Ethanol (ACS reagent, 99.5%) was purchased from Aldrich Chemical Co. The commercial TiO₂ electrodes, Pt electrodes and electrolyte were purchased from Sol. All chemicals mentioned above were used without further purification. Deionized water (DIW) was used throughout the work.

Fabrication of various counter electrodes

The electrodeposition of Ni(OH)₂ and Fe(OH)₃ precursor films were formed directly on FTO substrates using a three-electrode electrochemical cell with a Ag/AgCl electrode as reference electrode and a Pt mesh as counter electrode. Specifically, a Ni(OH)₂ film was obtained in an electrolyte containing 0.05 M Ni(NO₃)₂ and 0.1 M NaNO₃, while a Fe(OH)₃ film was carried in 0.05 M and 0.1M NaOH solution at a constant current of 1.0 mA cm⁻² for 100s with a CHI 760D Electrochemical Workstation (CH Instruments, Inc.). The obtained Ni(OH)₂ and Fe(OH)₃ films were converted to NiO and Fe₂O₃ counterparts via sintering at 350°C and 450°C, respectively, for 30 min in air.

Thereafter, the films of S-doped NiO and Fe₂O₃ were obtained by vapour-phase hydrothermal (VPH) method. Specifically, NiO or Fe₂O₃ film on the FTO substrates were held on a home-made PTFE holder in a hydrothermal reactor where Al₂S₃ (0.26g) and 60 μ L water were placed at the bottom without direct contact. The VPH reaction between the metal oxide film and hydrogen disulphide gas is initialized upon the hydrolysis of Al₂S₃ at the presence of water vapor generated at high temperature. The VPH reactors were heated for 6 hours in an oven with preset temperatures of 120°C and 150°C for NiO and Fe₂O₃ respectively.

Fabrication of the DSSCs

TiO₂ electrodes with mesoporous TiO₂ films coated on FTO substrates were purchased commercially from Dyesol. They are sintered at 450°C for 30 mins in air prior to use. The sintered TiO₂ electrode was coupled with one of the various CEs (CEs with metal oxides, S-doped metal oxides, and commercial Pt) to fabricate the DSSC; these two electrodes were separated by a 60 μ m thick Surllyn and sealed by heating. The iodide/triiodide electrolyte was injected into the gap between the two electrodes under vacuum, and the hole was sealed with hot-melt glue after the electrolyte injection.

Characterization

The morphological properties of samples were investigated by a JSM-7001 scanning electron microscope (SEM). Cyclic voltammetric (CV) measurements were performed with a CHI 7600 electrochemical workstation (CH Instruments, Inc., USA), using the conventional three-electrode system. One of the various CEs, a platinum sheet, and a Ag/AgCl electrode were used as the working electrode, counter electrode, and reference electrode, respectively. The solution of 10.0 mM LiI, 1.0 mM I₂, and 0.1 M LiClO₄ in acetonitrile was used as the electrolyte for all CV measurements. CV curves were recorded at a scan rate of 100 mV/s. Tafel polarization curves were obtained by symmetrical cells, at a scan rate of 50 mV/s, using a CHI 760 instrument with a two-electrode system. The symmetrical cell contained two identical electrodes; the film area was confined to be 0.25 cm² by removing the side portions by scrapping. The

photocurrent density-voltage characteristic was measured using a computer-controlled scanning potentiostat (Model 362, Princeton Applied Research, US). A 500 W Xe lamp (Trusttech Co., Beijing) with an AM 1.5G filter (Sciencetech, Canada) was used as the light source. The light intensity was measured by a radiant power meter (Newport, 70260) coupled with a broadband probe (Newport, 70268).

4.3 Results and Discussion

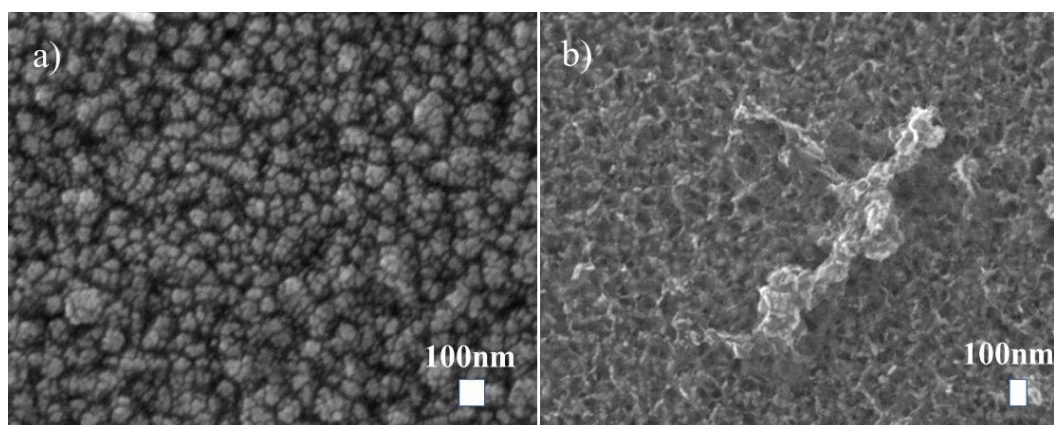


Figure 4.1 SEM images of a) S-NiO and b) S-Fe₂O₃ film on FTO substrates.

The morphology of resultant S-NiO and S-Fe₂O₃ after VPH treatment was analyzed using scanning electron microscopy (SEM). As we can see from Figure 4.1 that a S-NiO film is composed of nanoparticles with the mean diameter in the range from 10 nm to 50 nm, while a S-Fe₂O₃ film is composed of particles with salient edges formed. As shown in Figure 4.2, cyclic voltammetry (CV) measurements were carried out in a three-electrode system, with Ag/AgCl as the reference electrode, Pt foil as the counter electrode and NiO, S-NiO, Fe₂O₃ and S-Fe₂O₃ as working electrodes, respectively, with a scan rate of 50 mV s⁻¹, to investigate the electrocatalytic activity of these working electrodes toward triiodide reduction in the I⁻/I₃⁻ electrolyte solution. The electrolyte used for this study was 10 mM LiI, 1 mM I₂ and 0.1 M LiClO₄ in acetonitrile. These electrodes exhibit obviously different electrochemical activity towards I⁻/I₃⁻ redox reaction before and after VPH treatment. No significant current and oxidation–

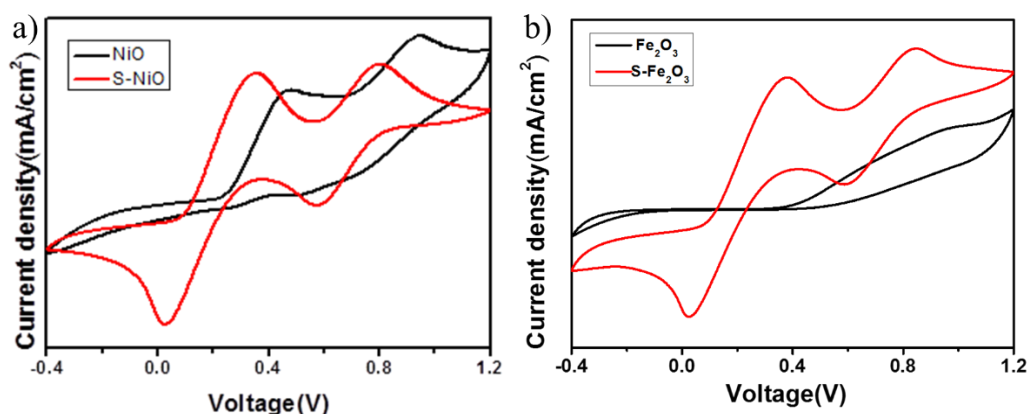


Figure 4.2 Cyclic voltammograms comparison of a) NiO/FTO and S-NiO/FTO samples; b) Fe₂O₃/FTO and S-Fe₂O₃/FTO samples. The scan rate and scan voltage range are 50 mV s⁻¹ and -0.4–1.2 V vs Ag/AgCl, respectively.

reduction were observed for both NiO and Fe₂O₃ CEs at the potential range from -0.4 to 1.2 V, which indicated their poor electrocatalytic activity towards I⁻/I₃⁻ redox reaction. Distinctively, the CV curves of the S-NiO and S-Fe₂O₃ electrodes after a facile VPH treatment exhibited two typical pairs of redox peaks assigned to the redox reactions of I₃⁻ + 2e⁻ → 3I⁻, 3I₂ + 2e⁻ → 2I₃⁻, respectively,^{18,20} which strongly indicating that S-NiO and S-Fe₂O₃ showed significantly improved electrochemical activity towards I⁻/I₃⁻ redox reaction.

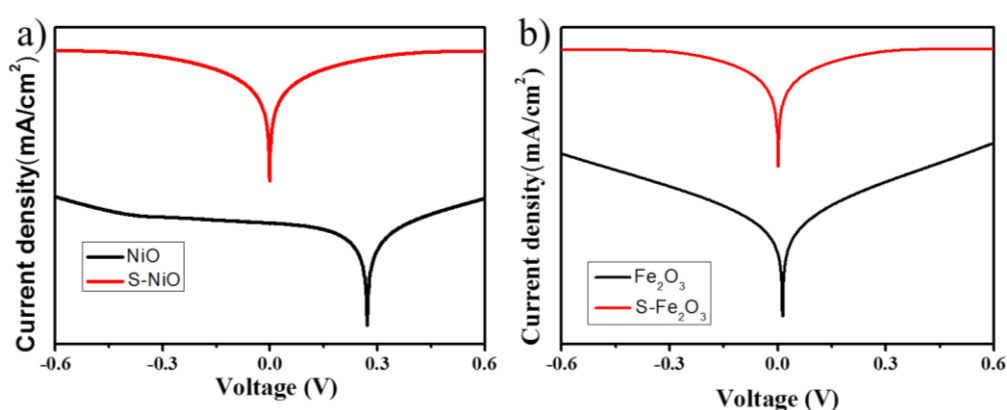


Figure 4.3 Tafel polarization curves for a) NiO/FTO and S-NiO/FTO and b) Fe₂O₃/FTO and S-Fe₂O₃/FTO counter electrodes.

Tafel polarization measurement was also carried out in a symmetric cell assembly

with usual DSSCs electrolyte mentioned above to further confirm electrocatalytic activity for NiO, S-NiO, Fe₂O₃ and S-Fe₂O₃ electrodes, respectively. The scan rate for this measurement was 10 mV s⁻¹. The catalytic properties of an electrode are determined by the Tafel zone, which is at the middle of the curve with a steep slope. The exchange current density (J_0), which is the intersection of the cathodic branch with the equilibrium potential line of the corresponding Tafel curves, is directly related to the electrocatalytic activity of an electrode.²¹ The steeper the Tafel zone, the higher J_0 and the more catalytically active the materials. As shown in Figure 4.3, NiO electrode showed an irregular Tafel curve, which indicated its poor electrocatalytic activities, while S-NiO electrode displayed a steep Tafel slope, which is in a good agreement with the results of CV measurements. Similarly, S-Fe₂O₃ electrode has a steeper change in the slope of the curve and also higher diffusion current density than its Fe₂O₃ counterpart.

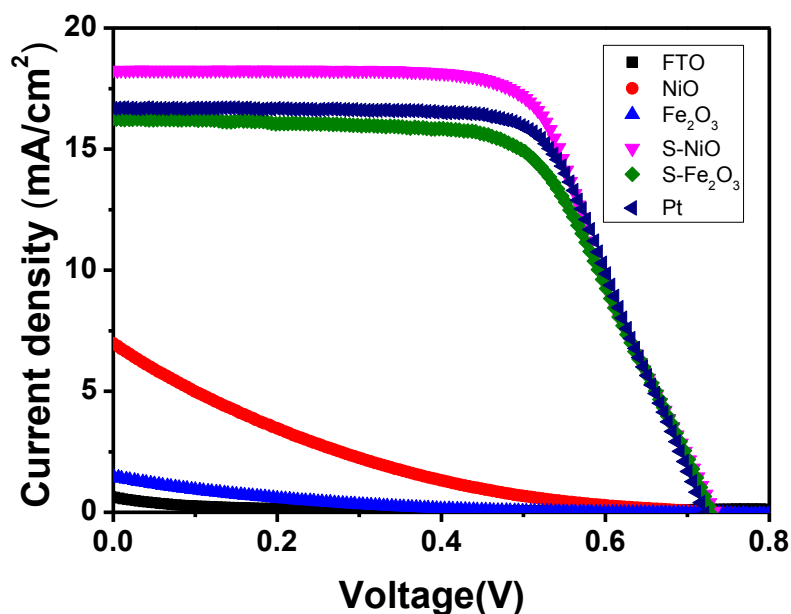


Figure 4.4 Photocurrent density–voltage characteristics of FTO, NiO/FTO, S-NiO/FTO, Fe₂O₃/FTO, S-Fe₂O₃/FTO and Pt/FTO CEs.

Figure 4.4 illustrates the J – V curves of the DSSCs based on FTO, NiO/FTO, S-NiO/FTO, Fe₂O₃/FTO, S-Fe₂O₃/FTO and Pt/FTO CEs, respectively, and also open-circuit voltages (V_{oc}), short-circuit photocurrent densities (J_{sc}), fill factors (FF), and

Table 4.1 Photovoltaic performance comparisons of DSSCs using S-NiO/FTO, S-Fe₂O₃/FTO, and Pt/FTO CEs.

<i>Sample</i>	<i>J_{sc} (mA/cm²)</i>	<i>V_{oc} (V)</i>	<i>FF</i>	<i>η (%)</i>
<i>S-NiO</i>	16.68	0.72	0.67	8.05
<i>S-Fe₂O₃</i>	16.26	0.73	0.63	7.48
<i>Pt</i>	18.23	0.73	0.65	8.61

power conversion efficiencies (η) of S-NiO/FTO, S-Fe₂O₃/FTO and Pt/FTO CEs are listed in Table 4.1. DSSCs based on FTO, NiO/FTO, and Fe₂O₃/FTO show poor photovoltaic performances with low *FF* and poor energy conversion efficiency, which is consistent with the absent redox peaks in CV curves of NiO and Fe₂O₃ in I⁻/I₃⁻ electrolyte. However, after VPH treatment, the S-NiO/FTO CE exhibits a high efficiency of 8.05%, and the corresponding *J_{sc}*, *V_{oc}* and *FF* are 16.68 mA/cm², 0.72 V and 0.67, whereas cell efficiency of S-Fe₂O₃/FTO CE reaches up to 7.48% *J_{sc}* = 16.26 mA/cm², *V_{oc}* = 0.73 V, *FF* = 0.63. The higher *J_{sc}* and η for cells with S-NiO/FTO and S-Fe₂O₃/FTO CEs are clearly due to the higher electrocatalytic activity for the I₃⁻ reduction of their CEs, which mainly results from the increased active catalytic sites after S doping. Compared to the Pt/FTO cell (*FF*=0.65), the S-NiO/FTO CE even possesses a slightly higher *FF*. Even though η of the S-NiO/FTO and S-Fe₂O₃/FTO cells are slightly lower than that of Pt/FTO cell (8.61%), this can be mainly ascribed to a slightly lower *J_{sc}*. The excellent photovoltaic performances of S-NiO/FTO and S-Fe₂O₃/FTO cells could be promising alternatives for Pt-free DSSCs.

4.4 Conclusion

In conclusion, a facile VPH technique has been successfully extended to the fabrication of sulphur doped metal oxide films (metal = nickel or iron) via in-situ doping approach. Our preliminary results confirm that compared with their metal oxide counterparts, the sulphur doped metal oxide films demonstrate significantly enhanced electrocatalytic activities towards the reduction of triiodide. The photovoltaic performances of the DSSCs have reached 8.05% and 7.48% for S-NiO and S-Fe₂O₃

respectively which are similar to those with benchmark Pt electrode. In view of their earth abundancy, wide availability and superior electrocatalytic performance, both S-NiO and S-Fe₂O₃ can be viewed as promising CE alternatives to be used in high efficiency, Pt-free DSSCs.

4.5 Reference

1. Casaluci, S.; Gemmi, M.; Pellegrini, V.; Di Carlo, A.; Bonaccorso, F., Graphene-based large area dye-sensitized solar cell modules. *Nanoscale* **2016**, *8* (9), 5368-5378.
2. Huo, J.; Wu, J.; Zheng, M.; Tu, Y.; Lan, Z., Flower-like nickel cobalt sulfide microspheres modified with nickel sulfide as Pt-free counter electrode for dye-sensitized solar cells. *Journal of Power Sources* **2016**, *304*, 266-272.
3. Hagfeldt, A.; Boschloo, G.; Sun, L.; Kloo, L.; Pettersson, H., Dye-sensitized solar cells. *Chemical reviews* **2010**, *110* (11), 6595-6663.
4. Law, M.; Greene, L. E.; Johnson, J. C.; Saykally, R.; Yang, P., Nanowire dye-sensitized solar cells. *Nature materials* **2005**, *4* (6), 455-459.
5. Mor, G. K.; Shankar, K.; Paulose, M.; Varghese, O. K.; Grimes, C. A., Use of highly-ordered TiO₂ nanotube arrays in dye-sensitized solar cells. *Nano letters* **2006**, *6* (2), 215-218.
6. O'regan, B.; Grifitzi, M., A low-cost, high-efficiency solar cell based on dye-sensitized. *nature* **1991**, *353* (6346), 737-740.
7. Wang, X.; Zhi, L.; Müllen, K., Transparent, conductive graphene electrodes for dye-sensitized solar cells. *Nano letters* **2008**, *8* (1), 323-327.
8. Jang, J. S.; Ham, D. J.; Ramasamy, E.; Lee, J.; Lee, J. S., Platinum-free tungsten carbides as an efficient counter electrode for dye sensitized solar cells. *Chemical Communications* **2010**, *46* (45), 8600-8602.
9. Wu, M.; Lin, X.; Hagfeldt, A.; Ma, T., Low-Cost Molybdenum Carbide and Tungsten Carbide Counter Electrodes for Dye-Sensitized Solar Cells. *Angewandte Chemie International Edition* **2011**, *50* (15), 3520-3524.
10. Wu, M.; Lin, X.; Wang, Y.; Wang, L.; Guo, W.; Qi, D.; Peng, X.; Hagfeldt, A.;

Grätzel, M.; Ma, T., Economical Pt-free catalysts for counter electrodes of dye-sensitized solar cells. *Journal of the American Chemical Society* **2012**, *134* (7), 3419-3428.

11. Lin, X.; Wu, M.; Wang, Y.; Hagfeldt, A.; Ma, T., Novel counter electrode catalysts of niobium oxides supersede Pt for dye-sensitized solar cells. *Chem Commun (Camb)* **2011**, *47* (41), 11489-11491.

12. Jiang, Q.; Li, G.; Gao, X., Highly ordered TiN nanotube arrays as counter electrodes for dye-sensitized solar cells. *Chemical communications* **2009**, (44), 6720-6722.

13. Li, G.; Song, J.; Pan, G.; Gao, X., Highly Pt-like electrocatalytic activity of transition metal nitrides for dye-sensitized solar cells. *Energy & Environmental Science* **2011**, *4* (5), 1680-1683.

14. Wu, M.; Lin, X.; Hagfeldt, A.; Ma, T., A novel catalyst of WO₂ nanorod for the counter electrode of dye-sensitized solar cells. *Chemical Communications* **2011**, *47* (15), 4535-4537.

15. Lin, X.; Wu, M.; Wang, Y.; Hagfeldt, A.; Ma, T., Novel counter electrode catalysts of niobium oxides supersede Pt for dye-sensitized solar cells. *Chemical Communications* **2011**, *47* (41), 11489-11491.

16. Yun, S.; Wang, L.; Guo, W.; Ma, T., Non-Pt counter electrode catalysts using tantalum oxide for low-cost dye-sensitized solar cells. *Electrochemistry Communications* **2012**, *24*, 69-73.

17. Chuang, H.-M.; Li, C.-T.; Yeh, M.-H.; Lee, C.-P.; Vittal, R.; Ho, K.-C., A coral-like film of Ni@NiS with core-shell particles for the counter electrode of an efficient dye-sensitized solar cell. *Journal of Materials Chemistry A* **2014**, *2* (16), 5816-5824.

18. Zhao, W.; Zhu, X.; Bi, H.; Cui, H.; Sun, S.; Huang, F., Novel two-step synthesis of NiS nanoplatelet arrays as efficient counter electrodes for dye-sensitized solar cells. *Journal of Power Sources* **2013**, *242*, 28-32.

19. Tan, Z.; Liu, P.; Zhang, H.; Wang, Y.; Al-Mamun, M.; Yang, H. G.; Wang, D.; Tang, Z.; Zhao, H., An in situ vapour phase hydrothermal surface doping approach for

fabrication of high performance Co_3O_4 electrocatalysts with an exceptionally high S-doped active surface. *Chemical Communications* **2015**, 51 (26), 5695-5697.

20. Wu, M.; Wang, Y.; Lin, X.; Yu, N.; Wang, L.; Wang, L.; Hagfeldt, A.; Ma, T., Economical and effective sulfide catalysts for dye-sensitized solar cells as counter electrodes. *Physical Chemistry Chemical Physics* **2011**, 13 (43), 19298-19301.

21. Lin, J.-Y.; Chou, S.-W., Highly transparent NiCo_2S_4 thin film as an effective catalyst toward triiodide reduction in dye-sensitized solar cells. *Electrochemistry Communications* **2013**, 37, 11-14.

Chapter 5 General Conclusion and Future Work

The major objective of this thesis is to develop generic synthesis method to convert earth abundant nanostructured metal oxide into highly efficient electrocatalytic active materials for energy conversion, i.e., as counter electrode materials in dye-sensitized solar cells. Noble metals and their alloys have been the benchmark materials to catalyse numerous key chemical reactions in energy conversion devices, such as dye-sensitized solar cells (DSSCs), fuel cells, water electrolyzers. To develop generic, viable synthesis method to fabricate efficient, stable alternatives using other widely available materials will provide avenues towards large scale applications of such important devices. In this thesis, a facile and robust vapor-phase hydrothermal (VPH) treatment has been developed to introduce high sulphur dopants as active sites into the metal oxide materials to remarkably improve their electrocatalytic activities that could be used as counter electrode (CE) in high performance DSSCs. The research results and essential details of each experimental chapter are briefly summarized as below:

In Chapter 2, for the first time, Co_3O_4 nanowires films have been successfully converted into S- Co_3O_4 counterpart by the simple VPH approach. The structural and electrocatalytic properties of the resultant S- Co_3O_4 films are systematically characterized and show strong dependence on the fabrication parameters. DSSCs equipped with the optimized S- Co_3O_4 films CE demonstrated high photovoltaic performance that is comparable to the commercial platinum (Pt) electrode. The superior electrocatalytic activities of S- Co_3O_4 films confirm their potentials to be used as alternative CE materials for Pt-free DSSCs.

In Chapter 3, unprecedentedly high sulphur contents (47%) have been introduced to the surface of electrodeposited Co_3O_4 thin film via VPH approach and they have demonstrated the high electrocatalytic activities towards triiodide reduction reaction. Characterization data confirms that surface oxygen have been fully substituted with the sulphur during the mild VPH treatment. Density Function Theory calculation confirms that the Co-S species on the surface plays key role in the electrocatalytic reduction of

triiodide in electrolytes. The solar-to-electricity conversion efficiency of the DSSCs with the as prepared S-Co₃O₄ CE has achieved 7.79% almost identical to that with benchmark Pt electrode (7.81%).

In Chapter 4, the VPH method has been successfully extended to other metal oxides such as NiO and Fe₂O₃ to fabricate S-NiO and S-Fe₂O₃ electrodes. The applicability of the robust VPH techniques has been verified with the significantly enhanced electrocatalytic activities of the resultant electrodes compared to the pristine NiO and Fe₂O₃ counterparts. Relatively high solar-to-electricity conversion efficiency has been achieved using these low cost, earth abundant S-NiO and S-Fe₂O₃ materials when compared to commercial Pt electrode, confirming the usefulness of the generic VPH for the development of other novel functional materials.

Despite of the positive results demonstrated in this study, future work is highly recommended in the following aspects: firstly, from material engineering point of view, the full capability of the generic VPH approach is required to be further exploited. Other metal compounds (oxides, nitrides, carbides, chalcogenides), metal free materials (carbon, graphene, carbon nitride etc.) and their composite have been proven to possess potentials to be activated to boost their photocatalytic, electrocatalytic properties using VPH. It is strongly believed that the synergy between the atomic structures with the alien atoms would dramatically alter the physiochemical properties that open up a new avenue towards high performance functional materials for various applications. Secondly, in-depth understanding on the VPH reaction energetics, reaction kinetics, interfacial reaction and mass transfer is highly desirable. Investigation on the fundamental processes of the entire VPH reaction will not only allow knowledge on the principle of the reaction mechanism but more importantly provide opportunities to manipulate the process to achieve specific goal. To achieve this, systematic experiment and also in-situ monitoring techniques need to be put in place. Also, computational calculation tools should be involved to provide theoretical prediction and guidance.